A NUMERICAL STUDY OF HEAT TRANSFER IN BUBBLY FLOWS

A Dissertation

Submitted to the Faculty

of

Purdue University

by

Pramod R. Bhuvankar

In Partial Fulfillment of the

Requirements for the Degree

of

Doctor of Philosophy

August 2019

Purdue University

West Lafayette, Indiana

THE PURDUE UNIVERSITY GRADUATE SCHOOL
STATEMENT OF DISSERTATION APPROVAL

Dr. Sadegh Dabiri, Chair

School of Agricultural and Biological Engineering &

School of Mechanical Engineering.

Dr. Issam Mudawar

School of Mechanical Engineering.

Dr. Arezoo Ardekani

School of Mechanical Engineering.

Dr. Alina Alexeenko

School of Aeronautics and Astronautics.

Approved by:

Dr. Jay Gore

School of Mechanical Engineering.

ACKNOWLEDGMENTS

I want to acknowledge the central role played by my advisor Dr. Sadegh Dabiri in my work. I would like to thank him for the guidance, resources, creative freedom, and funding support that he provided me. I also wish to thank him for being patient with my progress.

I want to thank Dr. Ardekani, Dr. Alexeenko, and Dr. Mudawar for taking the time to be at my defense. I wish to thank Dr. Mudawar for offering the course "Two-phase flow and heat transfer", which has undoubtedly helped me in my research.

I want to thank my girlfriend Madelina Nuñez for being a pillar of support during my thesis. I also want to thank my friends at Vienna café, especially Taylor Wolf, Mehran Einakchi, Chris Heggarty, Jeremy Brown, Justin Bougher, Ali Williamson, Vish, and Vishnu. I have also enjoyed tremendous support from my dear friends Valeria, David, James, Raghu, Maria and Meike Ernst.

I am immensely thankful to my co-workers, especially Sangkyu "Calvin" Kim, Ilyas Yilgor, Tiago, Alfonso, Yash Shah and Maathangi Ganesh for their insights during our many group meetings. I would like to thank Sangkyu "Calvin" Kim for the many enjoyable discussions I have had with him, and all the times we spent making music. He has inspired me to be a better computational fluid dynamicist.

I owe everything I achieve in life to my parents, Chandu and Anuradha Bhuvankar. Words cannot do justice to how deeply I am indebted to them.

TABLE OF CONTENTS

Page

LIST OF TABLES

LIST OF FIGURES

Figure Page

Figure Page

Figure Page

SYMBOLS

VARIABLES

T	Temperature
g	Gravitational acceleration
$\dot{\gamma}$	Shear rate
x, y, z	Coordinates
U	u velocity of the left wall
t	Time
tm	Non-dimensional temperature
L_v	Latent heat of vaporisation
d	Bubble diameter
δ_T	Thermal layer thickness
q"	Heat flux
ρ	Density
u	Velocity vector
σ	Surface tension
μ	Dynamic viscosity
ν	Kinamatic viscosity
k	Thermal conductivity
C_p	Specific heat capacity at constant pressure
C	Specific heat capacity
h	Heat transfer coefficient
A_b	Projection area of the bubble
$\overline{V}$	Area integral of the v velocity

h_r	Reversal height
w	Reversal width
H	Augmented reversal height
ω	Vorticity
ψ	Stream function
Re	Reynolds number
Pr	Prandtl number
Ar	Archimedes number
Nu	Nusselt number
La	Laplace number
Ja	Jakob number $= \frac{\rho_f C_f \Delta T_{sup}}{\rho_g L_v}$
$\overline{Nu}$	Fractional improvement in Nu
$\overline{\dot{\gamma}}$	Dimensionless shear rate
$\Delta()$	Improvement in
$\overline{()}, ()^*$	Dimensionless

SUBSCRIPTS

L, R	Left, Right
0	Initial
l, g	Liquid, gas
b	Bubble
s	Single phase
D	Downstream
$D1$	Whole downstream
$D2$	Thin strip downstream
$wall$	At the right wall.
f	Liquid
sup	Superheat

ABSTRACT

Bhuvankar, Pramod R. PhD, Purdue University, August 2019. A Numerical Study of Heat Transfer in Bubbly Flows. Major Professor: Sadegh Dabiri, School of Mechanical Engineering.

Two-phase flow and heat transfer has a wide variety of applications ranging from nuclear power plants to computer chip cooling. The efficient designs of these systems require a clear understanding of the mechanisms by which two-phase flows enhance heat transfer. With the rapid growth in computing power, Computational Fluid Dynamics is becoming an increasingly reliable predictive tool to understand the physics underlying two-phase flow and heat transfer. We identify the two chief phenomena affecting heat transfer in two-phase flows as being the improved convective effect in bubbly flows, and the phase change phenomenon. We examine three key aspects of bubbly flows in the present work namely: a) The flow of bubbles near vertical walls, b) the heat transfer associated with a non-condensable bubble rising near a vertical wall, and c) the heat transfer associated with boiling and condensation involving bubbles.

The first part involves studying the rise velocity of a layer of bubbles rising near a vertical wall. We derive a scaling between the rise velocity based Reynold's number and the Archimedes number. The second part involves examining the flow pattern around a single bubble rising under the buoyancy effect in a shear flow near a heated wall, and how it affects the heat transfer from the wall. We study the dependence of the fractional improvement in Nusselt number at the wall on various non-dimensional parameters such as the Archimedes number, the Laplace number and the shear rate. Our study shows the existence of an optimum dimensionless shear rate for heat transfer enhancement and a strong dependence between the flow pattern around the bubble and its associated heat transfer enhancement. The third part involves building a nu-

merical model to study flow boiling in micro-channels. We validate the proposed model with two benchmark problems and two experimental studies. The validated numerical tool is then used to understand the effect of varying the micro-channel inlet flow rate on its heat transfer characteristics. This numerical tool is further developed to include a stagnant micro-layer model that can simulate nucleate boiling. We then use it to study the flow boiling characteristics of a line of bubbles undergoing boiling and lift-off in a shear flow. In the end, based on existing literature in the field, we propose future tasks to be undertaken in the area of numerical two-phase flow.

1. INTRODUCTION

Two-phase flow is an effective means for heat transfer enhancement. It has been studied over several decades due to its application in a wide variety of areas such as the chemical industry, food industry, power plants, refrigeration, and in recent years, heat removal from high heat flux devices such as computer chips and fuel cells. Bubbly flows in particular, are found in many of the above mentioned applications. A clear understanding of the impact of bubbles on surrounding flows in terms of momentum and energy transport is required for the thermal design of the mentioned systems. Bubbly flows that undergo boiling or condensation have the added complexity of the coupling between energy and momentum transport brought about by phase change.

Flow boiling in micro-channels has been an active field of research over the past couple of decades with the objective being heat removal from electronic devices. Two-phase flow accompanied by phase change in the form of boiling offers the advantage of suppressing the temperature fluctuations under high heat fluxes owing to the latent heat of vaporization of the liquid. Chamund *et al.* [1] indicate that in devices like insulated gate bipolar transistors (IGBT) the thermo-mechanical stress is a major cause for failure. T.G Karayiannis and M.M. Mahmoud [4] published a review of the applications of micro-channel flow boiling in heat removal, and they mention that the International Technology Roadmap of Semiconductors (ITRS 2011) predicted the power dissipated by computer chips to be as high as $800W$ by 2026. The average heat flux in a desktop computer chip is expected to be as high as $4.5MW/m^2$ at that time. Since the hot-spots in these chips could be as high as six time the mean power [2], we would need to be prepared to remove fluxes as high as $30MW/m^2$. There is active research presently in the field of micro-channel flow boiling to address this issue. While researchers are looking into other means of heat removal such as heat pipes

and jet impingement techniques, there seem to be some issues such as integration into a closed loop circuit [3]. For a more detailed analysis on the applications of micro-channels flow boiling in heat removal, we direct the readers to Karayiannis *et al.* [4].

Apart from the on-earth applications, two-phase heat transfer also has an application in space based systems that involve refrigeration or thermal control systems. Over the past couple of decades there has been a growing interest in micro-gravity two-phase flow and heat transfer. Beside the above mentioned fields, two-phase heat transfer finds an application in other traditional means of heat transfer such as heat exchangers, petro-chemical processing, condensers and evaporators.

Vertical bubbly flows are commonly found in the above mentioned applications, and hence are of great interest to the two-phase flow community. In the present work, we address three important phenomena pertaining to bubbly flows, namely a) the rise velocity associated with a layer of bubbles rising near a vertical wall, b) the heat transfer due to a non-condensable bubble rising near a vertical wall, and c) the heat transfer associated with bubbles as they undergo boiling and condensation. These three cases cover many of the bubbly-flow related situations encountered in the industry.

Over the past couple of decades, with the rapid growth in computing power, there has been a growing interest in Computational Fluid Dynamics as an effective means to help us understand two-phase flow heat transfer. In the present work we develop an effective numerical approach to model two-phase flows involving phase change, and use it to study the aforementioned three phenomena.

2. STRATEGY

The heat transfer enhancement in two-phase flows can be broadly credited to two phenomena, namely the enhanced convection and mixing due to bubbly flows, and phase change in the form of boiling. Using computational fluid dynamics to study any physical process allows us to isolate the various phenomena involved, which can then be studied individually. A commonly encountered two-phase flow situation in the industry is vertical bubbly flow near a wall. Therefore, we first need to develop an understanding of the effect of bubbles rising under the influence of buoyancy near a vertical wall on the surrounding flow. In the present work, we employ the following strategy to understand two-phase flow and heat transfer:

1) We first examine the flow characteristics of a layer of bubbles rising near a vertical wall under the influence of buoyancy. We study the rise velocity of the bubbles and the velocity of the surrounding flow.

2) We then consider non-condensable gas bubbles moving in the vicinity of a heated wall. The effect of flow streamlines around the bubbles in the heat transfer enhancement at the wall is studied by considering a single bubble moving in a shear flow near the wall. We examine the effect of changing the various flow parameters in the form of commonly used non-dimensional groups on the wall-to-liquid heat transfer. We then consider the effect of a layer of non-condensable bubbles rising near a wall on the wall-to-liquid heat transfer.

3) Subsequently, build the numerical tool necessary to simulate boiling and condensation in two-phase flows, which we validate with experimental data from literature.

The numerical tool can then be used to simulate problems like flow boiling in micro-channels and nucleate pool boiling.

3. A LAYER OF BUBBLES RISING NEAR A VERTICAL WALL

3.1 Literature review

Having bubbles flow in a boundary layer can improve the mixing and convection in the viscous sub-layer, thereby, improving the heat transfer. A very commonly encountered flow configuration in industrial applications is the vertical flow of bubbles near a wall. Thus, it is useful to gain an understanding of vertical bubbly flows in order to understand two-phase heat transfer near vertical walls. Many studies have been performed to understand vertical bubbly flows which has created a large volume of literature on the subject [14–17, 60–65]. Moore [18, 19] characterized the rising motion of bubbles in viscous liquids. Bubbly flows have been seen to show different behavior in channels depending on the size of the bubbles [20]. It was found that the deformability of the bubbles controls their spatial distribution. The small bubbles that are less deformable have a lift force toward the channel wall in an upflow, while large deformable bubbles either have a zero lift force or one directed away from the wall. The change in the direction of the force results in the change in the distribution of the void fraction in the channel. Lu *et al.* [21] developed a model that predicts the laminar down-flow in a vertical channel for the case of nearly spherical bubbles. In vertical down-flow, the bubbles are pushed away from the wall and there exists a bubble free region near the wall that can be easily modeled. In the case of the up-flow of nearly spherical bubbles that are pushed to the wall, the flow is controlled by the rise of the bubbles near the wall. Therefore, it is of interest to understand the rising motion of bubbles near vertical walls.

There have been several studies on the motion of bubbles near walls but most have considered inclined walls. Masliyah *et al.* [22] studied the drag coefficient of bubbles rising near an inclined wall. They compared their results with theoretical results for

Stokes bubbles rising near a wall of a cylinder. Norman and Miksis [23] used the level-set method to simulate a two-dimensional bubble rising near an inclined wall. They observed a bouncing motion of the bubbles for large Reynolds. Maxworthy [24] performed experiments on a bubble rising under an inclined plate and Tsao and Koch [38] observed the bouncing motion of bubbles near inclined wall as well.

Krishna *et al.* [26] studied the wall effect on the rise velocity of bubbles in a vertical cylindrical column. They found that the effect of the wall on the rise velocity of bubbles to be dependent on the diameter ratio of bubble to column and a small column diameter can significantly reduce the rise velocity of a spherical cap bubble. Biswas [27] studied the deformation and rise velocity of the bubbles rising near a vertical wall and developed a one-dimensional volume averaged model based on their numerical results.

Most of the previous studies on the motion of bubbles near a wall are concentrated on the rise of bubbles in a stagnant environment. However, in many situations the rise of the bubbles itself or other flow conditions, such as a driving pressure gradient, creates a flow parallel to the wall near which the bubbles are rising. The goal of this paper is to study these types of flows and specially, characterize the rise of bubbles near a wall in the presence of a flow parallel to a wall.

3.2 Numerical method and problem set up

The gas-liquid flow is governed by the Navier-Stokes equations, which are written below for the entire domain:

$$\rho\frac{\partial \mathbf{u}}{\partial t}+\rho\nabla\cdot(\rho\mathbf{u}\mathbf{u}) = -\nabla p+\nabla\cdot\left\{\mu\left(\nabla\mathbf{u}+(\nabla\mathbf{u})^T\right)\right\}+\rho\mathbf{g}+\int_f \sigma\kappa\mathbf{n}\delta(\mathbf{x}-\mathbf{x}_f)d\mathcal{A}_f, \quad (3.1)$$

where continuity is expressed as:

$$\nabla\cdot\mathbf{u} = 0, \quad (3.2)$$

where ρ, μ, $\mathbf{u}$, p, and $\mathbf{g}$ are the local density, local viscosity, velocity, pressure, and the acceleration due to gravity, respectively. The effect of surface tension is taken

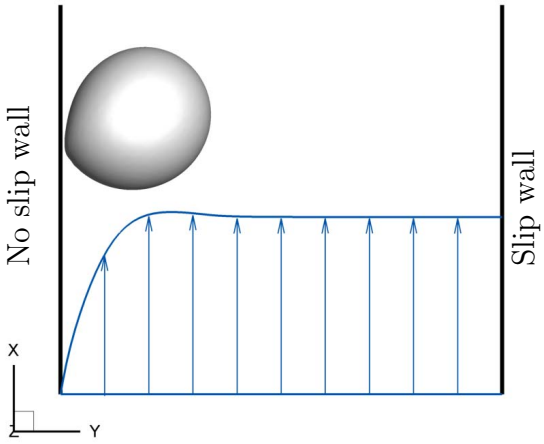

Figure 3.1. Schematic of the problem. No-slip wall on the left and slip wall on the right. Periodic boundary conditions in the x- and z-directions are used.

into account through the last term on the right hand side which represents it as a concentrated force on the interface "f". Here, σ, κ, $\mathbf{n}$, and δ denote surface tension coefficient, twice the mean curvature of the interface, unit vector normal to the interface, and the Dirac delta function, respectively.

The computations are done using a front-tracking/finite-volume method originally introduced by Unverdi and Tryggvason [28]. Various improvements as well as verification studies can be found in Tryggvason *et al.* [29] The method is based on the one-fluid formulation of the Navier-Stokes equations, where a single set of equations is solved for both the bubbles and the ambient liquid. The one-fluid formulation allows us to use a regular structured grid to solve for the flow and is the basis for a number of methods currently used for flows with sharp interfaces. In our approach the interface between the different fluids is identified by connected marker points that are advected by the fluid velocity, interpolated from the grid used to solve the fluid equations. Since the interest of this work is in the statistically steady state flow with

a constant number of bubbles of a given size, here bubbles are not allowed to coalesce. In addition, the range of parameters is such that bubbles do not break apart.

Figure 3.1 shows the schematic of the problem. The computational domain consists of a rectangular box with a no-slip wall on one side (-y) and a slip wall with on the other side parallel to the no-slip wall (+y). The two other directions have periodic boundary conditions.

The non-dimensional groups include the Archimedes number, Ar, and Eötvös number, Eo, defined as follow.

$$Ar = \frac{gd^3\rho_L(\rho_L - \rho_G)}{\mu_L^2}, \qquad Eo = \frac{gd^2(\rho_L - \rho_G)}{\sigma} \tag{3.3}$$

Here, d is the nominal diameter of the bubble, equal to the diameter of a sphere with the same volume, and subscripts L and G represent the liquid phase and the gas phase, respectively. The other dimensionless groups are density ratio and viscosity ratio which are chosen with values of $\rho_L/\rho_G = 50$ and $\mu_L/\mu_G = 10$ throughout this study.

The motion of bubbles near a solid surface may be influenced by other physical processes such as the disjoining pressure. Del Castillo *et al.* [30] showed that the terminal velocity of bubbles rising under an inclined wall at low inclination angles of 1°-5° is affected by the disjoining pressure. At larger angles, however, due to the increase in the effects of hydrodynamic forces, the influence of disjoining pressure on the terminal velocity becomes negligible. Therefore, these effects are not considered here. Even though the interest of this study is in the quasi-steady behavior of the flow the choice of initial conditions is still important. A poor choice of initial conditions could result in separation of the bubbles from the wall layer and drifting in the flow. For example, if a zero velocity is used as an initial condition, the rise of the bubbles in the stagnant domain will cause the bubbles to bounce on the wall. This could result in the bubbles moving out of the computational domain which is not desired. To avoid these possibilities, a uniform shear has been used as the initial condition of the flow. This shear flow creates a lift force on the bubble and pushes it toward the wall, preventing it from leaving the computational domain.

3.3 Results and discussion

The wall void fraction, ε_w, has been defined as the void fraction inside a layer of one diameter thickness next to the wall. By this definition, a wall packed with monodispersed spherical bubbles has a void fraction of $\pi/\sqrt{27} = 0.6046$ which can be used as only an estimation of maximum void fraction, since deformable bubbles are considered here. All of the presented results are scaled with d, $\sqrt{d/g}$, and $\rho_L d^3$ for length, time and mass, respectively. The results for the average rise velocity of the bubble relative to the wall, U_B, is reported in terms of bubble Reynolds number, Re_B which is based on the bubble diameter, d, and the liquid kinematic viscosity.

$$U_b = f(\rho_L, \rho_G, \mu_L, \mu_G, g, d, \sigma) \tag{3.4}$$

Since we are considering bubbles with negligible density and viscosity, the dimensionless parameters have the following form:

$$Re_b = f(Ar, Eo, \varepsilon) \tag{3.5}$$

$$Re_B = \frac{\rho_L U_B d}{\mu_L}, \qquad Re_L = \frac{\rho_L U_L d}{\mu_L}, \qquad Ar = \frac{g\rho_L d^3}{\mu_L^2}, \qquad Eo = \frac{\rho_L g d^2}{\sigma} \tag{3.6}$$

The simulations are performed by placing 1 to 16 bubbles near a vertical wall with an initial gap between the bubble and wall at 2% of the bubble's diameter. A dimensionless shear velocity profile of $u = y$ is used as the initial condition. The initial shear is chosen to keep the bubbles near the wall during the transient state. The bubble rising in a stagnant fluid will tend to bounce on the wall and could leave the computational domain. On the other hand, a bubble rising in a shear layer will have a lateral lift force toward the direction with larger velocity difference which is toward the wall in this case. This lift force will keep the bubbles near the wall. Eventually, due to the no slip boundary condition on the right wall, the flow will level off near the right boundary. However, the rising motion of the bubbles creates an average rise velocity in the liquid and an average shear near the wall which will keeps the bubbles there. The wall void fraction for all of the cases are kept the same at 15% by adjusting

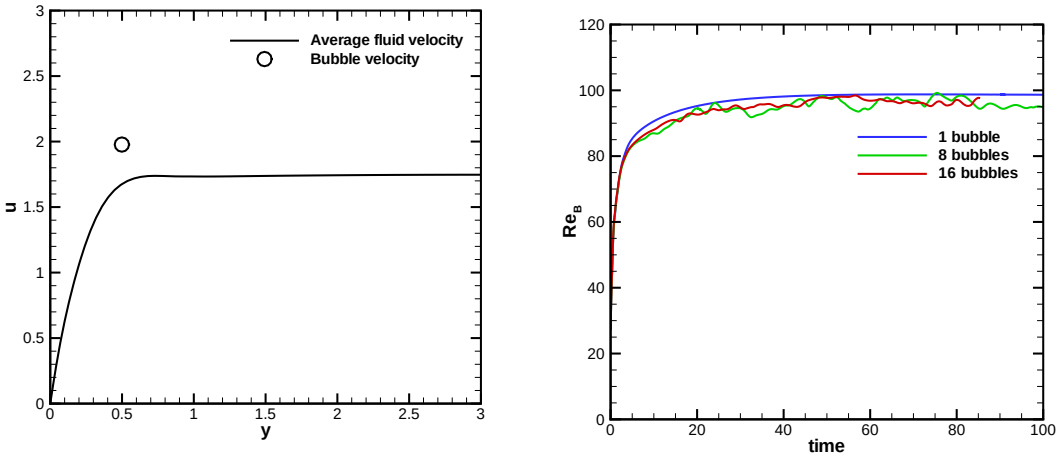

(a) (b)

Figure 3.2. (a)Average velocity profile and the velocity of the bubble for Eo=0.55, Ar=2400 and ε_w=0.15. (b)The average Reynolds number of bubbles for simulations with different number of bubbles.

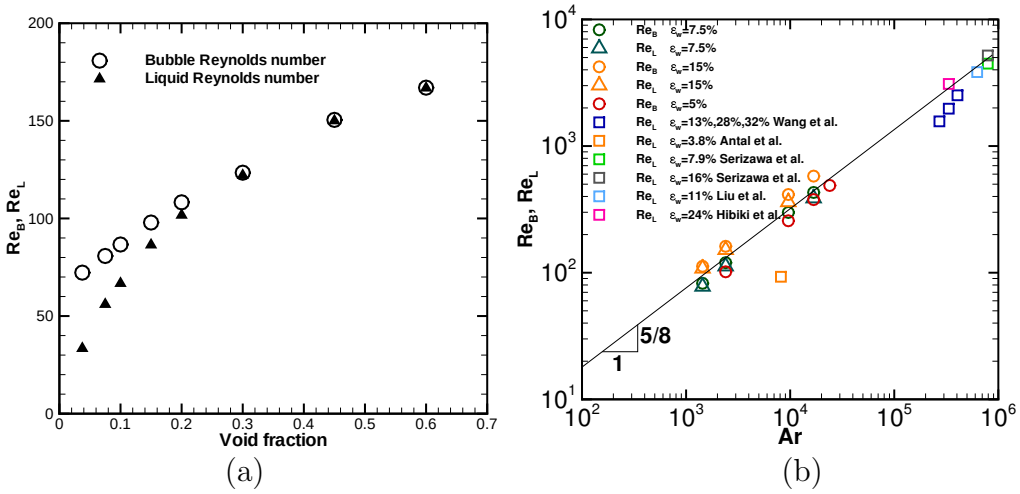

Figure 3.3. (a) Dependency of the bubbles Reynolds number and liquid Reynolds number on the wall void fraction at Ar=2400 and Eo=0.55. (b) Scaling of the liquid Reynolds number with Archimedes number at ε=0.15 and Eo=0.55.

the size of the computational domain in the x and z directions. As can be seen in figure 3.2(b), 8 bubbles and 16 bubbles simulations have essentially the same average bubble Reynolds number which is slightly less than the bubble Reynolds number for one bubble per domain. The case with one bubble per domain can be considered as a regular array of bubbles rising near a wall. Based on this observation, the rest of the simulations in this study have been performed using a single bubble in the computational domain with a matched void fraction. The average vertical velocity profile for the single bubble case is shown in figure 3.2(a). The velocity is averaged over planes parallel to the wall and plotted versus the distance from the wall, y. The rise velocity of the bubble and the location of its center is also shown in figure 3.2(a). As can be seen, the part of the domain away from the wall that only contains liquid phase, has a flat velocity profile due to the applied average pressure gradient that has balanced the weight of the liquid phase. The value of this average rise velocity of the liquid phase away from the wall is referred to as the liquid bulk velocity hereafter and is reported

in terms of a liquid bulk Reynolds number, Re_L, scaled with the bubble diameter and the kinematic viscosity of the liquid. The difference between Re_L calculated with one bubble simulation and 16 bubbles simulation is about 5%.

Both the rise velocity of bubbles and liquid bulk velocity vary significantly with void fraction on the wall as shown in figure 3.3(a). The void fraction is varied between 3.75% and 60%. A similar trend for the increase of the bubble rise velocity with void fraction has been observed for rising bubbles confined between two vertical walls [31, 32]. This is the opposite of the trend that has been observed for the rise velocity of bubbles in a homogeneous flow which has been found to decrease with the void fraction [33–35]. At a void fraction of 30% and above, the liquid phase away from the wall rises with the same velocity as the bubbles which gives matching values of Re_B and Re_L. This can be interpreted in the way that the wall is so covered by bubbles that the liquid phase on the other side of the bubble layer does not have any interaction with the wall anymore and only follows the motion of the bubbles. However, this does not mean that the relative velocity of the bubble and the liquid surrounding the bubble is zero, since the liquid on the left side of the bubble (figure **??**) rises at a lower velocity. As the wall void fraction drops below 30% the bulk velocity of the liquid falls below the velocity of the bubbles in such a way that the reaction force of the drag force on the bubbles on the liquid is balanced by the shear force on the wall. In the limit of zero void fraction, the liquid bulk velocity will go to zero.

A linear extrapolation of the bubble Reynolds number gives the value of $Re_B = 63.6$ at zero void fraction, *i.e.*, a single rising bubble. However, one should note that as the void fraction approaches zero, the liquid velocity also approaches zero. This leads to smaller shear near the wall and a smaller lateral lift force on the bubble. In the limit of single bubble, one expect the shear to be zero and the bubble start to bounce on the wall. This behavior was not observed in the lowest void fraction of 3.75% which is tested here.

The variation of the liquid Reynolds number with Archimedes number at a fixed Eo and wall void fraction is shown in figure 3.3(b). As it can be seen, the liquid Reynolds number scales with the Archimedes number to power 5/8.

For validation, the data from experiments on bubbly up-flow in circular channels, performed by Wang *et al.* [60] , Serizawa *et al.* [55], Liu and Bankoff [61] , and Hibiki *et al.* [56] , that were summarized in the work of R.V.Mukin [57], were used. The data from a similar work by Antal *et al.* [58] has also been used. These experiments measured the void fraction distribution along the diameter of the channel and the rise velocity of the liquid. In the present work, the void fraction for each set of data, has been calculated by averaging the void fraction distribution over a region near the wall having thickness equal to the bubble diameter. Re_B and Re_L were calculated by using the bubble diameter and rise velocity data from each work. Figure 3.3(b) shows that these experiments seem to agree well with the scaling that has been found. One may consider this simulation as a bubbly channel flow where all the bubbles has gathered near the wall and a single-phase uniform flow is present in the center of the channel.

Mendez-Diaz reported a criterion for the transition from core-peak void fraction to wall-peak void fraction on bubbly channel flows based on Reynolds number and Weber number of bubbles [16]. The criterion for wall-peak up-flow to occur is that Re_{rel} and We_{rel} (each of which is defined by using the bubble relative velocity) should be below 1500 and 8 respectively. The maximum Re_{rel} and We_{rel} in the present simulations were 53 and 0.16 respectively, which are well within the limits. fraction and increases the average density of the mixture at the center of the channel, reducing its rise velocity [21]. Since the average bubble velocity is larger than that of the surrounding fluid, large velocity gradients can be expected in the gap between the bubble and the wall. This would cause higher viscous stresses in the region as compared to the other regions in our domain. We shall refer to this region as the 'thin film' here after. We are interested in finding the variation of the viscous dissipation in the domain with the Archimedes number Ar.

Viscous dissipation is a useful quantity to analyze in the case of bubbly flows because it can be used in energy analysis. The steady state balance between the rate of change of potential energy of our system and viscous dissipation, as we will show in the present section, can be used as a means to check our computation of the Bubble reynolds number. One can also use simplifications such as the lubrication analysis, as we will see in a later section, to arrive at a scaling between the viscous dissipation and Ar. Once a scaling of the viscous dissipation is obtained, one could also proceed to find the drag coefficient on the wall. Since the average bubble velocity is larger than that of the surrounding fluid, large velocity gradients can be expected in the gap between the bubble and the wall. This would cause higher viscous stresses in the region compared to the other regions in our domain. We shall refer to this region as the 'thin film' here after. We are interested in finding the variation of the viscous dissipation in the domain with the Archimedes number Ar. Ar was varied by changing the value of μ_L and keeping all other parameters (i.e ρ_L, ρ_g, g, σ, R), constant. For incompressible flow, viscous dissipation can be written as:

$$\psi = \int_{Domain} \phi dV \qquad , \tag{3.7}$$

where,

$$\begin{aligned} \phi =& 2\mu \left[\left(\frac{\partial u}{\partial x} \right)^2 + \left(\frac{\partial v}{\partial y} \right)^2 + \left(\frac{\partial w}{\partial z} \right)^2 \right] + \\ & \mu \left(\left[\frac{\partial v}{\partial x} + \frac{\partial u}{\partial y} \right]^2 + \left[\frac{\partial w}{\partial y} + \frac{\partial v}{\partial z} \right]^2 + \left[\frac{\partial u}{\partial z} + \frac{\partial w}{\partial x} \right]^2 \right) \end{aligned} \tag{3.8}$$

From five simulations of different Archimedes numbers: $(1440, 2400, 9600, 16800, 24000)$, the viscous dissipation was computed for each case. A mechanical energy balance for our control volume would give:

$$\int_{Domain} \frac{\partial \rho(|\bar{v}|^2/2)}{\partial t} dV + \iint \rho \left(\frac{|\bar{v}|^2}{2} \right) (\bar{v}.\hat{n}) dA + \frac{d(P.E_{sys})}{dt} = - \int_{Domain} \phi dV \tag{3.9}$$

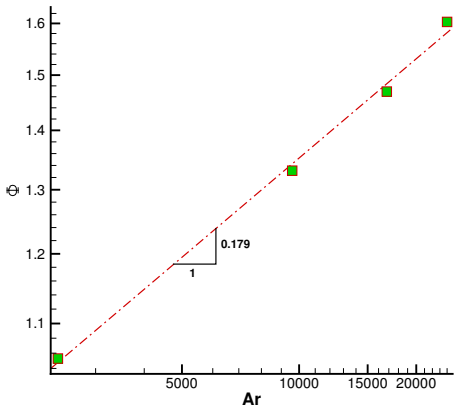

Figure 3.4. Variation of non-dimensional viscous dissipation with Archimedes number Ar.

The viscous dissipation per unit volume ϕ and viscous dissipation ψ, can be non-dimensionalized as:

$$\Phi = \frac{\psi}{\rho_l g^{3/2} d^{7/2}} \tag{3.10}$$

$$\phi^* = \frac{\phi}{\rho_l g^{3/2} d^{1/2}} \tag{3.11}$$

In equation 3.9, $P.E_{sys}$ is the potential energy of our system (which includes the bubble and surrounding water).Since we have periodic boundary conditions at the 'x' ends of the domain and the component of velocity normal to every other surface is zero, the second term in the above equation is zero. Left hand side of equation 3.9 was compared with the viscous dissipation and there was a match of about 98% between the two.

As the system approaches steady state, the first term in equation would tend to zero and the viscous dissipation would tend to the rate of change of Potential Energy. It was observed that $\frac{d(P.E_{sys})}{dt}$ reached a steady value before viscous dissipation did, and hence its value was used as steady state viscous dissipation in our analysis. Since Figure 3.3(b) shows that the Re_B (a measure of bubble velocity, related to rate of change of $P.E$ of the system) increases with Archimedes number, from equation (12) we would also expect Φ to increase with Ar. This trend can be seen in figure 3.4. A linear fit in the log-log plot reveals that:

$$\Phi \propto (Ar)^{0.179} . \tag{3.12}$$

Due to continuity of stress across the bubble interface, and the fact that in the present study is focussed on clean bubbles (without any surfactants or contaminants), a 'free slip' velocity field is observed at the bubble interface. There is no rotating or tank treading motion of the bubble due to shear at the interface. When the bubble gets close to the wall, a thin film of liquid is formed between the bubble and the wall. Due to the relative velocity between the bubble and the wall, viscous dissipation in the film becomes significant. The minimum distance between the bubble and the wall can be called the minimum film thickness. Since the bubble pushes the

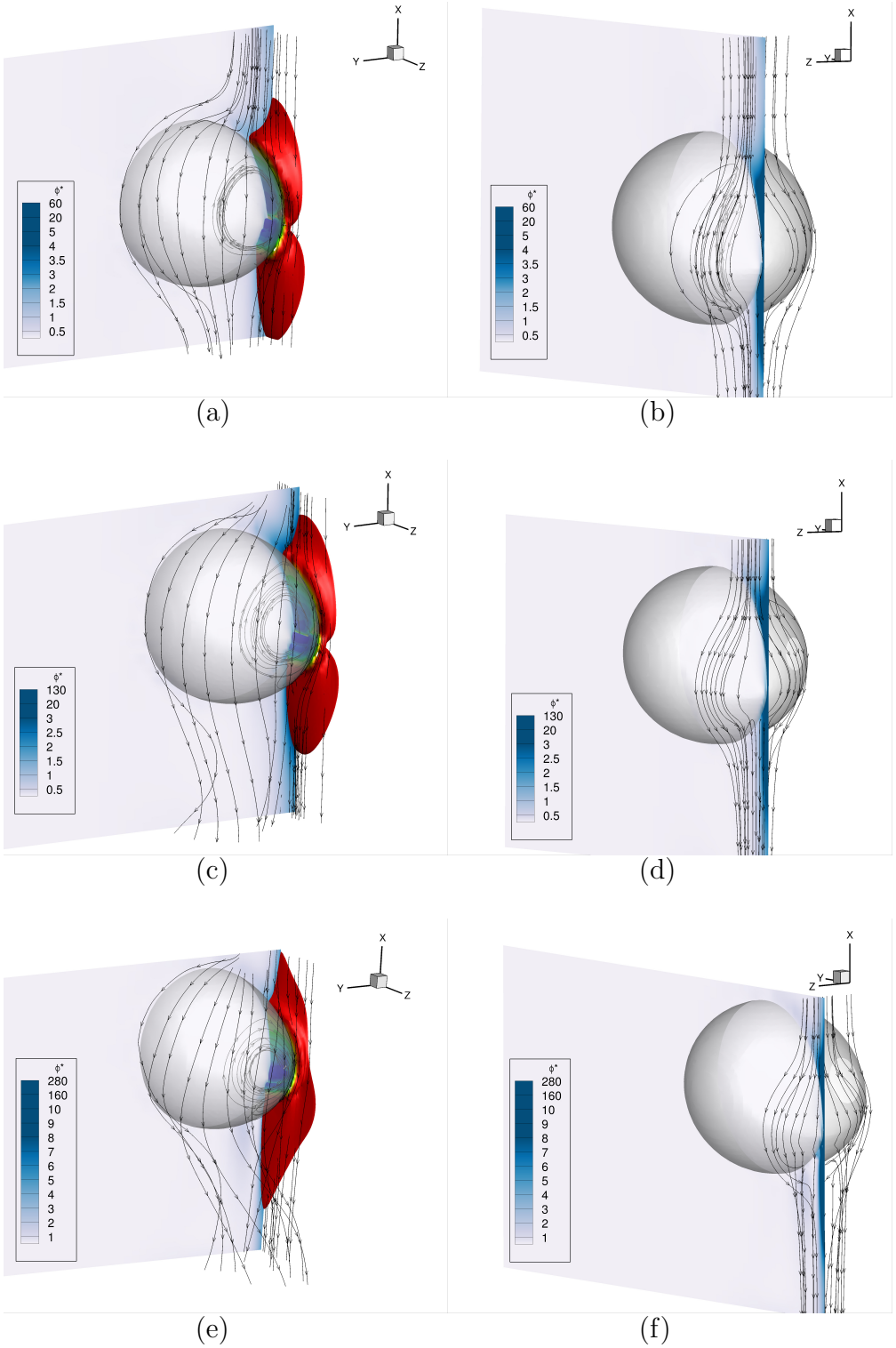

Figure 3.5. (a),(c),(e):Streamlines in the frame of reference of the bubble, Iso-contours of ϕ^* on a slice through the bubble and the red region which accounts for 35% of total dissipation for Ar=1440 ,Ar=2400, Ar=9600. (b),(d),(f): Streamlines of strained flow between bubble and the wall in a frame moving with the bubble for Ar= 1440 ,Ar=2400, Ar=9600.

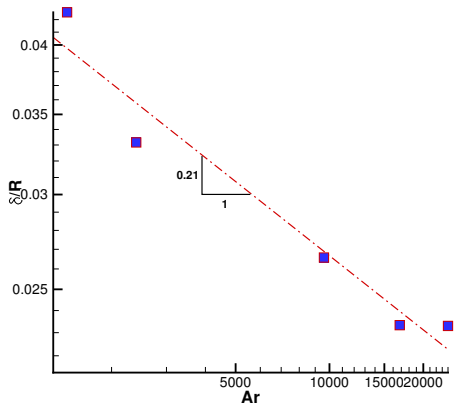

Figure 3.6. Variation of minimum film thickness with Archimedes number Ar.

surrounding fluid in the upward direction as it rises, we can expect higher values of u downstream compared to upstream, leading to greater viscous dissipation downstream of the bubble. This can be seen in figures 3.5(a),(c) and (e). The red region accounts for 35% of the total viscous dissipation. Streamlines seen in the flow visualization are shown in the frame moving with the bubble.

Figures 3.5(b),(d) and (f) show the strained flow in the film region. It can be seen that near the bubble, the stream lines diverge, causing the relative velocity of the surrounding fluid with respect to the bubble to reduce. Since the wall has a no slip boundary condition, it has a relative velocity equal to the velocity of the bubble in magnitude, but in the $-x$ direction. Thus we have high velocity gradients arising in the film, causing viscous dissipation. From these simulations it is observed that the film thickness attains a steady state value. Since the bubble is in a shear flow, it experiences a lift force towards the wall. There is a build up of pressure due to the flow taking place in the thin gap between the bubble and the wall. It was observed that the bubble interface becomes nearly flat close to the wall (which would enable us

to use the assumption of lubrication for this flow, as we will see in a later section).This build up of pressure balances the lateral lift.

It was found that if the initial shear is decreased to 66 % of what was used, the steady state film thickness changes only by 2.5 % .We believe that the steady state film thickness should be largely independent of the initial shear. The initial shear condition has been used only to make sure that the bubble does not bounce off the wall. The film thickness at steady state would depend on the shear that exists in the flow around the bubble at steady state, which is primarily a function of non-dimensional numbers such as Eotvos number, Archimedes number etc. Film thickness δ has been non-dimensionalized by dividing it with R, the bubble radius. From figure 3.6, we see that a linear fit in the log-log plot reveals the following correlation between the steady state film thickness and Ar:

$$\frac{\delta}{R} = 0.18 Ar^{-0.21} \tag{3.13}$$

Dissipation method has been used in the past to find drag force on a spherical bubble rising in an unbounded quiescent liquid. Harper [59] showed that the dissipation in the boundary layer of a bubble rising in quiescent liquid is negligible compared to the viscous dissipation in the bulk of the liquid outside the boundary layer. Using a scaling argument he was able to fine the scaling of the viscous dissipation and by matching it with the rate of change of potential energy he found a scaling for rise velocity of bubbles which matches the experimental observations that is the linear scaling of the Reynolds number with Archimedes number. This leads to an inverse scaling of the drag coefficient of the bubble with the Reynolds number. Here we apply the dissipation method to find a scaling for the rise of bubbles near a vertical wall.

We have observed that the viscous dissipation is very large in the film layer that forms between the bubble and the wall. Here, we assume that the main contribution to the viscous dissipation comes from this region. Let's assume that the minimum film thickness is δ and the size of the film is L (in both streamwise and spanwise directions.) The viscous dissipation per unit volume in the film layer scales with

$\phi = O(\mu U^2/\delta^2)$. This will not be the case if the interface was parallel to the wall since the interface has a slip boundary condition. The cause of this dissipation comes from the slope of the interface. Considering a simple lubrication theory analysis one can find the scaling to be as above. The volume of the film is $V = O(\delta L^2)$ and the total viscous dissipation is $O(\mu U^2 L^2/\delta)$ which should match the potential energy release rate $\frac{d(PE)}{dt} = O(\rho g R^3 U)$, R being the bubble radius. This should give us:

$$\rho g R^3 U \propto \frac{\mu U^2 L^2}{\delta} \tag{3.14}$$

This is not enough to find the scaling law as there are two more unknowns L and δ for which we do not have a scaling yet. However, we can make two more scaling arguments. One is about the pressure build up in the film layer. From lubrication theory the pressure build up in the film is $\Delta P = O(\mu U L/\delta^2)$. Since the interface near the film layer is almost flat, the pressure build up should be of the order of capillary pressure, $\Delta P = O(\sigma/R)$. Moreover there is a lift force on the bubble towards the wall that is balanced by the pressure build up in the film layer. The pressure force will be $F_L = O(\mu U L^3/\delta^2)$ and this should scale with the $(C_L \rho U^2 R^2)$. Here, C_L is the lift coefficient of a bubble rising in a shear layer. Thus, we have:

$$\mu \frac{UL}{\delta^2} \propto \frac{\sigma}{R} \tag{3.15}$$

$$\mu \frac{UL}{\delta^2} L^2 \propto C_L \rho U^2 R^2 \tag{3.16}$$

The lift force also depends on the shear rate which in our case is going to scale with U/R. The reason is that the liquid rise velocity away form the wall is very close to the bubble rise velocity U. These three scaling arguments are enough to find the scaling laws for three unknowns U, L, and δ. By using equations (17),(18) and (19), we find that in the dimensional form the scaling law for velocity turns out to be:

$$U \propto \left(\frac{\rho R^5 g^4 \sigma}{C_L^3 \mu^2} \right)^{1/8} \tag{3.17}$$

In dimensionless form, this would be:

$$Re \propto \left(\frac{Ar^5}{C_L^3 E_o} \right)^{1/8} \tag{3.18}$$

Considering that the lift coefficient of the bubble in shear is almost constant for $Re > 10$ [**?**], we get from equation (21), that $Re \propto Ar^{5/8}$. The line shown in Figure. **??**(b) has slope 5/8 and it can be seen that our numerical results and the experimental results used for validation from other papers, match the scaling derived.

If we re-arrange the left hand size of equation (17), we have:

$$\frac{\mu U^2 L^2}{\delta} \propto \left(R^2 g \mu\right) \left(\frac{\rho U R}{\mu}\right) \tag{3.19}$$

$$\Rightarrow \frac{\mu U^2 L^2}{\delta} = \psi \propto \rho g^{3/2} R^{7/2} . \frac{Re}{Ar^{1/2}} \tag{3.20}$$

We have from equation (13), that $\Phi = \frac{\psi}{\rho_l g^{3/2} d^{7/2}}$. If we use $Re \propto Ar^{5/8}$, we have:

$$\Phi \propto Ar^{1/8} \sim Ar^{0.125} \tag{3.21}$$

We see that this is not quite close to the scaling we have in equation (15) and this could be due to the following reasons. While the scaling derived in the above analysis applies to the viscous dissipation in the region between the bubble and the wall, the viscous dissipation we found in the earlier analysis, i.e., equation (15) is for the entire domain. Also, since the $\Phi \propto \frac{Re}{Ar^{1/2}}$, a small error in Re would result in a large percentage error of Φ. i.e., if $Re \propto Ar^n$ and hence $\Phi \propto Ar^m$ where $m = n - 0.5$,

$$\frac{\Delta m}{m} = \frac{\left(\frac{\Delta n}{n}\right)}{1 - \frac{1}{2n}} \tag{3.22}$$

We see that for $n = 0.625$, the percentage error in m is that of n magnified by a factor of 5.

When we re-arrange the terms equation (17) use the result derived in equation (21), and use the relation $Re \propto Ar^{5/8}$ we get:

$$\left(\frac{\delta}{R}\right) \propto \frac{Ar^3}{Re^5} \propto (Ar)^{-0.125} \tag{3.23}$$

Again, we observe a significant deviation from the scaling found in equation (16) because firstly, the δ which is found in the scaling analysis signifies the 'average' distance between bubble and wall where the lubrication theory is applicable, while

the δ in equation (16) is the minimum distance of the bubble from the wall at steady state. Secondly, we can do a similar analysis as done in equation (25) and show that the relative error in the power of Ar in equation (26) would be 25 times the relative error in n. n being 5/8.

3.4 Summary

The rising motion of bubbles near a vertical wall with a uniform flow in the liquid phase parallel to the wall has been simulated. An average pressure gradient is applied to the domain to balance the weight of the liquid phase. The rising motion of the buoyant bubbles drag the liquid upward creating the uniform flow in the liquid phase away from the wall. The rise velocity of the bubble and the liquid has been calculated for different wall void fractions and different values of Archimedes numbers. A scaling has been found between the liquid rise velocity and Archimedes number. Using this law, the flow rate of laminar bubbly flow in vertical channels has been predicted and compared with previous studies.

Since the liquid trapped between the bubble and the wall (in the film region) is dragged upwards by the rising bubble, a high viscous dissipation rate was observed in the film. This viscous dissipation has been correlated with Archimedes number and a scaling has been found between the two. The minimum distance between bubble and wall ('film thickness') was found to attain a steady state value. A scaling has been found between the steady state film thickness and Archimedes number. A scaling analysis built by using lubrication theory, lift force on the bubble and energy conservation showed that the bubble rise reynolds number would be proportional to $Ar^{5/8}$ which is in agreement with our finding. The scaling of bubble reynolds number is also in agreement with the experimental findings from studies conducted by different research groups.

4. EFFECT OF NON-CONDENSABLE BUBBLES ON WALL-TO-LIQUID HEAT TRANSFER

4.1 Literature review

The high rate of heat transfer associated with bubbly flows can be attributed to two important phenomena: Firstly, phase change, wherein a high heat transfer coefficient is observed due to the high latent heat of vaporization of the liquid phase; Secondly, the enhanced convective effect of bubbly flows. In the present study, we examine the latter. Some experimental studies have indicated that rising bubbles affect the thermal boundary layer near the wall. Tokuhiro *et al.* [5] indicated as much as two to threefold increase in local heat transfer coefficients in the presence of small bubbles near a heated wall for low values of wall heat flux. Since this heat transfer enhancement occurred due to the bubble-induced turbulence in the thermal boundary layer, bubbles smaller than the thermal boundary layer thickness led to higher heat transfer rates compared to larger bubbles. The presence of bubbles increases the convective heat transfer by buoyancy [6]. Kitigawa *et al.* [7] performed $2D$ simulations to show that the local heat transfer coefficient can be increased to around 2.2 times that of a single phase flow if sub-millimeter bubbles are injected in the channel. Their results suggest that the increased convection due to bubbles contributed more strongly to the heat transfer enhancement than mixing. Studies have shown that the presence of bubbles modifies the flow pattern thereby enhancing the heat transfer coefficient [8,9]. Computational fluid dynamics has been used as an effective tool to study bubbly flow heat transfer over the past couple of decades. Mehdizadeh *et al.* [50] used VOF [51] to simulate heat transfer in a slug bubble flow through a micro-channel.They found the thin film between the bubble and wall to contribute significantly to the wall heat transfer. Dabiri *et al.* [10] showed by using direct numerical simulation (DNS) of

bubbly up-flow that a 3% increase in volume fraction could lead to an improvement in the Nusselt number of about 60% . They used the front tracking method [28,29] for their simulations. By performing DNS of rising bubbles in a channel, Deen *et al.* [12] showed that the heat transfer coefficient peaked near the bubble. They observed a decrease in the heat transfer downstream of the bubble due to the thickening of the thermal boundary layer. They also observed an increase in the heat transfer coefficient when there was a coalescence between bubbles. Babin *et al.* [11] performed an experimental study on the effect of a single rising slug bubble in a vertical channel on the wall heat transfer and found an enhancement of up to 60 % in the wake of the bubble.

The flow patterns around a bubble moving in a shear flow have been investigated in studies such as Wang *et al.* [54] numerically. Kossack *et al.* [41], and Mikulencak *et al.* [40] investigated flow patterns around cylindrical objects in shear flows. It can be seen from a comparison between Wang *et al.* [54] and Kossack *et al.* [41] that inviscid shear flow around a cylinder can be used to approximate the flow patterns around a bubble.

There are several studies such as Hikita *et al.* [46], Mersmann *et al.* [47], and Deckwer [48], that proposed correlations between the heat transfer coefficient and various non-dimensional groups like Reynolds number, Froude number, and Prandtl number. For a detailed review of the various studies dealing with heat transfer correlations for bubble columns, refer to Kantarci *et al.* [49].

From an examination of existing literature, we see while there is an abundance of studies proposing heat transfer correlations for bubbly up-flow, that there is a lack of studies relating the flow pattern around a rising bubble to the heat transfer coefficient at the wall. Also, most of the proposed correlations in past studies apply to specific flow situations such as flow in a circular channel or a square channel and predict the aggregate/bulk effect of bubbly flow. There is a lack of studies predicting the localized effect of individual bubbles on the wall-to-liquid heat transfer. The aim of the present chapter therefore, is to find the local impact of a single bubble rising in a

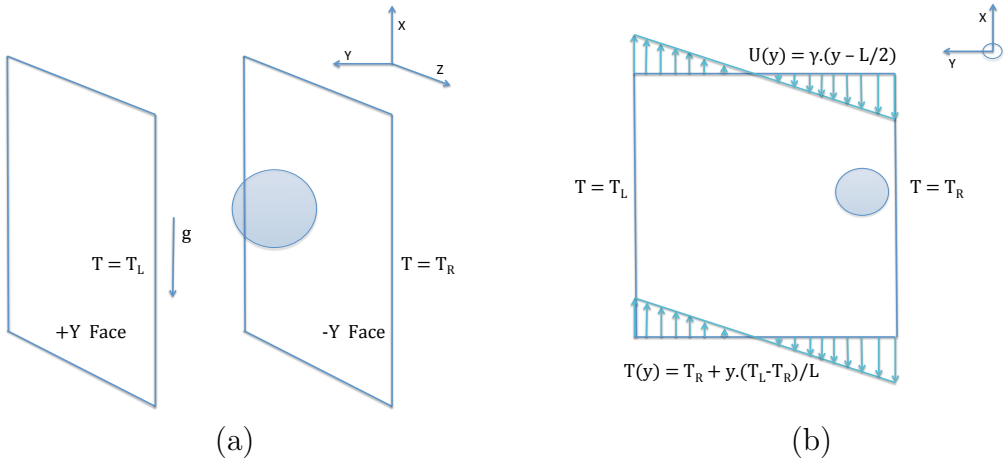

Figure 4.1. (a) $3D$ view of the problem set up (b) Walls maintained at $T^* = 0$ and 10, Initial condition for velocity: $U = \dot{\gamma} y$.

shear flow near a wall on the wall-to-liquid heat transfer. Shear flow is chosen to be the background flow since both internal and external flows can be approximated to be shear flows close to the wall, and given the shear rate at the wall we can apply the findings of the present work to a generic case provided the bubble diameter is small enough. In the present chapter, we will examine the impact of a single bubble on steady and transient heat transfers at the wall. In the former case, the bubble is at thermal equilibrium in a Couette flow with a linear temperature profile. In the latter case, the bubble rises in a Couette flow undergoing a transient heat transfer from the wall.

4.2 Problem Definition and set up

We wish to simulate a bubble rising in a shear layer near a wall. To achieve this we consider a computational domain shown in Figures 4.2 (a) and (b). We impose no-slip boundary conditions on the $-Y$ and $+Y$ faces of the domain. The separation between the $-Y$ and $+Y$ faces is $L = 10d$. The $-Y$ face acts as the wall near the

bubble. The $+Y$ face serves to approximate the flow far away from the wall, which is a shear flow profile. Initially, the $-Y$ and $+Y$ faces have equal but opposite u velocities such that a Couette flow profile of shear rate $\dot{\gamma}$ is created in between them. The presence of the $+Y$ face has negligible effect on the heat transfer enhancement seen on the $-Y$ wall since L is an order of magnitude larger than the bubble diameter. We impose a free-slip or zero shear boundary condition on the $-Z$ and $+Z$ faces of the computational domain and the inflow and outflow boundary conditions on the $+X$ and $-X$ faces respectively. The gravity acts along the $-X$ direction.

Bubbles rising near a wall may undergo a bouncing motion against the wall [37–39]. In the present study, we initialize the position of the bubble close to the wall. The initial distance between the bubble center and the wall is $1.04r$, where r is the bubble radius. Previous studies have shown that nearly spherical bubbles tend to experience a lift force pushing them towards the wall in an up-flow. An earlier work by the authors [42] found the steady state distance between a bubble and a wall during the bubble rise to be dependent only on the shear. The steady state thickness of the thin film region between the bubble and the wall is such that the pressure build-up in the lubrication region balances the lift force experienced by the bubble. Since the focus of the present study is the effect of steady state flow patterns around a non-condensable bubble on heat transfer, phenomena such as bubble nucleation or bubble formation have not been modeled.

In the present work, we are interested in two scenarios: First, we consider a case with a linear temperature profile between the walls as the initial condition, i.e. a uniform temperature gradient $\left(\frac{\partial T^*}{\partial y^*}\right)_0 = 1$. We define the dimensionless position vector $\vec{x}^*$, temperature field T^* and time t^* according to equation 4.1:

$$\vec{x}^* = \frac{\vec{x}}{d};\ T^* = \frac{T - T_R}{\left(\frac{\partial T}{\partial y}\right)_0 d};\ t^* = t\dot{\gamma}. \tag{4.1}$$

We consider a computational domain of the following dimensions: $(L_x^*, L_y^*, L_z^*) = (30, 10, 20)$. The bubble's initial location is $y^* = 0.54$. The right and left walls are maintained at dimensionless temperatures $T_R^* = 0$ and $T_L^* = 10$, respectively, where

T_L^* and T_R^* are defined according to equation 4.1. The subscripts R and L correspond to the right and left or $-Y$ and $+Y$ faces, respectively. Figure 4.1 (a) and (b) show $3D$ and $2D$ views of the setup, respectively. In the second case, the liquid is at a bulk temperature $T^* = 0$. At $t^* \geq 0$, the right wall temperature is maintained at $T_R^* = 1$ and during the process of transient diffusion, at a point when the thickness of the thermal layer $\delta_T \sim d$, we introduce the bubble into the domain to examine its impact on the transient heat transfer. The closed form solution for the second case described above in the absence of the bubble is as follows:

$$T^*(y^*, t^*) = 1 - erf\left(\frac{y^*\sqrt{Re_{d,\dot{\gamma}}Pr}}{2\sqrt{t^*}}\right), \tag{4.2}$$

$$\overline{q''(t^*)} = \sqrt{\frac{Re_{d,\dot{\gamma}}Pr}{\pi t^*}}. \tag{4.3}$$

Here, $Re_{d,\dot{\gamma}}$ is the Reynolds number defined using the shear rate $\dot{\gamma}$ and the bubble diameter, Pr is the Prandtl number, and $\overline{q''}$ is the heat flux at the wall normalized by dividing with $\frac{k\Delta T}{d}$. δ_T is defined such that:

$$T^*(\delta_T^*, t_0^*) = 0.1 \tag{4.4}$$

The starting time of the simulation t_0^* is calculated by substituting $T^* = 0.1$ and $y^* = 1$ into equation 4.2. Throughout all our simulations, we use the following values of parameters mentioned above. For all the computations, we keep Pr constant at 4.0.

4.3 Numerical method

The gas-liquid flow is governed by the Navier-Stokes equations, which are written entire domain

$$\rho\frac{\partial \mathbf{u}}{\partial t} + \rho\nabla\cdot(\mathbf{uu}) = -\nabla p + \nabla\cdot\left\{\mu\left(\nabla\mathbf{u} + (\nabla\mathbf{u})^T\right)\right\} + \rho\mathbf{g} + \int_f \sigma\kappa\mathbf{n}\delta(\mathbf{x}-\mathbf{x}_f)d\mathcal{A}_f \tag{4.5}$$

$$\nabla\cdot\mathbf{u} = 0, \tag{4.6}$$

where ρ, μ, $\mathbf{u}$, p, and $\mathbf{g}$ are the local density, local viscosity, velocity, pressure, and the acceleration due to gravity, respectively. The effect of surface tension is taken into account through the last term on the right hand side which is represented as a concentrated force on the interface "f". Here, σ, κ, $\mathbf{n}$, and δ denote the surface tension coefficient, twice the mean curvature of the interface, unit vector normal to the interface, and the Dirac delta function, respectively.

The computations are done using a front-tracking/finite-volume method developed by Unverdi and Tryggvason [28]. There have been many improved versions of this method and they can be found in Tryggvason *et al.* [29] In this method, we solve a single set of Navier-Stokes equations for the entire domain, by using Eulerian grids. The liquid-vapor interface is represented by a front consisting of a network of interconnected marker points. These individual marker points are advected at each time-step by using the surrounding velocity field computed from the Navier-Stokes equations.

To solve for the temperature distribution, we use the standard temperature transport equation:

$$\frac{\partial T}{\partial t} + u_i \frac{\partial T}{\partial x_i} = \frac{1}{\rho C_p} \frac{\partial}{\partial x_i} \left(k \frac{\partial T}{\partial x_i} \right), \tag{4.7}$$

The above equation was solved by using a fully explicit time advancement scheme. For the diffusion of temperature, a central difference scheme was used and for the advection of temperature, the QUICK scheme was employed. In the present work, we do not consider the phase change phenomenon. We are mainly interested in the effect of a gas bubble on the convective heat transfer.

We aim to keep the bubble almost stationary in the computational domain to take advantage of the local mesh refinement. To achieve this, after each time step we move from one inertial frame of reference to another with a non-zero relative velocity such that the bubble remains almost fixed. The value of the relative velocity is calculated by a simple PI controller with a signal from the location of the center of the volume of the bubble. Note that this method is different from solving the constitutive equations

in a non-inertial frame of reference attached to the bubble. After each time-step, the u and w velocity fields are updated by subtracting the bubble velocity from them.

$$\frac{u^{n+1} - u'^{n}}{\Delta t} = -R'^{n}_{c,x} + R'^{n}_{\nu,x} - \frac{P^{n+1}_{i+1} - P^{n+1}_{i}}{\rho \Delta x} - \left(1 - \frac{\rho_l}{\rho}\right) g \tag{4.8}$$

$$\frac{w^{n+1} - w'^{n}}{\Delta t} = -R'^{n}_{c,z} + R'^{n}_{\nu,z} - \frac{P^{n+1}_{k+1} - P^{n+1}_{k}}{\rho \Delta z}, \tag{4.9}$$

where, $R'^{n}_{c,x}$, $R'^{n}_{\nu,x}$, $R'^{n}_{c,z}$, $R'^{n}_{\nu,z}$, are the advective and viscous terms in the Navier-Stokes equations of the x and z momenta, respectively, evaluated at the n^{th} times step. For the y momentum, we use the standard Navier Stokes equation with u'^{n} and w'^{n} as the x and z velocities respectively. P^{n+1}_{i} is the pressure at $n + 1^{th}$ time step and the i^{th} node along x direction (similarly, k for z directions). In order to prevent the liquid from falling, we apply a pressure gradient along the x direction that balances the weight of the liquid. This can be seen in the last term of equation 4.8. We used the QUICK scheme to evaluate R'^{n}_{c}, and a central difference scheme to evaluate R'^{n}_{ν}. As mentioned earlier, we have:

$$u'^{n} = u^{n} - u^{n}_{b} \tag{4.10}$$

$$w'^{n} = w^{n} - w^{n}_{b}, \tag{4.11}$$

where,

$$u^{n}_{b,i} = \int\int\int_{V} u^{n}_{i}(1 - I) dV, \tag{4.12}$$

where,$i = 1, 2, 3$ for x, y, z, respectively. I is the color function which is 0 for the gas phase and 1 for the liquid phase. The above integral is performed over the volume of the domain.

The boundary conditions for the momentum equations are as follows: The right and left walls initially move with x velocities of $-U$ and $+U$, in the lab frame of reference, in order to create a shear rate $\dot{\gamma} = \frac{2U}{L}$. Depending on the shear rate that we wish to impose, we can compute the value of U. At each time step, we find the u velocity component to be imposed as boundary conditions on the left and right walls

by subtracting the increment in bubble velocity at the previous time step from the u-boundary conditions at the previous time step. The z velocity on these walls is 0. For the $-Z$ and $+Z$ walls, we impose zero-shear boundary conditions. All the walls, except the $+X$ and $-X$ ones, are impermeable. We impose a zero velocity gradient boundary condition, i.e., $\frac{\partial u_i}{\partial n} = 0$ for $i = 1, 2, 3$, on the $+X$ and $-X$ walls. The initial condition everywhere in the domain is: $u(y) = -U + \dot{\gamma}y$, where $U = \dot{\gamma}L/2$.

For the energy equation, in the steady state case, we have $-Y$ and $+Y$ walls maintained at T_R and T_L,respectively. At $t = 0$, we have a temperature profile: $T^*(y^*) = y^*$. On the $-Z$,$+Z$, $-X$ and $+X$ faces, we have adiabatic boundary conditions. In the transient case, we impose a Dirichlet boundary condition $T = T_R$ on the right wall $(-y)$. We impose the analytical solution for the single phase flow shown in equation 4.2 as an inflow boundary condition on the $+X$ face. Adiabatic boundary conditions are imposed on the $-X, -Z, +Z$ and $+Y$ faces.

It is to be noted that if T^* is the solution to Equation 4.7 with the boundary conditions $T^*(y = 0) = 0$, and $T^*(y = L_y) = T_1^*$, then it can be shown that $T' = T_1^* - T^*$ is also a solution to Equation 4.7 with boundary conditions $T'(y = 0) = T_1^*$, and $T'(y = L_y) = 0$. Hence, as long as the Energy equation has no source term, whether the wall near the bubble is hot or cold has no impact on resulting magnitudes of temperature gradients observed at the wall. Therefore, the results obtained in the present work will also apply to cases where the bubble moves near a hot wall, although in the present work we simulate bubble motion near a cold wall.

In order to verify the numerical method described we first use it to solve the case of a bubble rising in a Couette flow with a steady temperature gradient. We then simulate the same problem using a steady inertial frame of reference moving with a constant velocity. After that, we compare the results of both simulations at different times before the bubble attains its steady state velocity. Figure 4.2 shows the superimposition of dimensionless wall normal temperature gradients along the center line at different times for the two methods explained. The wall normal temperature is made dimensionless using the single phase wall normal gradient. We use the verified

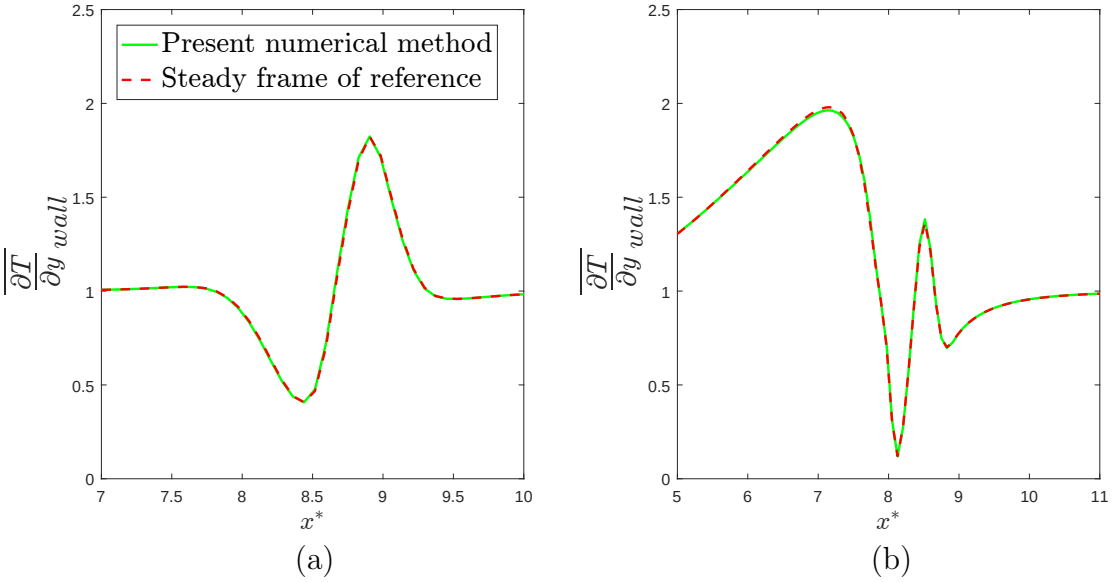

Figure 4.2. Superimposition of the distribution of wall normal temperature gradient along the centerline using the proposed numerical method and a steady inertial frame of reference, respectively, at $t^* =$ (a)0.63 and (d)5.7.

numerical approach discussed in Section 4.3 for all the simulations henceforth in the present work.

4.4 Dimensionless parameters and the fractional improvement in Nusselt number

We note that the heat transfer coefficient at the wall depends on the following parameters:

$$h = f(d, \sigma, \mu, \dot{\gamma}, g, C_p, \rho, k). \tag{4.13}$$

All the variables used in the above equation are for the liquid phase. After performing dimensional analysis with g, K, d and μ as the primary variables, we have:

$$Nu_d = f\left(La, \overline{\dot{\gamma}}, Pr, Ar\right), \tag{4.14}$$

where Nu_d, La, $\bar{\dot{\gamma}}$, Pr and Ar are the Nusselt number defined using bubble diameter, Laplace number, Non-dimensional shear rate, Prandtl number, and Archimedes number respectively and are defined as follows:

$$Nu_d = \frac{hd}{k} \; ; \; La = \frac{\sigma \rho d}{\mu^2} \; ; \; \bar{\dot{\gamma}} = \dot{\gamma}\sqrt{\frac{d}{g}} \; ; \; Pr = \frac{\mu C_p}{k} \; ; \; Ar = \frac{g d^3 \rho^2}{\mu^2}. \tag{4.15}$$

It is to be noted that while $\overline{Nu}$ may depend on other non-dimensional groups like $\frac{\rho_l}{\rho_g}, \frac{Cp_l}{Cp_g}, \frac{K_l}{K_g}$, subscripts l and g corresponding to liquid and gas phases, respectively, such non-dimensional groups are not of interest in the present study. We define a dimensionless parameter to quantify the improvement in heat transfer due to the bubble in the steady and transient problems as follows: Assume q_s'' to be the analytical heat flux at any time for the single phase problem under the same boundary conditions, and q'' to be the heat flux for the two-phase problem in the presence of the bubble. The enhanced heat transfer due to the bubble occurs in a small area equal to the projection area of the bubble $A_b = \pi R^2$, and we define:

$$\Delta Q = \int\int_A q'' dA - \int\int_A q_s'' dA, \tag{4.16}$$

$$q_b'' = \frac{\Delta Q}{A_b}. \tag{4.17}$$

We can then define Δh, the increment in the local heat transfer coefficient as:

$$\Delta h = \frac{q_b''}{\Delta T}. \tag{4.18}$$

The local increment in the Nusselt number ΔNu, and the local fractional improvement in the Nusselt number $\overline{Nu}$ are defined as:

$$\Delta Nu = \frac{\Delta h d}{k} \tag{4.19}$$

$$\overline{Nu} = \frac{\Delta Nu}{Nu_s}, \tag{4.20}$$

where $Nu_s = \frac{h_s d}{k} = \frac{q_s'' d}{k \Delta T}$. Here, Q is computed by integration over the area of the right wall. The values of ΔT for the steady state and transient cases are 10^oC and 1^oC, respectively. $\overline{Nu}$ indicates the impact of the bubble on the wall to liquid heat transfer. Please note that in the present work, the Prandtl number is kept constant. Also note that Nu_d in equation 4.14 is related to $\overline{Nu}$ by a constant of proportionality.

Table 4.1.
List of parameters corresponding to each numerical case

Case	$\overline{\dot{\gamma}}$	Ar	La	Case	$\overline{\dot{\gamma}}$	Ar	La
1	0.32	250	250	23	1.58	1000	1000
2	0.47	250	250	24	2.21	1000	1000
3	0.63	250	250	25	0.57	1000	250
4	0.95	250	250	26	0.63	1000	250
5	1.58	250	250	27	0.95	1000	250
6	1.90	250	250	28	1.32	1000	250
7	2.21	250	250	29	1.90	1000	250
8	0.63	562	250	30	0.95	250	500
9	0.76	562	250	31	0.95	250	1000
10	0.95	562	250	32	0.95	250	2000
11	1.58	562	250	33	0.95	250	2500
12	1.90	562	250	34	1.60	250	500
13	2.21	562	250	35	1.60	250	1000
14	0.50	562	2000	36	1.60	250	2000
15	0.95	562	2000	37	1.60	250	2500
16	1.56	562	2000	38	0.69	250	250
17	2.21	562	2000	39	0.89	250	250
18	2.84	562	2000	40	1.08	250	250
19	0.50	1000	1000	41	0.47	1000	2000
20	0.63	1000	1000	42	0.79	1000	2000
21	0.95	1000	1000	43	1.42	1000	2000
22	1.26	1000	1000				

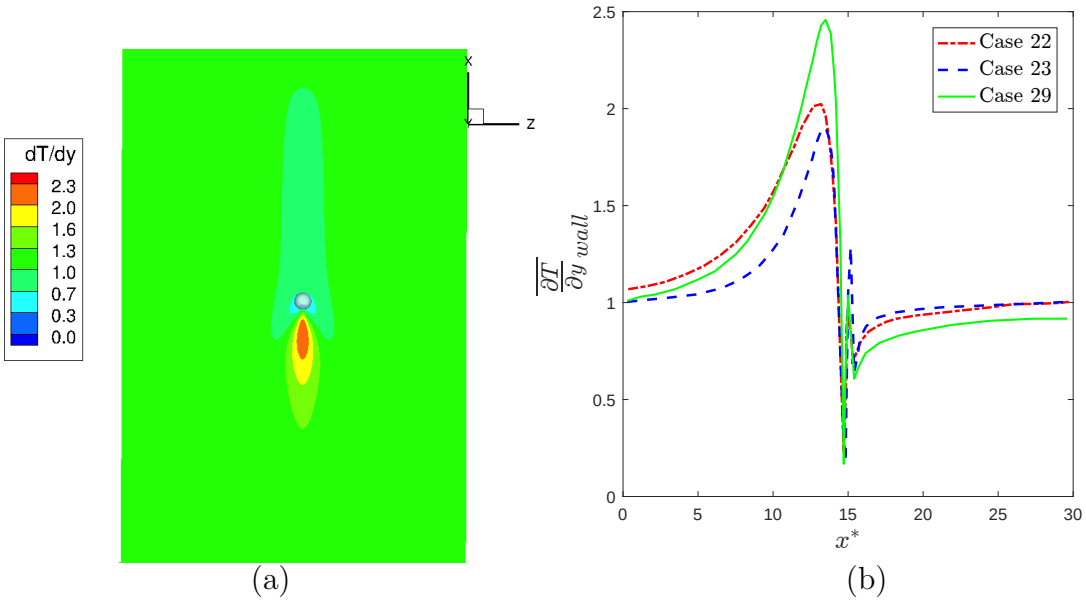

Figure 4.3. (a)Enhancement and reduction of temperature gradient downstream and upstream of bubble for the case $\overline{\dot{\gamma}} = 1.6$ and $La = 2000$ (b) Temperature gradient along the centre line of the $-y$ wall.

4.5 Results and discussion: Steady state

Simulations were performed for five different Laplace numbers and three different Archimedes numbers for dimensionless shear rates in the range of 0.32 to 2.84. All the simulated cases are indicated in Table 4.1. For all the simulations, parameters such as Pr, ρ_l, ρ_g, $C_{p,l}$, and $C_{p,g}$ are kept constant. The dimensions of the domain are: 30 x 10 x 20, and the bubble is located at $(x_b^*, y_b^*, z_b^*) = (15, 0.54, 10)$. The length of the domain is sufficiently large so that the heat flux decays to the single phase value at $x^* = 0$ and $x^* = 30$.

An enhancement of heat transfer downstream of the bubble, and a reduction of heat transfer upstream of the bubble is a characteristic feature observed in all simulations. This can be seen from Figures 4.3(a) and (b). Figure 4.3 (a) shows a view of the bubble rising near the wall at steady state. Figure 4.3 (b) shows a plot of the wall

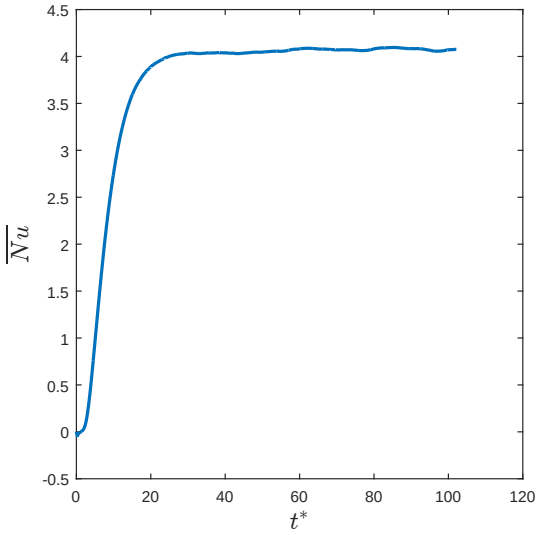

Figure 4.4. The case corresponding to $\bar{\dot{\gamma}} = 2.2$ reached steady state at $t^* = 20$

temperature gradient along the center line of the $-y$ wall passing right underneath the bubble for three cases corresponding to rows 22, 23, and 29 in Table 4.1. We can see that in the upstream region $x^* \geq 15$, heat transfer is reduced, and in the downstream region $x^* \leq 15$ the heat transfer is enhanced.

Another characteristic feature of all the simulations is the abrupt reduction of heat transfer right underneath the bubble. The maximum value of heat flux is $2.0 - 2.5$ times that of single phase flow, and the minimum value is 20% of single phase phase flow, as is evident from Figure 4.3. All the simulations were given sufficient time to reach steady state before the values of $\overline{Nu}$ were recorded. An example of the evolution of $\overline{Nu}$ with time is shown by Figure 4.4. The larger the shear rate and the larger the Laplace number, the longer the bubble takes to reach steady state. For the case shown in Figure 4.4, the heat transfer characteristics around the bubble reach a steady state when the bubble covers approximated 20 bubble diameters along the flow direction in a stationary frame of reference.

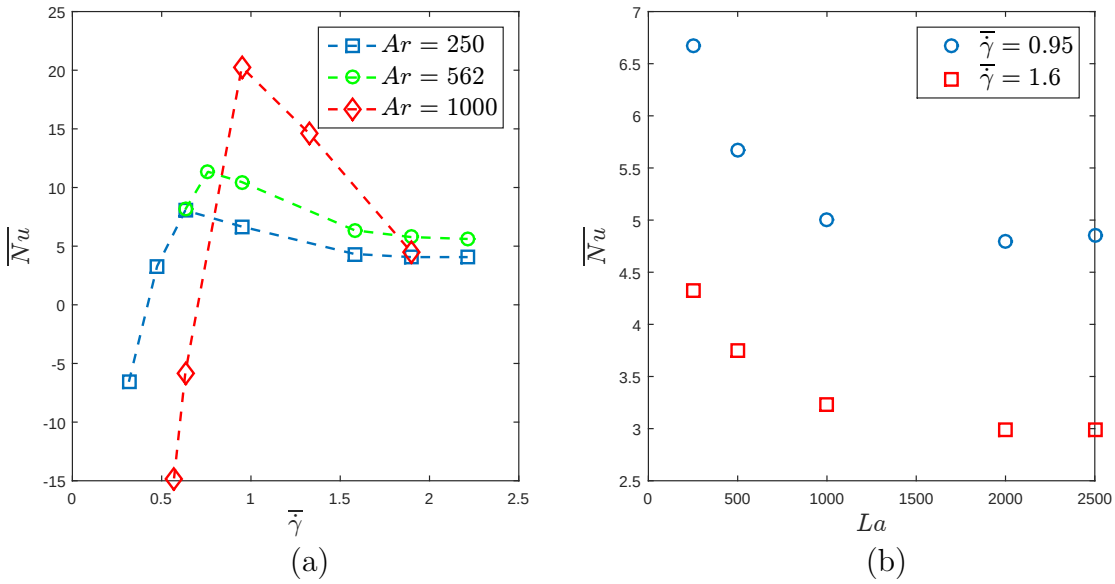

Figure 4.5. (a) $\overline{Nu}$ increases, attains a maximum and decreases as $\overline{\dot{\gamma}}$ increases, (b) Optimum $\overline{\dot{\gamma}}$ shifts with Ar

4.5.1 Variation of $\overline{Nu}$ with $\overline{\dot{\gamma}}$, Ar and La

Ar and La signify the buoyancy and deformability effects, respectively. Numerical studies performed on turbulent bubbly flow in a channel by Dabiri *et al.* [45] show that the distance of the bubbles in the viscous sub-layer from the wall is a function of $E_o = \frac{Ar}{La}$. Bubbles that are weakly deformable tend to hug the wall and those that are deformable tend to move away from the wall. Thus, Ar, La and $\overline{\dot{\gamma}}$ would determine the steady state velocity and the proximity of the bubble with the wall which would in turn determine the heat transfer enhancement at the wall.

We examine how each of the mentioned dimensionless groups affects the heat transfer by running a set of simulations keeping the other groups constant. Cases $1-7$, $8-13$, $14-18$, $19-24$, $25-29$ in Table 4.1 are of fixed combinations of Archimedes and Laplace numbers. Figure 4.5(a) shows the variation of $\overline{Nu}$ with $\overline{\dot{\gamma}}$ for the cases of (Ar, La) : $(250, 250)$, $(562, 250)$, and $(1000, 250)$.

For all the three values of Archimedes numbers shown in Figure 4.5(a), the trend observed is that $\overline{Nu}$ first increases, attains a local maximum and then decreases as $\overline{\dot{\gamma}}$ is increased. It is also to be noted that the increase in $\overline{Nu}$ is steeper than the descent. We observe that the peak $\overline{Nu}$ increases in magnitude as the Archimedes number is increased. The optimum shear rate is found to increase as the Archimedes number is increased. Another important observation from Figure 4.5(a) is that for shear rates below a certain value of $\overline{\dot{\gamma}}$, $\overline{Nu}$ is negative. As evident from Figure 4.3(a) and (b), there is a reduction of heat transfer upstream and an enhancement of heat transfer downstream of the bubble. The net heat transfer enhancement is the sum of the upstream and the downstream effects. Hence, the trend observed in Figure 4.5(a) indicates that for shear rates below a critical value, the upstream effect dominates the downstream effect. Figure 4.5(b) shows the data points for cases $30 - 33$ and $34 - 37$, which correspond to different Laplace numbers for a fixed shear rate and Archimedes number. We observe that $\overline{Nu}$ initially decreases and finally plateaus as the Laplace number is increased for both the shears. For a fixed Archimedes number, as Laplace number increases the bubble deformability decreases. We know from past studies that more deformable bubbles tend to settle farther away from the wall than the less deformable ones. Varying the Laplace number could affect the heat transfer at the wall in the following two ways: Firstly, by affecting how far the bubble is from the wall and thereby affecting how strongly the effect of the bubble is felt on the wall; Secondly, by affecting the steady-state velocity of the bubble, thereby affecting the flow pattern around the bubble. The observed trend can be attributed to a combination of the factors mentioned.

In order to examine the role of the flow pattern around the bubble in the wall heat transfer, and to explain the results observed in Figures 4.5(a) and (b), we define a parameter $\overline{V}$ such that:

$$\overline{V} = \int \int_P \bar{v} dA, \tag{4.21}$$

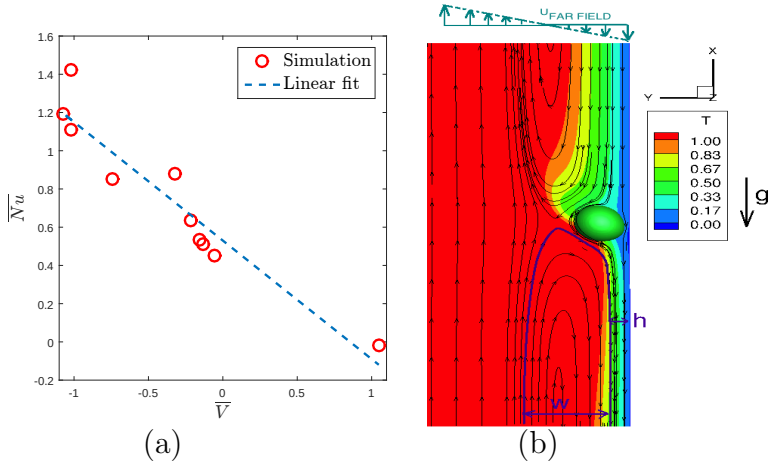

Figure 4.6. (a) Dependence of $\overline{Nu}$ on $\overline{V}$ suggesting the importance of the flow patten behind the bubble (b) Flow pattern around a bubble showing reversal height h_r and reversal width w.

where,

$$\bar{v} = \frac{v}{\dot{\gamma} d}. \tag{4.22}$$

P is a plane with a unit normal in the x direction, behind the bubble. $\overline{V}$ is the area integral of the normalized v velocity field over the plane P. A positive value of $\overline{V}$ implies that the average v velocity behind the bubble is towards the right wall. Figure 4.6(a), indicates a strong dependence of $\overline{Nu}$ on $\overline{V}$. We can see that the more negative the average v velocity behind the bubble, the better the local Nusselt number improvement. This suggests a strong correlation between the flow pattern around the bubble and the heat transfer improvement.

4.5.2 Flow visualization around a bubble in a shear layer

In a plane shear flow without any obstacle, one would see two sets of streamlines in opposite directions separated by a stagnation plane where the velocity changes sign.

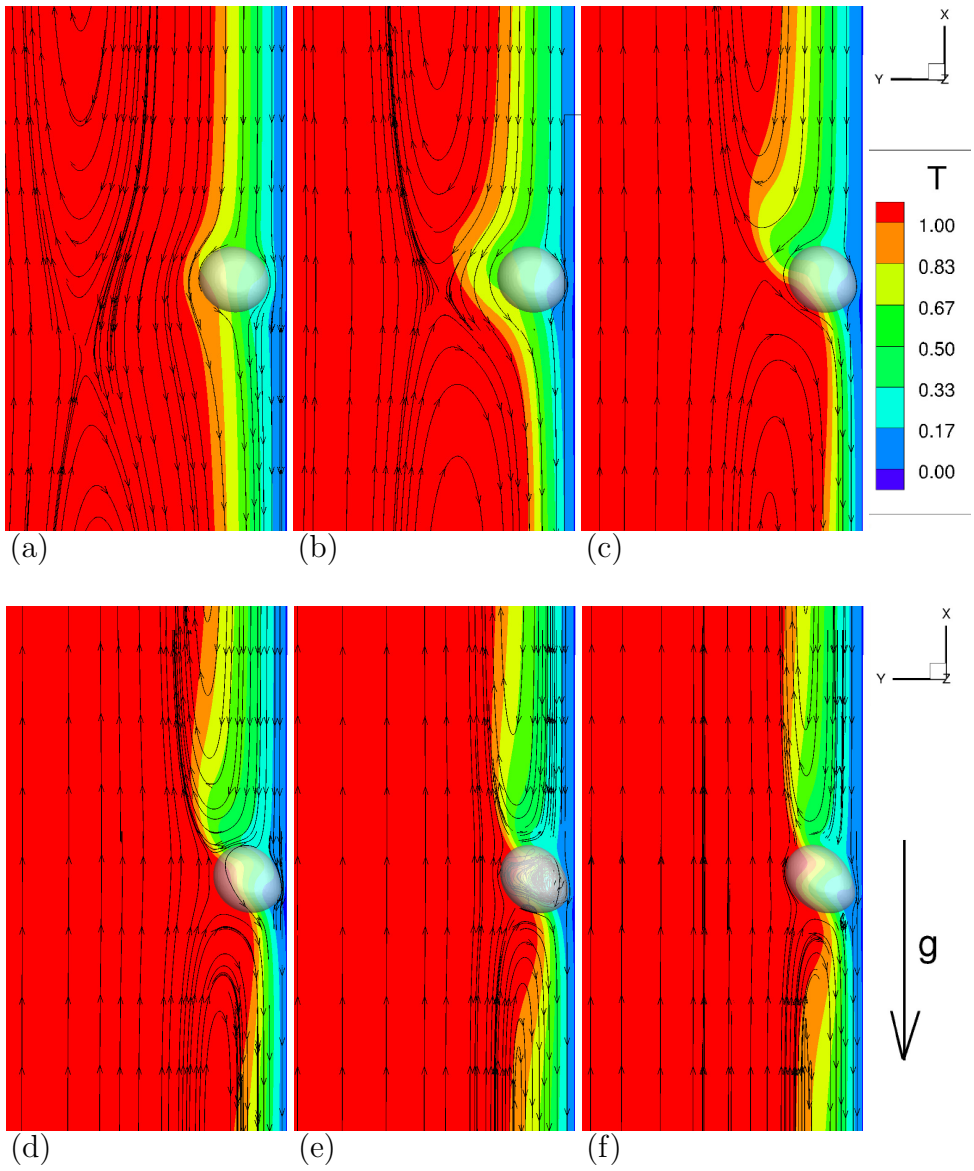

Figure 4.7. Streamlines around the bubble in moving frame of reference and temperature contour plots for $\overline{\dot{\gamma}}$ = (a)0.32, (b)0.47, (c)0.63, (d)0.95, (e)1.6, (f)2.2

However, when there is an obstacle in the shear flow, the streamlines are modified. There are some prior studies on the flow pattern around a cylinder in a shear flow [40,41]. Mikulencak *et al.* [40] found that in the case of an elliptical cylinder in a shear

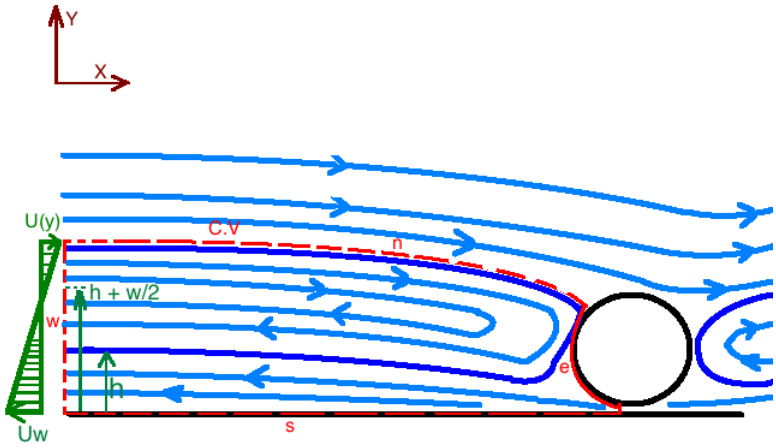

Figure 4.8. Control volume analysis of a simplified $2D$ problem

flow with a non-zero angle of attack, there exist regions with flow reversal. Kossack *et al.* [41] found that for freely rotating cylinders in a shear flow with moderate Reynolds numbers, there are symmetric wakes on both sides of the cylinders. From the analytical solution of an inviscid shear flow over a cylinder, they found that there is a region with closed streamlines. Figure 4.6(b) shows a snapshot of our simulation at steady state. Shown in Figure 4.6(b) is a slice passing through the bubble showing the temperature contour and streamlines around the bubble. Consistent with the cited studies, we observe two sets of closed streamlines near the bubble. Note that the cited studies observed closed streamlines for a $2D$ flow around a cylinder and we observe a similar pattern for $3D$ flows. The flow reversal is a characteristic feature of shear flow around the bubble for all shear rates. Let us call the last stream line to reverse its direction as the reversal streamline. The reversal streamline is shown in purple color in Figure 4.6(b). As we move from the right wall towards the left wall, at some distance, the u velocity changes sign. At $x \to \pm\infty$, this region of zero u velocity represents a stagnation plane parallel to the right wall. At steady state, the right and left walls move at different speeds with respect to the bubble, since the bubble itself has a non-zero rise velocity with respect to the laboratory frame of reference. The

distance of the stagnation plane from the right wall is hence a function of the shear rate and the steady state bubble rise velocity. In order to examine how the reversal streamlines downstream and upstream of the bubble, shown in purple color in Figure 4.6(b), affect the heat transfer, we define the following parameters:

a) w the reversal width, which is the distance along y direction between the incoming and outgoing streams of the reversal streamline.

b) h_r the reversal height, which is the distance of the reversed streamline shown in purple color, from the right wall.

c) The stagnation point, which is the point between the upstream and downstream reversal streamlines where the u velocity is zero with respect to the bubble.

In order to understand the trends observed, we consider the streamlines around the bubble. Shown in Figure 4.7 $(a) - (f)$ are pictures of streamlines around the bubble as seen from the bubble's frame of reference. The contour plot shows the temperature profile. The important observations from Figure 4.7 are the following: Firstly, we see that the thermal layer downstream of the bubble is thinner than that upstream. A thinner thermal layer means greater temperature gradients near the wall resulting in better heat transfer coefficients. Secondly, we observe that as the shear is increased, the reversal height h_r decreases. This is due to the variation of u_b, the steady state bubble rise velocity, with $\bar{\dot{\gamma}}$. We also observe that as the shear rate is increased, the stagnation point gets closer to the bubble. At a certain value of shear rate the stagnation point touches the top of the bubble. If the shear is increased beyond this value, w can only decrease since the reversal streamline is confined by the wall on the right side.

Let us consider a $2D$ version of the problem to gain a physical understanding of the problem and derive a simple analytical description of heat transfer enhancement. We turn our attention to the downstream reversal streamline, to model the heat transfer enhancement downstream of the bubble. We define a control volume as illustrated in Figure 4.8, by the red dashed boundary. It encloses the region between the top of the reversal streamline, the part of the bubble interface in contact with the reversal

streamline, the thin film between the bubble and wall, and the wall. The north, east, west and south faces of the control volume are labeled n, e, w and s, respectively. We make the following assumptions in order to simplify the analysis:

a) The temperature gradient along y direction on the n face of the control volume is almost equal to 1.

b) The enthalpy flux entering the control volume from underneath the bubble is negligible compared to that entering/leaving the control volume from the w face of the control volume. Assuming zero shear condition at the bubble interface, an estimate of the upper bound of this flux is given by:

$$F_e = \rho C_p \delta^2 U_w \left(\frac{\partial T}{\partial y}\right)_e, \tag{4.23}$$

where δ is the thickness of the thin film between the bubble and the wall, and $\left(\frac{\partial T}{\partial y}\right)_e$ is the temperature gradient right below the bubble. δ is usually an order of magnitude less than d, $\left(\frac{\partial T}{\partial y}\right)_e$ is normally less than 1, and U_w is the wall velocity.

c) The thermal conductivity of the gas phase is low. For an air-water mixture, the thermal conductivity of the gas is an order of magnitude less than that of liquid. This assumption would result in a negligible heat transfer from the bubble into the control volume. If the w face of the control volume is far away from the bubble, we can assume that the velocity variation is linear along the y direction at the w face. It can be shown from equation 4.7, that as $x \to \pm\infty$, and the flow becomes fully developed, at steady state, $\frac{\partial^2 T}{\partial y^2} \to 0$, and we have a linear temperature profile. Therefore, we have the following equations at the w face of the control volume:

$$u(y) = \dot{\gamma}.\left(y - h_r - \frac{w}{2}\right) \tag{4.24}$$

$$T(y) = y. \tag{4.25}$$

Now, we perform a thermal energy balance on the control volume:

$$Q_D = F_w. \tag{4.26}$$

Here, Q_D is the excess heat leaving the system from the bottom wall compared to a single phase flow. F_w is the enthalpy flux entering the control volume through the w face.

$$Q_D = \rho C_p \int_0^{h_r+w} \dot{\gamma} \left(y - h_r - \frac{w}{2} \right) y dy \tag{4.27}$$

$$= \rho C_p \dot{\gamma} \left[\left(\frac{w/2 - h_r}{6} \right) (h_r + w)^2 \right]. \tag{4.28}$$

A comparison between the enthalpy fluxes in Equations 4.28 and 4.23 indicates that for cases where the reversal height is small, assumption (b) holds. This is typically the case when the flow reversal occurs close to the wall. Let us define two new quantities W and H:

$$W = \left(\frac{w/2 - h_r}{6} \right), \tag{4.29}$$

$$H = (h_r + w). \tag{4.30}$$

W is the difference between the half width of the reversal stream and the reversal height. H is the height of the reversal streamline. From the control volume analysis, we have:

$$Q_D = \rho C_p \dot{\gamma} \left(\frac{W}{6} \right) (H)^2. \tag{4.31}$$

We compute the downstream excess heat transfer (ΔQ_D) from our $3D$ simulations and record the values of W and H as seen on a slice through the center of the bubble. ΔQ_D is defined as the area integral of wall normal temperature gradient downstream of the bubble. In order to verify the control volume analysis, we perform a least square error for $Q_D \propto \dot{\gamma}^a W^b H^c$, for the $3D$ simulations. Note that the control volume analysis was performed for a $2D$ flow, while the simulation result is a $3D$ one. If the heat transfer enhancement is mainly observed on a thin strip behind the bubble and if the reversal streamlines do not change significantly in height and width along the span-wise direction in the vicinity of the bubble, we can expect the $3D$ data to follow the $2D$ analysis. Figures 4.9 shows a comparison between ΔQ_D from

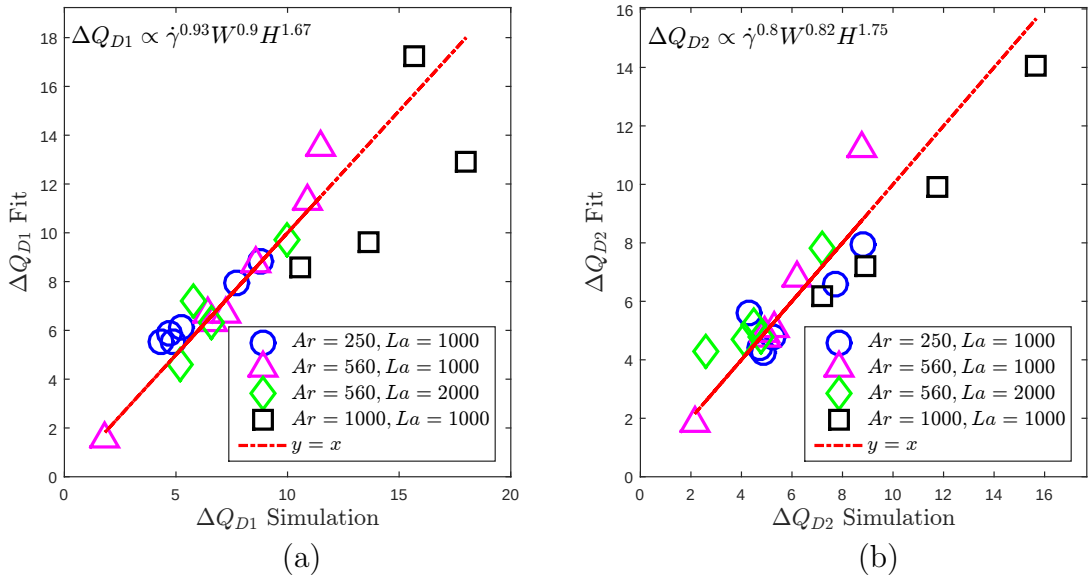

Figure 4.9. A power law fit shows good agreement with the control volume analysis for: (a)ΔQ_{D1} computed over the entire downstream area, and (b)ΔQ_{D2} computed over a thin strip of thickness $3d$ behind the bubble.

simulation and a least square fit. In Figure 4.9 (a) ΔQ_{D1} is computed over the entire downstream wall area, while in Figure 4.9 (b)ΔQ_{D2} is computed over a thin strip downstream that is three bubble diameters in thickness. In the case of $Ar = 1000$, the heat transfer enhancement is well spread out along the span wise direction, unlike in the case of lower Archimedes numbers. This violates the condition for agreement with the $2D$ control volume analysis discussed earlier, causing the data points to deviate from the 45^o line as seen in Figure 4.9 (a). Figure 4.9 (b), however, shows that if ΔQ_{D2} is computed for a thin strip downstream of the bubble that is three bubble diameters in width, there is much less deviation from the 45^o line compared to Figure 4.9 (a). For ΔQ_{D1} computed over the entire downstream area, we have $\Delta Q_{D1,Fit} \propto \dot{\gamma}^{0.93} W^{0.9} H^{1.67}$. For ΔQ_{D2} computed over a thin strip downstream of the bubble, we have $\Delta Q_{D2,Fit} \propto \dot{\gamma}^{0.8} W^{0.82} H^{1.75}$. The exponents of $\dot{\gamma}, W$ and H are close to $1, 1$ and 2 as predicted by the control volume analysis. The deviation of

these exponents from the predicted values is due to the simplifications used to derive the analytical formulation. Nonetheless, the analysis provides us with a qualitative understanding of the impact of the reversal streamlines around the bubble on the enhanced heat transfer. It is important to note that W and H are functions of the shear rate, the Laplace number and the Archimedes number respectively. A similar analysis could be performed on the upstream reversal streamline to find the heat transfer reduction, but assumption (a) is no longer valid in that case. The net improvement in heat transfer is a result of the downstream improvement in heat transfer eclipsing the upstream effect of heat transfer diminishment.

4.5.3 Inviscid shear flow and the effect of the thin film

Prior studies [40, 41] show that the analytical solution of inviscid shear flow gives us a good approximation of the flow pattern around cylindrical objects in a shear flow. The assumption in such a flow is that it has a uniform vorticity ω_0 in the far field region. For $2D$ inviscid shear flows, since the vortex stretching term is 0 in the vorticity transport equation, the stated assumptions yield that vorticity is preserved everywhere as shown in equation 4.33. Inviscid shear flows around a circular and an elliptical cylinder were solved analytically by Milne-Thomson [43]. However, we need the solution to inviscid shear flow around a cylinder fixed near a wall in order to make any valid comparisons with our problem. Dériat analytically solved the inviscid shear flow around a cylinder near a stationary wall [44]. In our case, the wall has a tangential velocity with respect to the bubble and hence we make some changes to the result derived by Dériat. For a $2D$ inviscid shear flow of shear rate $\dot{\gamma}$ around a cylinder of radius a held at a fixed distance b from a wall, the equations we seek to solve are as follows:

$$\frac{D\omega}{Dt} = \nu\Delta\omega = 0, \tag{4.32}$$

$$\Rightarrow \omega(x, y, t) = \omega_0 = 2\dot{\gamma}, \tag{4.33}$$

$$\Delta\psi = 2\dot{\gamma}. \tag{4.34}$$

The boundary conditions to this equation are:

$$|x| \to \infty : u = \dot{\gamma}y, v = 0, \tag{4.35}$$

and the stream function is a constant on the cylinder and the wall.
If we use the Argand plane to represent points in the $2D$ cartesian space, the above boundary conditions can be expressed as:

$$|Re(z)| \to \infty : \psi = -\frac{\dot{\gamma}(z-\overline{z})^2}{8}, \tag{4.36}$$

$$|z - bi| = a : \psi = C_1, \tag{4.37}$$

$$Im(z) = 0 : \psi = C_2. \tag{4.38}$$

By omitting the circulation terms in the solution of Dériat and adding some terms to impose a velocity u_{wall} on the wall, we arrive at the following expression for the stream function:

$$\begin{aligned}\psi = -\frac{\dot{\gamma}}{8}\Bigg((z-\overline{z})^2 + 2a^4\Bigg[&Re\left(-\frac{1}{(z-ib)^2} + \frac{1}{(z+ib)^2}\right)\\ &+\sum_{n\geq 1}\frac{1}{(b+b_n)^2}Re\left(\frac{(z-ib_n)^2}{(z-ib_{n+1})^2} - \frac{(z+ib_n)^2}{(z+ib_{n+1})^2}\right)\Bigg]\\ &-8ba^2\left[Im\left(\frac{1}{z-ib} + \frac{1}{z+ib}\right) + \sum_{n\geq 1}\frac{1}{b+b_n}Re\left(\frac{z-ib_n}{z-ib_{n+1}} - \frac{z+ib_n}{z+ib_{n+1}}\right)\right]\Bigg)\\ &-\frac{u_{wall}(z-\overline{z})}{2i} - u_{wall}a^2\left[Im\left(\frac{1}{z-ib} + \frac{1}{z+ib}\right) + \right.\\ &\left.\sum_{n\geq 1}\frac{1}{b+b_n}Re\left(\frac{z-ib_n}{z-ib_{n+1}} - \frac{z+ib_n}{z+ib_{n+1}}\right)\right],\end{aligned} \tag{4.39}$$

where b_n is given by the recursive relation:

$$b_{n+1} = b - \frac{a^2}{b+b_n}, b_1 = b. \tag{4.40}$$

In our computations of ψ, we sum up each of the series in the above equations up to 30 terms as doing so yields a convergence up to the fifth decimal place. The detailed derivation of the above equations can be found in [43, 44].

Consider a $2D$ version of the problem of interest: a cylindrical bubble rising in a shear flow between two walls with opposite velocities. Solving this problem numerically results in a thin film region between the bubble and the wall, similar to what was observed in the $3D$ cases. In the case of an inviscid shear flow around a cylinder, the no-slip boundary condition is not guaranteed everywhere along the wall. In fact in the inviscid shear flow, the vorticity is preserved everywhere including the thin film between the bubble and the wall, whereas in the case with non-zero viscosity the shear rate in the film is known to be significantly higher than the far field shear rate. Therefore, while the inviscid shear flow over a cylinder might capture the physics of viscous flow over a bubble for some Reynolds numbers, one can be sure that the physics in the thin film region would not be accurately captured. A comparison between the results of the inviscid flow solution coupled with the energy equation and the $2D$ simulation would shed some light on the relative importance of the thin film heat transfer.

This is done by the following method:

1) Compute the heat transfer around a $2D$ bubble in the bubble's frame of reference.

2) At an instant when the bubble is close to the wall, record the bubble's distance from the wall and the distance of the top most point of the bubble from the wall.

3) Record the velocity of the wall with respect to the bubble, and the heat flux distribution along the wall.

Now, move to the inviscid shear flow and:

1) Manipulate the values of a and b such that the top most point on the cylinder is at the same distance from the wall as the top most point of the bubble, and the reversal height and width match those from the simulation. This is necessary since

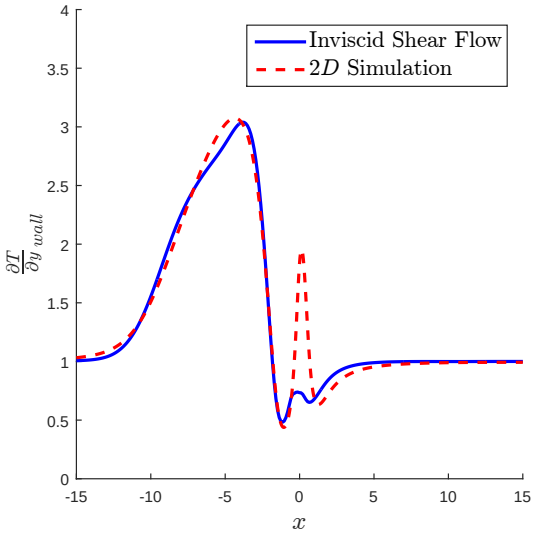

Figure 4.10. Comparison between the inviscid shear flow solution and $2D$ simulation for $\dot{\gamma} = 0.2$ showing a good match for downstream heat transfer, and highlighting the contribution of the thin film.

the bubble in the $2D$ simulation is deformable and hence gets stretched whereas in the inviscid flow solution we assume a perfectly circular cylinder.

2) Plug the value of wall velocity recorded from the simulation into equation 4.39 and solve for the u and v velocity components using the stream function ψ.

3) Use the velocity field to numerically solve the temperature equation. For simplicity, neglect the $\frac{\partial T}{\partial t}$ term and only spatially integrate with the appropriate boundary conditions.

A comparison between wall normal temperature gradient along the x axis for the inviscid shear flow solution and the $2D$ simulation would serve to verify the method used for simulation and also highlight the contribution of the film between the bubble and the wall. Figure 4.10 shows the wall normal temperature gradients for both cases with the bubble position being $x = 0$. We observe that the downstream temperature

gradients compare well for both cases. There is however a peak in the temperature gradient in the thin film region captured by the $2D$ simulation. We also see that the downstream heat transfer enhancement caused by the reversal streamline is the dominant factor.

4.6 Transient heat transfer

The cases examined thus far have been confined to the impact of the bubble on steady state heat transfer. However, in many practical applications, the background single phase heat transfer is transient in nature. In order to examine the effect of bubble dynamics in shear flow on the transient heat transfer from a wall, we make the following modifications to the previous problem: The fluid is initially at a uniform bulk temperature $T^* = 0$, the wall is maintained at a temperature $T_R^* = 1$. For a single phase problem with the same boundary and initial conditions, the analytical solution is given by Equations 4.2 and 4.3. Equation 4.3 gives us a benchmark to evaluate the enhanced heat transfer due to the bubble. In order to examine the effect of $\overline{\dot{\gamma}}$, we simulate three cases of dimensionless shear rate: $\overline{\dot{\gamma}} = 0.7$, 0.9 and 1.1 corresponding to rows 38, 39 and 40, respectively in Table 4.1.

We use the same parameters as used in the steady case to quantify the improvement in heat transfer for the transient simulations. Shown in Figure 4.11(a) is a snapshot of the simulation at $t^* = 638$ for a shear rate $\overline{\dot{\gamma}} = 0.5$. $\overline{Nu}$ is defined according to section 4.4. Figure 4.11(b) shows that $\overline{Nu}$ reaches an asymptotic value after a certain time for $\overline{\dot{\gamma}} = 0.7$, 0.9 and 1.1. It is interesting to note that although the wall heat transfer is transient in nature, its enhancement due to the bubble reaches a steady state. In order to explain the observed trend, we consider equation 4.3. The two relevant length scales to this problem are: the thermal layer thickness $\delta_T = \sqrt{\pi \alpha t}$, and the augmented reversal height H defined in equation 4.30. While the former increases with time, the latter reaches a steady state. Therefore, at a certain time when the δ_T is significantly larger than H, the system resembles a case of the linear temperature

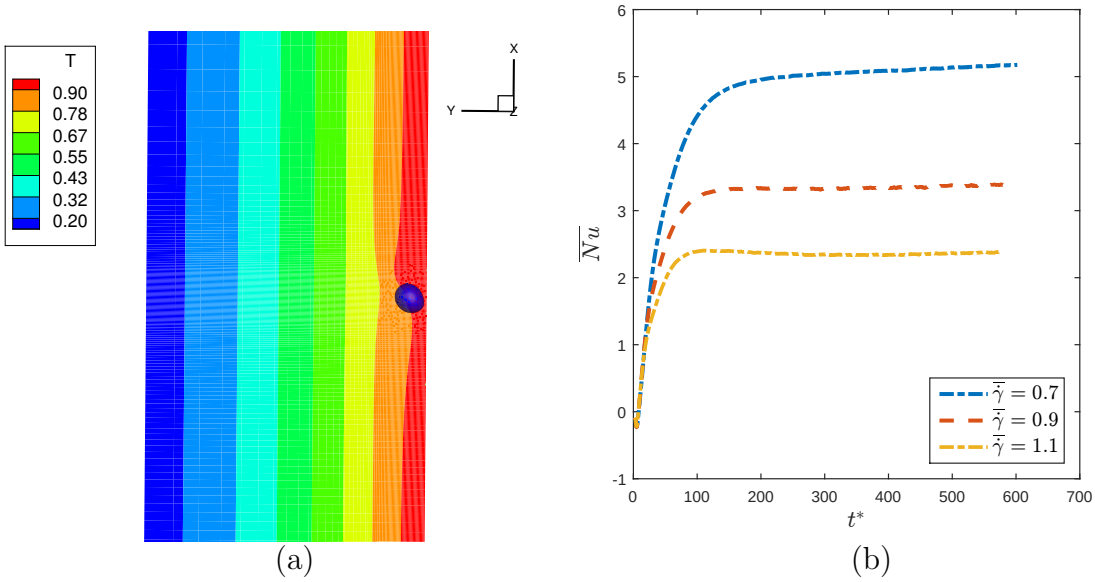

Figure 4.11. (a)Snapshot of the simulation at $t^* = 638$ for transient heat transfer (b)$\overline{Nu}$ reaches asymptotic values for $\bar{\dot{\gamma}}$=0.7,0.9 and 1.1 respectively.

profile problem discussed earlier, but with a time dependent temperature gradient $\frac{\partial T}{\partial y} = -\frac{1}{\delta_T(t)}$. Hence, we see that the fractional enhancement in heat transfer, which is independent of the heat flux at the wall, is purely a function of the flow parameters at steady state.

4.7 A rising layer of bubbles

In practical applications of two-phase heat transfer we often have an array of bubbles moving near the heated surface with a certain void fraction. In many situations the rise of the bubbles itself or other flow conditions, such as a driving pressure gradient, creates a flow parallel to the wall near which the bubbles are rising. In the present section we consider a layer of bubbles rising near a vertical wall and the heat transfer associated with such a flow. To examine the heat transfer characteristics of such

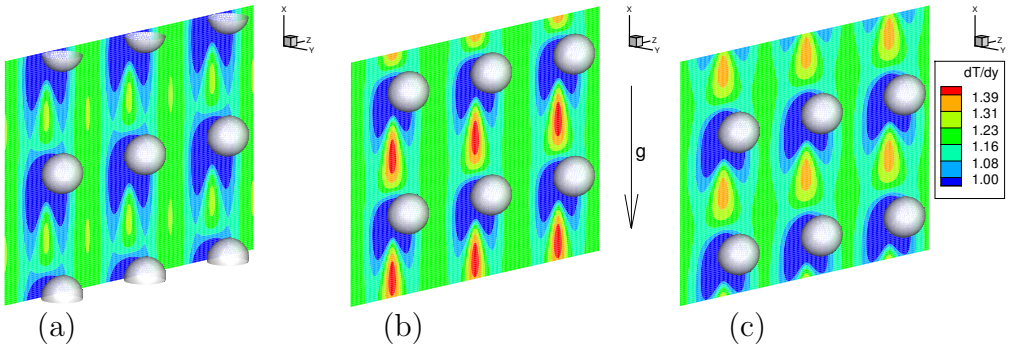

Figure 4.12. Contours of heat flux at the wall with an array of bubbles flowing upwards at (a) $\overline{\dot{\gamma}} = 0.47$, (b) $\overline{\dot{\gamma}} = 0.79$, and (c) $\overline{\dot{\gamma}} = 1.42$ respectively.

a flow, we solve Equation 4.7 along with the momentum equations. The boundary conditions for temperature are as follows:

$$T(y^* = 0) = 0, \tag{4.41}$$

$$T(y^* = L_y^*) = 1. \tag{4.42}$$

Periodic boundary conditions are applied to T along X and Z directions:

$$T(z^* = 0) = T(z^* = L_z^*), \tag{4.43}$$

$$T(x^* = 0) = T(x^* = L_x^*). \tag{4.44}$$

In the present work, we use a void fraction of 0.06 which corresponds to a dimensionless X and Z length of $L_x^* = L_z^* = 3.0$. The temperature and velocity boundary conditions at the $+Y$ and $-Y$ are the same as discussed in section 4.2.

We consider three different dimensionless shear rates corresponding to cases 41, 42, and 43 respectively in Table 5.4. Figure 4.12 (a), (b), and (c) show the contour of the dimensionless temperature gradient at the wall for the cases of dimensionless shear rates 0.47, 0.79, and 1.42, respectively. It is to be noted that Figure 4.12(a), (b), and (c) were each created by stacking together several images of the computational domain

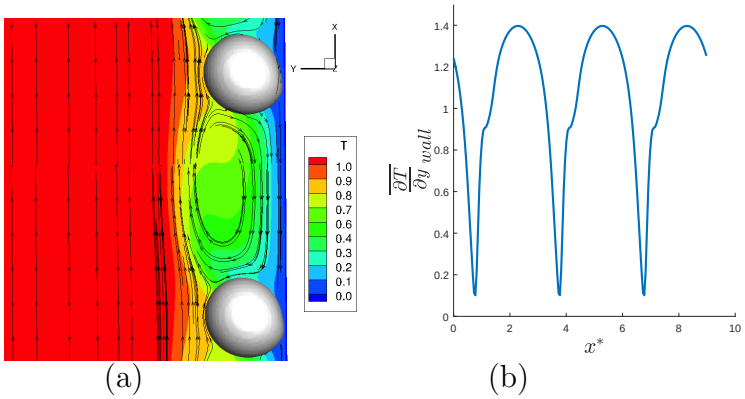

Figure 4.13. (a)Snapshot of the simulation of case 42 corresponding to $\overline{\dot{\gamma}} = 0.79$ showing a recirculation zone between two bubbles. (b) A Periodic variation of temperature gradient along the centre line of the $-y$ wall.

which contained a single bubble with the periodic boundary condition along X and Z directions. The fractional improvement in Nusselt number for these cases are 0.697, 1.17, and 0.83 respectively. Figure 4.13(a) shows a recirculation zone between two bubbles among the array of bubbles. The streamlines are drawn from the bubbles' frame of reference. The heat transfer characteristics in the recirculation zone can be seen as a combination of the diminishment in heat transfer caused upstream of the lower bubble and the enhancement in heat transfer caused downstream of the upper bubble. Figure 4.13(b) shows a periodic variation of the dimensionless wall normal temperature gradient along the centerline of the computational domain. The regions of steep heat transfer diminishment represent locations of the bubbles.

It is to be noted that although the results discussed in the present section are based on simulations with single bubble in the computational domain along with periodic boundary conditions, a configuration such as shown in Figure 4.12 is not stable and would require us to consider a larger computational domain with many bubbles.

4.8 Summary

The impact of a single bubble rising in a shear flow on the wall to liquid heat transfer has been quantified. $\overline{Nu}$ was found to show a non-monotonous variation with the shear rate. An optimum shear rate corresponding to the maximum heat transfer enhancement was observed for all Archimedes numbers. The heat transfer enhancement was found to chiefly be influenced by the downstream flow reversal structures characterized by the reversal height and reversal width. A $2D$ control volume analysis showed a good agreement with the $3D$ fully resolved simulation results in terms of the effect of reversal height and width on the heat transfer enhancement. A $2D$ inviscid shear flow around a cylinder was used to model the flow over a $2D$ bubble rising near a wall to describe the underlying physics of enhanced heat transfer. The wall normal temperature gradient from the inviscid shear flow solution was compared with that from a $2D$ Navier stokes simulation to highlight the role played by the thin film between the bubble and the wall in the heat transfer. In the case of transient heat transfer the fractional improvement in heat transfer was seen to reach a constant value after a certain time even though the heat flux decays with time. Both the steady state and transient simulation results suggest a strong dependence of heat transfer enhancement on the flow pattern around the bubble. The results from simulations of an array of bubbles rising near a wall suggest that the heat transfer in the recirculation zones is a combination of the upstream and downstream effects of the bubbles surrounding it.

5. NUMERICAL MODELING OF PHASE CHANGE IN TWO-PHASE FLOWS

For the past decade, there has been a growing interest in computational fluid dynamics as a predictive method for studying boiling related problems. This is partly due the development of effective numerical methods for multi-phase flow simulation, and partly due to empirical and theoretical models being limited in their ability to predict transient fluid flow and heat transfer. While several successful attempts have been made to reproduce experimental results using computational fluid dynamics, there still exist some areas that require more work. In the following section, we cover the relevant literature in the area of numerical methods for boiling, and the gaps that need to be filled.

5.1 Literature review

The most challenging part of two-phase flow simulation is interface tracking with minimal volume loss in the bubble. The following are some of the most popular methods that have been used in literature to simulate boiling problems:

5.1.1 Level-set method

The level-set method was pioneered by Sussman *et al.* [66]. It involves solving the time evolutionof ϕ, the distance function, which is defined at any point as the shortest distance of the point from the gas-liquid interface. In a two-phase simulation the distance function would have a positive value in one phase and a negative value in anther. The zero level-set of the distance function marks the interface. This function is advected using the Eulerian velocity field as follows:

$$\frac{\partial \phi}{\partial t} + \overline{u}.\nabla(\phi) = 0 \tag{5.1}$$

For ϕ to remain the distance function, it has to be reinitialized at a certain interval of time. The reinitialization is commonly achieved by using the method described in [66]. Son *et al.* [67] was the first to fully simulate nucleate pool boiling of water using the level-set method. They solved the axisymmetric Navier Stokes equations in $2D$ with a special treatment given to the micro-region beneath the bubble containing the thin film. They solved a fourth-order ODE iteratively along with the macro-region solution to match the solutions where the two regions meet. Their simulations compare very well with pictures captured during experiments. Singh *et al.* [68] studied the effect of sub-cooling and gravity on nucleate pool boiling.

Abarajith *et al.* [69] used the level-set method to study the effect of contact angle on the departure characteristics of a single bubble in nucleate pool boiling. Son *et al.* [70] used the same method to study the phenomenon of merger a departed bubble with the subsequent bubble and its effect on heat transfer characteristics and departure characteristics of the bubble. Li *et al.* [71] studied the effect of background flow on departure characteristics of bubbles in horizontal and vertical flow situations. They used a wall superheat of $5.3K$ and a flow velocity of $0.076\ m/s$. They specified a contact angle at the wall for the said simulations. Aktinol and Dhir [72] studied nucleate boiling coupled with the thermal response of the wall unlike the previous studies by Dhir's group where they used a constant wall temperature.

Mukherjee and Kandlikar [73] used the Level-set method to simulate the growth of a water bubble into a slug bubble. They conducted an experiment of flow boiling in a microchannel of hydraulic diameter $0.2\ mm$ with a wall superheat of $2K$. Their numerical simulation shows a good comparison with the experiment in terms of the equivalent bubble diameter as a function of time. Mukherjee and Kandlikar [75] also studied the effect of restrictions at the inlet of the channel on the bubble growth rate. They found from simulations consistent with experiments that the bubble growth rate decreases as the inlet is restricted. Mukherjee *et al.* [76] also studied the wall heat transfer during bubble growth in flow boiling. They found that the surface tension and flow rate have little influence on the wall heat transfer. But the bubble

with the lowest contact angle resulted in the highest heat heat transfer rate. All successful attempts to reproduce experimental results cited above show that Level-set is a powerful tool for Boiling simulations. The chief attraction of Level-set is its ease of implementation. The disadvantage being that if an effective reinitialization algorithm is not employed, a fast moving bubble can lose mass. By definition, the Level-set is not volume-conservative.

5.1.2 VOF (Volume of fluid)

In the Volume of fluid method, color function C is used to track the interface. C represents the volume fraction of a given phase. It is 0 wherever there is one phase, and 1.0 where there is another. At the interface cells C takes a value between 0 and 1.0 representing the volume fraction of the cell. The color function is advected as follows:

$$\frac{\partial C}{\partial t} + \overline{u}.\nabla(C) = 0 \tag{5.2}$$

Volume of Fluid was pioneered by Scardovelli and Zaleski [51]. There are several improvements to the basic Volume of Fluid method have been proposed of which $SLIC$ [52], and $PLIC$ [53] are the popular ones. Sato and Niceno [77] used VOF to build a phase change model to study nucleate boiling. They imposed saturation temperature as a dirichlet boundary condition at the interface by modifying the numerical schemes used to compute diffusion and convection by including the saturation temperature. They used a separate model using boundary layer theory to solve for the thin film beneath the bubble. They successfully compared their numerical results with experiments from different research groups. In an effort to simplify the film model proposed earlier, Sato *et al.* [78] incorporated the findings of Utaka *et al.* [87] to assume that the initial flow profile varies linearly along the radial direction. The constant of proportionality of the linear film profile was found by Utaka *et al.* [87] to be 4.46x10^{-3} for water, and 10.2x10^{-3} for ethanol at atmospheric pressure. Sato *et al.* [78] achieved a good match with experimental findings from various research

groups using their revised film model. Sato *et al.* [90] also studied the transition of vapor bubble regime from discrete bubbles to the vapor mushroom regime.
Magnini, Pulvirenti and Thome [93] used VOF to run $2D$ axisymmetric simulations of elongated slug bubble flow in a microchannel of circular cross-section. They employed a separate film model to solve for the heat transfer in the thin film region. They found the film heat transfer to be the dominant phenomenon of heat transfer. The popular VOF techniques used have the advantage of being robust and volume conservative. The disadvantage of VOF is that moving from $2D$ to $3D$ involves a significant increase in the level of complexity. The studies cited in the present section indicate that it is a reliable and accurate method for boiling problems.

5.1.3 Other methods

Apart from VOF and Level-set methods, there are a few other methods that have been used to carry out successful computations of boiling flows in literature. The front-tracking method was pioneered by Unverdi and Tryggvason [28], and it involves representing the gas-liquid interface as a network of interconnected points called the 'front'. The front is advected by using the eulerian velocity field. Juric and Tryggvason [94] first laid down the procedure to implement phase change using front-tracking. They carried out computations of film boiling in the study. Esmaeeli *et al.* [96, 97], in a two-part paper carried out computations of film boiling using front-tracking. The advantage of using front-tracking is its accuracy when it comes to surface tension computation and it is useful when we are interested in computations of swarms of bubbles. The disadvantage however is that coalescence and break of bubbles will involve changing the topology of the front which can be challenging.
The Lattice-Boltzmann method is attractive due to its ease in being run parallely on multiple cores. Sun *et al.* [98] simulated bubble growth and departure in nucleate pool boiling. They found the dependence of bubble departure diameter and bubble departure frequency on the acceleration due to gravity. Jafari *et al.* [99] used the

Cahn-Hillard phase field method to simulate bubble growth and departure from an artificial cavity in a micro-channel of cross-section $100\mu m$x$100\mu m$. They validated their results with the experimental findings of Lee *et al.* [100].

5.1.4 Gaps in literature

From the literature on numerical modeling of boiling, it is clear that a substantial amount of progress has been in studying Nucleate pool boiling. However, in the case of Flow boiling only moderate success has been achieved, especially in flows situations involving simple geometries. Microchannel heat sinks are susceptible to problems such as hot-spots, pressure fluctuations, and flow reversal between adjacent channels. From the literature reviewed in the present section, it is clear that more research is required to understand and mitigate the problems mentioned above. Kharangate and Mudawar [110] give a comprehensive review on all the progress that has been made in the field of boiling computational fluid dynamics over the past couple of decades. In their review, they mention that the focus of the computational fluid dynamics community needs to shift towards more complex geometries and better mass transfer models than are found in literature. There is also a need to mitigate parasitic currents that result from using a continuum approach to model surface tension.

Most of the existing studies in computational fluid dynamics of flow boiling either use a simplified $2D$ approach, or consider simple cases such as saturated boiling of singular slug bubbles. There is a scaricity of studies that have considered multi-dispersed bubbles undergoing flow boiling under sub-cooled conditions. With this in mind, the aim of the subsequent sections would be to illustrate a robust phase change model that is validated with benchmark problems for phase change.

5.2 Numerical method

We solve the momentum equation and the temperature equation using the finite-volume method. We employ the front tracking method [28] for interface tracking. The

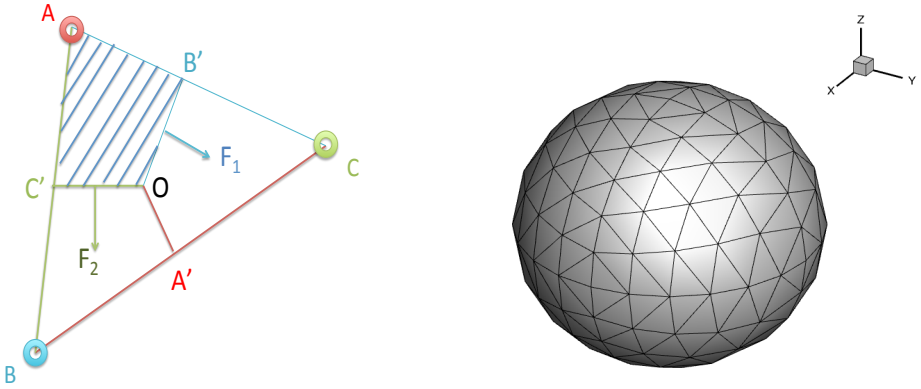

(a) (b)

Figure 5.1. (a)Element connecting 3 points showing the shaded sub-element, and forces acting on point A.(b) Interface represented as a front.

momentum equations are solved using the explicit Euler time advancement scheme, and the energy equation is solved semi-implicitly. Described in the following subsections is a detailed account of the various schemes used in the discretization.

5.2.1 Momentum

We solve the Navier-Stokes equations along the X, Y, and Z directions:

$$\rho\frac{\partial \mathbf{u}}{\partial t} + \rho\nabla\cdot(\mathbf{uu}) = -\nabla p + \nabla\cdot\left\{\mu\left(\nabla\mathbf{u} + (\nabla\mathbf{u})^T\right)\right\} + \rho\mathbf{g} + \int_f \sigma\kappa\mathbf{n}\delta(\mathbf{x}-\mathbf{x}_f)d\mathcal{A}_f + \rho\mathbf{u}(\nabla\cdot\mathbf{u}) \tag{5.3}$$

$$\frac{\mathbf{u}^* - \mathbf{u}^\mathbf{n}}{\Delta t} = -R_c^n + R_\nu^n + \nabla\cdot^n \mathbf{u} + g, \tag{5.4}$$

$$\frac{\mathbf{u}^{n+1} - \mathbf{u}^*}{\Delta t} = \frac{\nabla^{n+1} P}{\rho}. \tag{5.5}$$

Notice that equation 5.3 is different from the conventional momentum equations in that we no longer have a zero divergence of velocity. The non-zero divergence of velocity is due to volume change brought about by the expansion/contaction that

occurs as one phase transforms into the other. The details of how $\nabla \cdot \mathbf{u}$ is computed will be presented in the next subsection. The convective term is discretized using the QUICK upwind scheme [101], and the diffusive term is discretized using a central difference scheme. R_c^n is the discretized convective term and R_ν^n is the discretized diffusive term, computed at the n^{th} time-step. We use the fractional-step method proposed by Chorin [102]. We use the explicit treatment for $\nabla \cdot \mathbf{u}$ in the fractional-step method, although it could also be treated implicitly. The surface tension term in Equation 5.3 is computed using the front tracking method.

In front-tracking, we represent the gas-liquid interface as a network of interconnected points. The front points are interconnected in the form of triangular elements. Figure 5.1 shows a typical element connecting three points A, B, and C. Consider A', B', and C' being the mid-points of the sides of the triangle opposite to points A, B, and C, respectively. Point O being the centroid of the element, consider a sub-element A, B', O, C'. The contribution of surface tension from the element $A - B - C$ to point A is the sum of vectors F_1 and F_2, which are computed based on the lengths line segments $B' - O$ and $O - C'$ respectively as shown in Figure 5.1. Similarly the surface tension force is computed for points B, and C. This is in line with the method proposed by Unverdi and Tryggvason [28].

The surface tension a smoothed from the lagrangian front points onto the Eulerian node points using the Peskin interpolation [105]. The surface tension force per unit volume in Equation 5.3 is computed using the continuum force model [104]. Since the bubbles in the two-phase flow can experience stretching, expansion, and contraction the front elements in a localized region may experience a contraction or stretching in size. To keep the density of the front points relatively uniform we re-grid the front at each time-step. This is done based on the lower or upper limits on the aspect ratio and side lengths of the front elements. Additionally, we will also smooth the front to avoid sharp corners on the front that result from the re-grid mechanism. To gain further insights into the front operations, we direct the reader to Unverdi and Tryggvason [28].

5.2.2 Energy

For temperature, we solve the temperature transport equation 5.6. It is derived from the 1^{st} law of thermodynamics.

$$\rho C\left[\frac{\partial T}{\partial t}+\nabla\cdot(\mathbf{u}T)\right]=\nabla\cdot(K\nabla T)+\rho CT\left(\nabla\cdot u\right). \tag{5.6}$$

The difference between equation 5.6 and the standard incompressible-flow energy equation is the last term. The $\rho CT\left(\nabla\cdot u\right)$ term represents a source term arising due to the expansion of water as it transforms to vapor.

In the present model we make the assumption that the saturation temperature of the liquid is constant, and that the gas-liquid interface is at the saturation temperature. In order to implement this feature, we introduce the saturation temperature of the liquid as a boundary condition at the points where the interface exists. Note that Equation 5.6 does not have a source term containing the latent heat of vaporization of water. This is because we manually impose the saturation temperature as a boundary condition at the gas-liquid interface at each time-step. This is akin to the method used by Sato *et al.* [77]. The implementation of the saturation temperature as a boundary condition is achieved by using the front information as follows:

$$\left(\widehat{\frac{\partial T}{\partial x}}\right)_{ijk,-}=\frac{T_i-T_{sat}}{h_x(i,j,k)} \tag{5.7}$$

$$\left(\widehat{\frac{\partial T}{\partial x}}\right)_{ijk,+}=\frac{T_{sat}-T_i}{h_x(i,j,k)} \tag{5.8}$$

We mark any two nodes that are adjacent to the front as the interfacial nodes. The distance of the front from the interfacial points along X, Y and Z directions are stored as h_x, h_y, and h_z respectively. Figure 5.2(a) shows a $2D$ representation of the idea shown on the $X-Z$ plane. The saturation temperature is implemented as a boundary condition as follows. Consider a node such that the front passes to the left of the node as shown in Figure 5.2(b). If we wish to compute the derivative along the X direction $\left(\frac{\partial T}{\partial x}\right)_-$ we use Equation 5.7. On the other hand, if the interface passes

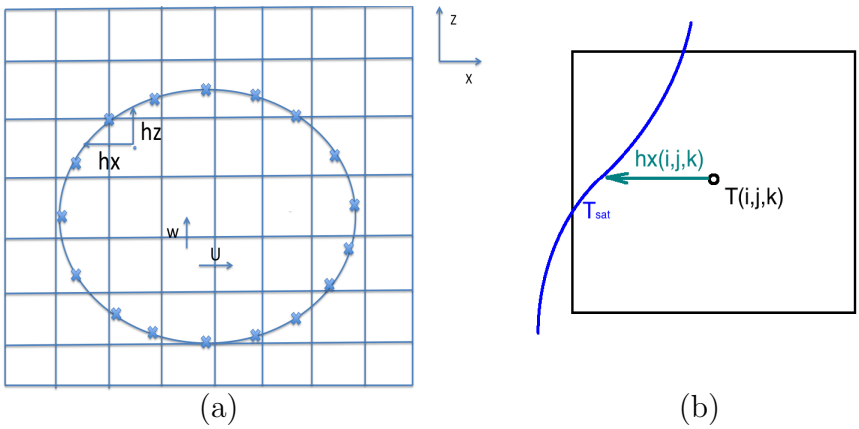

(a) (b)

Figure 5.2. (a) Showing hx and hz. (b) Implementation of the dirichlet boundary condition of T_{sat} at the front.

to the right of the node, and if we wish to compute $\left(\frac{\partial T}{\partial x}\right)_+$, we use equation 5.8. A similar approach is employed to compute the diffusive terms in the energy equation.

5.2.3 Mass transfer

There are several effective Mass transfer models that have been proposed in literature. The flux-deficit model has been used widely by researchers such as Son *et al.* [67], Sato *et al.* [77], and Mukherjee *et al.* [73]. The deficit in the conduction heat flux across the gas-liquid interface is balanced by the latent heat of vaporisation brought about by the mass transfer across the interface. The second method that has been used in literature is the Schrage model [106]. It uses the kinetic theory of gases [108] to predict the mass transfer happening across the interface using a parameter γ which is the fraction of molecules evaporating or condensing. The value of γ used for stagnant liquid problems is less than 0.1. A simplified version of Schrage's model is the Lee model [107], which uses the deviation of interface temperature from T_{sat} to be the driving force for phase change. Empirical coefficient r_i, known as the mass transfer intensity factor. In the present study, we use the simple flux-deficit model to im-

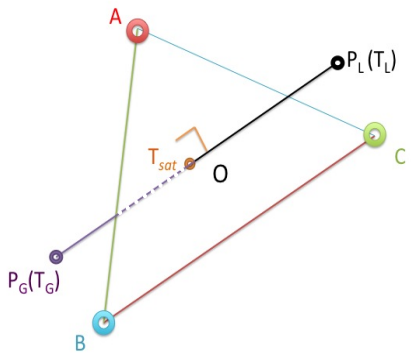

Figure 5.3. Two points in the gas and liquid phases normal to the element employed to compute the conduction heat fluxes in both phases.

plement phase change. In important assumption made in this method is that the convective fluxes across the interface is negligible compared to the conductive fluxes. The model is implemented in the front tracking framework as follows:

a) The mass flux across the interface is computed using the flux-deficit relation:

$$F_{cond,f} - F_{cond,g} = \dot{m} L_v, \tag{5.9}$$

or,

$$k_f \frac{\partial T}{\partial n}_f - k_g \frac{\partial T}{\partial n}_g = \dot{m} L_v. \tag{5.10}$$

Figure 5.3 shows an element along with two points P_L and P_G in the liquid and gas phases respectively. The two said points are along the direction normal to the element drawn from its centroid O. The distance of P_L and P_G from O is one grid-size $1.7\Delta x$.

b) Given points P_L and P_G, we compute the temperatures at those points using interpolation from the surrounding Eulerian temperature field. We use the Peskin interpolation technique [105] to find the temperatures at points P_L and P_G respectively. One has to be careful in choosing the distance between P_L and O such that in interpolating the temperature at P_L we only use information from the liquid phase.

The same applies to the gas phase and point P_G. This criterion is ensured by choosing the reference points to be at distance of $1.7\Delta x$ from the front.

c) To compute the temperature gradients on the liquid and gas sides using a first order approximation, we use the following relation:

$$\left(\widehat{\frac{\partial T}{\partial n}}\right)_{L,G} = \frac{T_{L,G} - T_{sat}}{1.7\Delta x}. \tag{5.11}$$

The above relation is then plugged into Equation 5.10 to compute the local mass flux at the element of interest.

d) Once we compute $\dot{m}$, the mass flux at the element, we can compute the volumetric mass conversion rate from liquid to vapor, $\dot{M}$ using a smoothing function as:

$$\dot{M} = \int_f \dot{m}\delta(\mathbf{x} - \mathbf{x}_f)d\mathcal{A}_f. \tag{5.12}$$

This is done using Peskin weights [105]. Given the volumetric mass conversion rate $\dot{M}$, we can compute the local divergence using the relationship:

$$\nabla \cdot \mathbf{u} = \dot{M}\left(\frac{1}{\rho_g} - \frac{1}{\rho_l}\right). \tag{5.13}$$

e) The divergence computed above is then plugged back into Equation [**?**], and the Navier-Stokes equations are solved with this non-zero divergence field using the projection method [102].

In the absence of any phase change, the front is advected using the velocity information from the Eulerian grid points. In the presence of phase change, in addition to the conventional velocity interpolated from the Eulerian grid points, we have add the jump velocity that occurs due to volume expansion/contraction. The velocity of the gas-liquid interface is given by the relation:

$$\mathbf{u}_i.\hat{n} = \frac{1}{2}\left(\mathbf{u}_f + \mathbf{u}_g\right).\hat{n} - \frac{\dot{m}}{2}\left(\frac{1}{\rho_l} + \frac{1}{\rho_g}\right). \tag{5.14}$$

Here, $\hat{n}$ is the direction normal to the element whose points are to be advected. The first term of Equation 5.14 is the velocity interpolated from the surrounding eulerian field. The second term is the velocity jump due to phase change. The tangential velocity at the interface is computed using conventional interpolation using the eulerian information. After computing u_i, the front points are advected using the explicit forward-eulerian time advancement:

$$\mathbf{x}_p^{n+1} = \mathbf{x}_p^n + \mathbf{u}_i^n dt \tag{5.15}$$

5.2.4 Conjugate heat transfer, outflow boundary conditions

To complete the discussion on the numerical method, we discuss the additional changes made to the conventional numerical methods used for flow computations to accomodate phenomena like conjugate heat transfer between the liquid and solid walls, and outflow. In problems typically involving boiling flows, there is lateral heat transfer along the walls of the heated surface. In order to accomodate this conjugate heat transfer, we make the first layer of computational cells have the properties of the metal that the heated surface is made up of. This also involves making the velocity field and the convective heat transfer this first layer of cells equal to zero. For simplicity, we shall refer to this first layer of cells as the 'conjugate cells' henceforth.

$$(\nabla \mathbf{u}) . \mathbf{n}_{out} = 0 \tag{5.16}$$

Since flow boiling usually involves flow through constricted channels, we need to ensure that outflow boundary condition employed does not result in unphysical velocity fields upstream of where the flow is truncated. There are several conventional methods used to implement outflow in a channel flow. The most popular one being the zero-normal velocity gradient 5.16 often accompanied by a pressure boundary condition at outflow. The attraction of this method is its simplicity, but the disadvantage is that it may result in unrealistic solutions for the velocity field if the channel length is short. This problem was solved by Orlanski [109] by proposing a simple advection

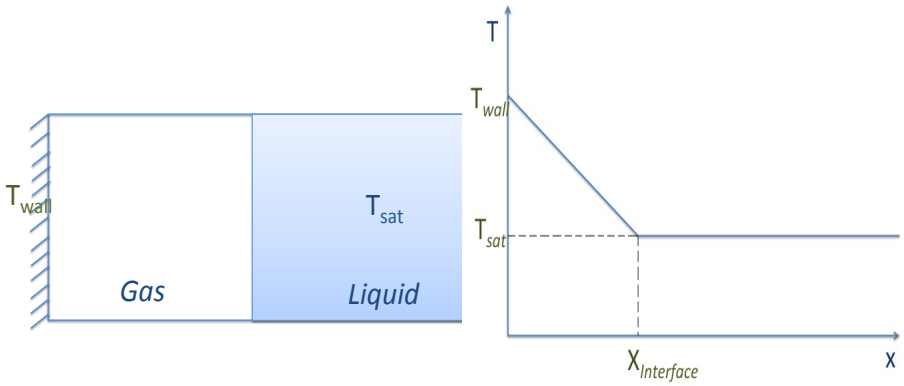

Figure 5.4. (a)Stefan's problem. (b)Temperature distribution.

boundary condition at the outlet. In the present study, we use the first method as the outflow boundary condition. For the energy equation, we use the zero normal gradient condition for temperature as the outflow condition at the channel exit.

5.3 Validation

5.3.1 Stefan's problem

The Stefan's problem is a $1D$ problem with a superheated vapor in contact with a wall and liquid as shown in Figure . The wall is maintained at a constant temperature (greater than saturation temperature). Due to an imbalance in heat flux across the gas liquid interface, there is evaporation at the interface and as a result, the liquid is pushed outwards. The analytical solution to Stefan's problem is given by Equation :

$$X(t) = 2\chi\sqrt{\alpha_g t}, \tag{5.17}$$

where,

$$T(x,t) = T_{wall} + \left(\frac{T_{sat} - T_{wall}}{erf(\chi)}\right) erf\left(\frac{x}{2\sqrt{\alpha_g t}}\right), \tag{5.18}$$

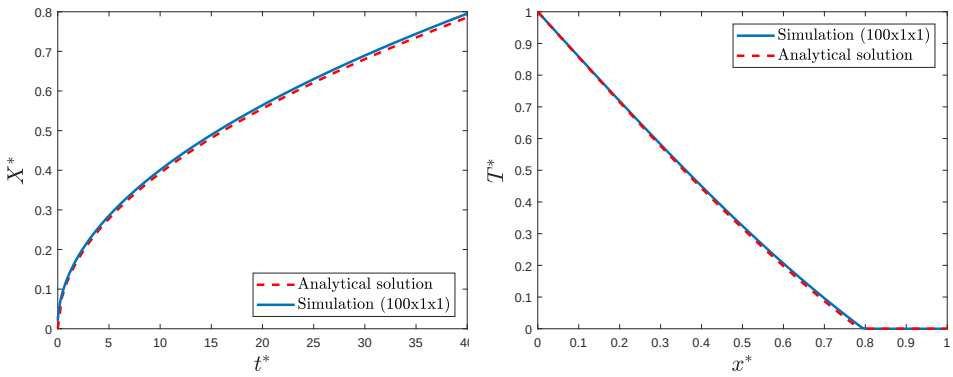

(a) (b)

Figure 5.5. (a)Simulation result for interface position. (b)Temperature distribution.

and χ is the solution to the equation:

$$\chi exp\left(\chi^2\right) erf(\chi) = \frac{C_g(T_{wall} - T_{sat})}{\sqrt{\pi} L_v}. \tag{5.19}$$

To put the model proposed in subsection 5.2.3 to test, we first implement it in a $1D$ code. We consider a fluid with properties: $C_g = C_f = 1J/Kg\text{-}K$, $K_g = K_f = 0.01W\text{-}mK^{-1}$, $\rho_g = 1kg/m^3$, $\rho_g = 100kg/m^3$, and $\Delta T_{sup} = 1K$. Figure 5.5(a) and (b) show schematic depiction of the Stefan's problem. Figure 5.3.1 (a) shows that for 100 nodes along the X direction, the $1D$ simulation matches the analytical solution. Figure 5.3.1 (b) shows a comparison between the temperature profiles obtained from the simulation and the analytical solution.

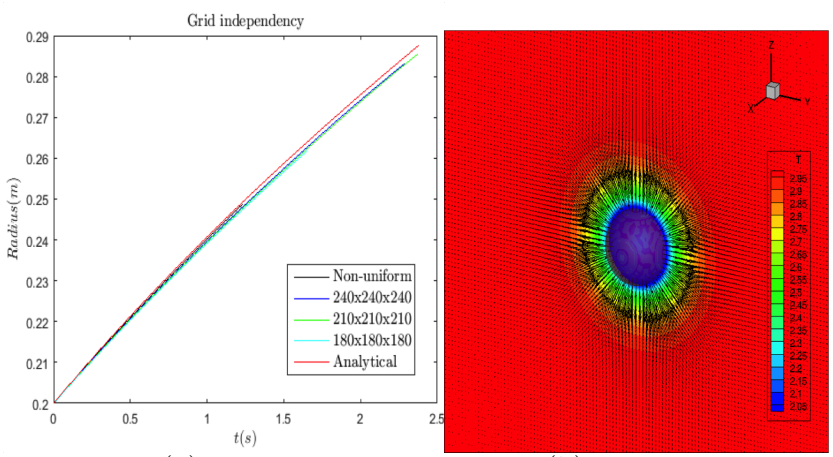

Figure 5.6. (a)Comparison of simulation with analytical radius. (b)Snapshot of the simulation showing temperature contour and velocity vector.

5.3.2 Bubble growth problem

Bubble growth in superheated liquid is another standard problem widely used to validate phase change numerical models. The problem involves the growth of a bubble at saturation temperature in an infinite stagnant liquid. The analytical solution to this problem is as follows:

$$R = 2\beta_g \sqrt{\frac{\lambda_l}{C_l \rho_l} t}, \tag{5.20}$$

where,

$$\frac{\rho_l C_l (T_\infty - T_{sat})}{\rho_v (L_v + (C_l - C_g)(T_\infty - T_{sat}))} = 2\beta_g^2 \int_0^1 exp\left(-\beta_g^2 \left((1-\psi)^{-2} - 2\left(1 - \frac{\rho_g}{\rho_f}\right)\psi - 1\right)\right) d\psi. \tag{5.21}$$

We consider a liquid with the following properties: $C_g = C_f = 1J/Kg\text{-}K$, $K_g = K_f = 0.01W\text{-}mK^{-1}$, $\rho_g = 1kg/m^3$, $\rho_g = 100kg/m^3$, and $\Delta T_{sup} = 1K$. The initial radius of the bubble in our simulation is $R_o^* = 0.2$. The analytical solution to the temperature at a time when the bubble radius equals $0.2m$ is specified as the initial

Table 5.1.
Parameters used in flow boiling simulations in the present study.

Case	L_y	L_z	L_x	$N_z(=N_y)$	N_x
1	$229\mu m$	$229\mu m$	$4L_y$	40	$4N_y$
2	$2000\mu m$	$2000\mu m$	$4L_y$	80	256
3	$232\mu m$	$232\mu m$	$1200\mu m$	60	300

condition. Figure 5.6(b) shows a the temperature contour at a certain point in the simulation. The saturation temperature for this case is $T^*_{sat} = 0.5$. Figure 5.6(a) shows that grid independency is achieved at a grid configuration of 180x180x180 with a uniform grid. This validates our phase change model as applied to a $3D$ configuration.

Table 5.2.
List of parameters corresponding to Mukherjee *et al.* [73]

Working fluid	Re	D_h	G	ΔT_{sup}
Water	100	$229\mu m$	$146kgm^{-2}s^{-1}$	2^oC

5.3.3 Flow boiling: Comparison with Mukherjee *et al.* [73]

Mukherjee *et al.* [73] performed experiments on micro-channel with of a rectangular cross-section and hydraulic diameter $229\mu m$. They maintained the wall temperature at 102^oC and used water at atmospheric pressure as the working fluid. They observed

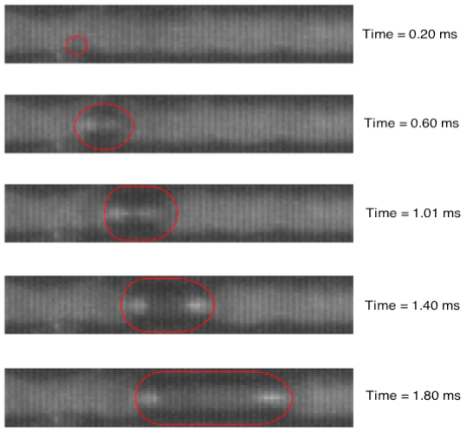

Figure 5.7. Experimental images of Mukherjee *et al.*for a superheat of 2^oC.

the nucleation, and growth of a single bubble into an elongated slug bubble eventually occupying the whole channel along the span-wise direction. They also performed numerical simulations of the same problem using the Level-set method. They used the numerical method proposed by Son *et al.* [67]. They recorded the equivalent diameter of the bubble as a function of time from the experiments and from their Level-set simulations.

Bubble growth in a superheated layer of liquid is sensitive to the superheat. In the simulations of Mukherjee *et al.*, they assumed the whole liquid in the micro-channel to be at a temperature equal to 102^oC. We use the same initial and boundary conditions as used by Mukherjee *et al.*, ie., for the inflow condition, we use a velocity profile with average velocity equal to $0.146m/s$ satisfying the poisson equation:

$$\mu\nabla^2 u_x = \frac{\partial P}{\partial x}, \tag{5.22}$$

where, $\frac{\partial P}{\partial x}$ is a function of the flow rate. The parameters for our simulation correspond to Case 1 in Table 5.1. For the outflow we use the pressure boundary condition. In our simulation we assume that the bubble nucleates at a corner. Figure 5.8(a) shows the side-view of a slice passing through the bubble at the end of the simulation show-

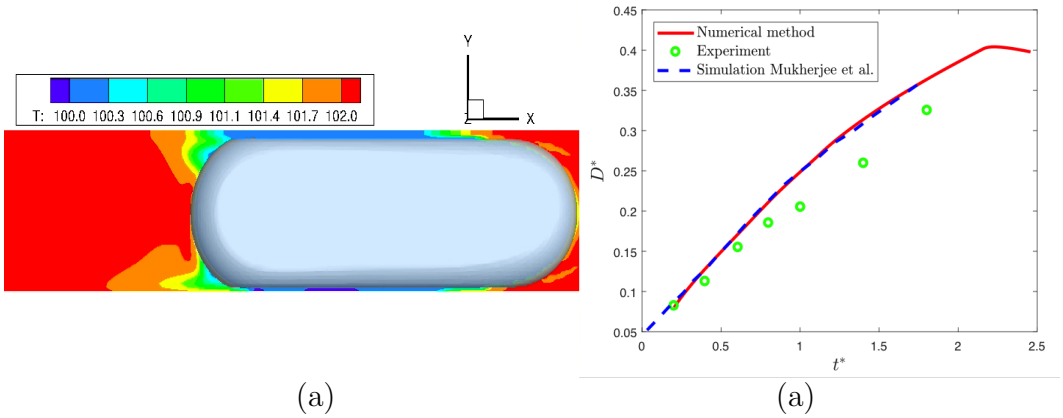

(a) (a)

Figure 5.8. (a) Snapshot of the bubble at the end of the simulation. (b) Comparison between the Mukherjee *et al.*, and our simulation.

ing the temperature contour. Figure 5.8(b) shows that our simulation result matches almost perfectly with the simulation performed by Mukherjee *et al.*. However, there is a discrepancy between both simulations and the experimental findings of Mukherjee *et al.*. This deviation can be attributed to the fact that since we assumed the temperature in the micro-channel to be uniform and equal to 102^oC. Since a more accurate initial condition would be a thermal boundary layer over the wall with maximum temperature being 102^oC, the simulations seem to over-predict the bubble growth. Understandably, the deviation is larger as the bubble grows. Another characteristic feature of the simulation is the fact that the slope of the graph in Figure 5.8(b) shows decreases after the bubble attains an equivalent diameter equal to the channel hydraulic diameter. We also find a similar trend in the experimental data of Mukherjee *et al.*.

5.3.4 Flow boiling: Comparison with Yoo *et al.* [103]

Next, we test the proposed model with an experiment involving the effect of gravity. We also look at the effect of multiple bubbles being injected into the channel. Yoo

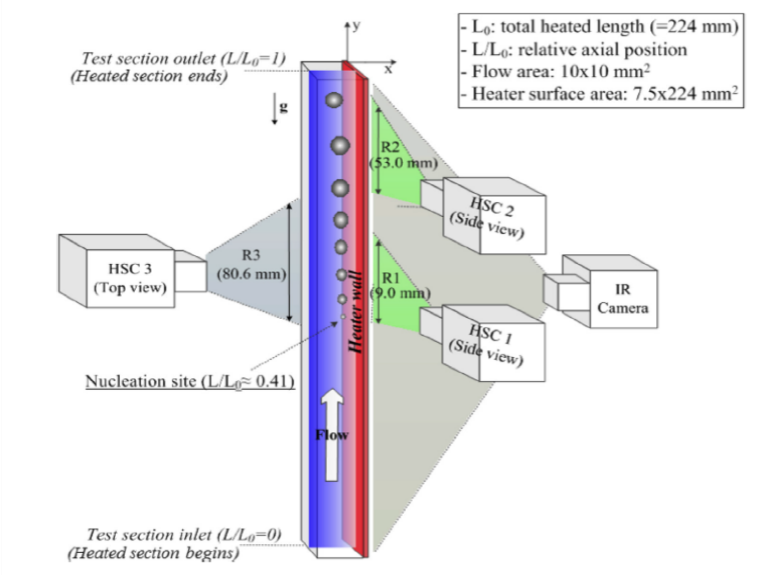

Figure 5.9. Experimental setup of Yoo *et al.* [103] for vertical flow boiling.

et al. [103] conducted experiments of vertical flow boiling in a channel of $10mm$x$10mm$ cross-section with a length of $224mm$. The used HFE-301 at the working fluid for their experiment. Their experimental setup consisted of an artificial cavity midway along the channel ($x = 92mm$) in the flow direction. They used cameras to capture the side-view and top-view images of the bubbles at various instances of time. Yoo *et al.*performed experiments over a wide range of mass flow rates and heat fluxes and they recorded the evolution of the diameter as observed from the side-view and top-view along the flow direction. They also report the bubble ejection frequency and the Jakob number at the nucleation site. This information is helpful to set up accurate initial conditions for our simulations. We consider a case with parameters shown in Table 5.3. Figure 5.9 shows a schematic taken from Yoo *et al.* [103] showing their experimental setup. As mentioned before, bubble growth is sensitive to the initial condition that we use for the energy equation, and therefore, one has to be careful in initializing the two-phase simulation. We use the following procedure for running the two-phase simulations:

Table 5.3.
List of parameters corresponding to Yoo *et al.* [103]

Fluid	Re	D_h	q"	G	$\overline{Ja}_{nuc}$
HFE-301	100	$10mm$	$9.3kW/m^2$	$140kgm^{-2}s^{-1}$	34.1

a) Run a single-phase flow simulation with the mass flow rate and inlet sub-cooling reported by the experimental study of interest. Use the superheated wall temperature reported in the experimental study as the wall boundary condition for the energy equation.

b) Let the single-phase flow simulation with conjugate heat transfer reach steady state and record the temperature profile at steady state at the site of nucleation (in the present case, $x = 92mm$).

c) Now use this temperature profile as the initial condition for two-phase flow simulation. Since Yoo *et al.* [103] used a channel of cross-section $10mm$x$10mm$ and the bubbles the observed were of diameter $1mm$ at the most, we do not need to simulate the whole flow and heat transfer in the whole channel. So we consider only a $2mm$ x $2mm$ cross-section containing the nucleation site for our two-phase flow simulation. From the single phase flow simulation, we record the temperature and velocity profile in this $2mm$ x $2mm$ window and use it as the initial condition for the two-phase flow simulation. The parameters for our simulation correspond to Case 2 in Table 5.1. We define the non-dimensional temperature as follows:

$$Tm = \frac{T - T_{sat}}{10^oC} + 0.5. \tag{5.23}$$

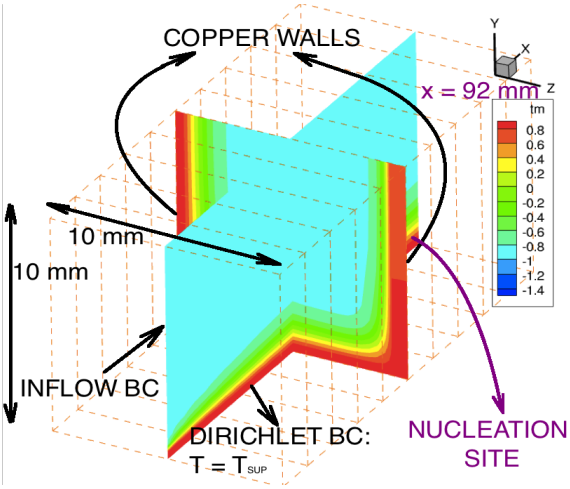

Figure 5.10. Single-phase flow simulation with conjugate heat transfer to generate initial conditions at the nucleation site for two-phase flow simulation.

We also scale the energy equation using the above definition. A Jakob number of 34.1 corresponds to a wall superheat of 13^oC at the wall. The boiling point of the working fluid is 78^oC and the inlet sub-cooling was given to be 13^oC in the experimental data corresponding to the present case. Given the definition of non-dimensional temperature in Equation 5.23, we see that the inlet temperature is $Tm = -0.85$ and wall temperature corresponds to $Tm = 1.85$. With these conditions, we simulate the single phase flow to get the initial condition for the two-phase flow simulation. A sample conjugate heat transfer simulation with wall temperature $Tm = 0.85$ is shown in Figure 5.10. For the two-phase simulation, we initially choose a computational domain that is $2mm$ tall along the Y direction, $1mm$ wide along the Z direction, and $4mm$ long the X direction. The nucleation occurs at $(x, y, z) = (0.25mm, 0mm, 0.5mm)$. For the two-phase flow simulation, we use a Neumann boundary condition corresponding to a heat flux of $9.3kW/m^2$ at the bottom Y wall. As mentioned earlier, the first layer of cells along the bottom Y wall and the two Z walls is filled with material having thermal properties of copper.

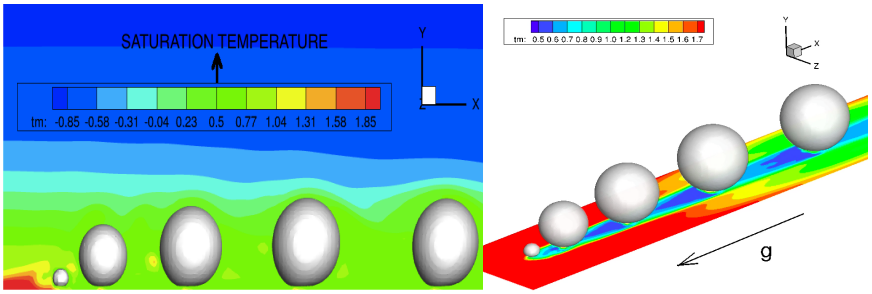

(a) (a)

Figure 5.11. (a) Side-view of the simulation at steady-state. (b) Isometric view showing the wall temperature contour.

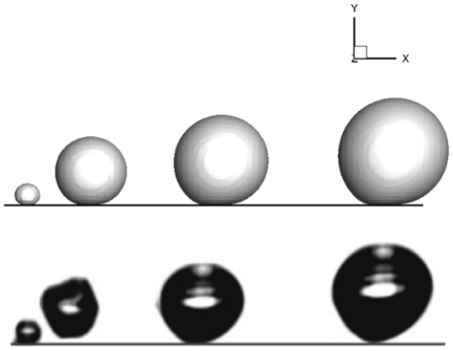

Figure 5.12. Visual comparison between the simulation (top) and experimental images of Yoo *et al.*(bottom).

A new bubble is added into the domain after the latest bubble reaches a certain distance from the point of nucleation. This distance is determined using the experimental images provided by Yoo *et al.* [103] in their paper. When the latest bubble reaches the position of the second bubble in Figure 5.12 - bottom, a bubble of the diameter of the first bubble is injected into the simulation. Figure 5.11(a) shows a snapshot showing the side-view of the simulation at a certain time instance. We see that the bubbles are exposed to both the superheated and sub-cooled regions in the channel.

Therefore bubbles experience boiling close to the wall and condensation away from the wall. Figure 5.11(b) shows the effect of the bubble on the wall temperature. It is to be noted that in the present study we don't use any film model to simulate the thin film between the bubble and the wall [91]. While experimental evidence [91] points towards the existence and importance of a thin film beneath the bubble during nucleation, several studies [73,75,76,99] have performed successful boiling simulations without using a film model. Although we need to work towards developing a robust film model to accompany our macro-scale simulations, present results without film modeling in the present section. Figures 5.13 (a) and (b) show a reasonable match between the experimental and simulation bubble diameters as seen from the top view and the side view of the channel.

For the outflow boundary condition, we employ the zero normal gradient of velocities accompanied by the pressure boundary condition at the outlet of the channel. Since there is an excess pressure inside the bubble due to surface tension, the constant pressure boundary condition does not allow a bubble to exit through the outlet. To overcome this problem, we make the bubble disappear from the computational domain after it covers 95% of the length of the computational domain along the flow direction. This unphysical removal of bubbles from the computational domain has an impact on the simulation results. Understandably, this effect diminishes as we increase the length of the computation domain. This can be seen in Figure 5.13(c), where as the length and width of the computational domain is increased, the simulation is found to yield results that better match the experimental data.

It is also to be noted that in the experiments of Yoo *et al.* [103], the bubbles were observed to bounce off the wall after nucleation, as can be seen in Figure 5.12 and also from the sharp local peaks observed in Figures 5.13 (a) and (c). We don't observe this phenomenon in our simulations. However, from both our simulation results and the experimental observations of Yoo *et al.* [103], it is clear that the bubble diameter evolution can be separated into two regimes: Firstly, the nucleation regime with

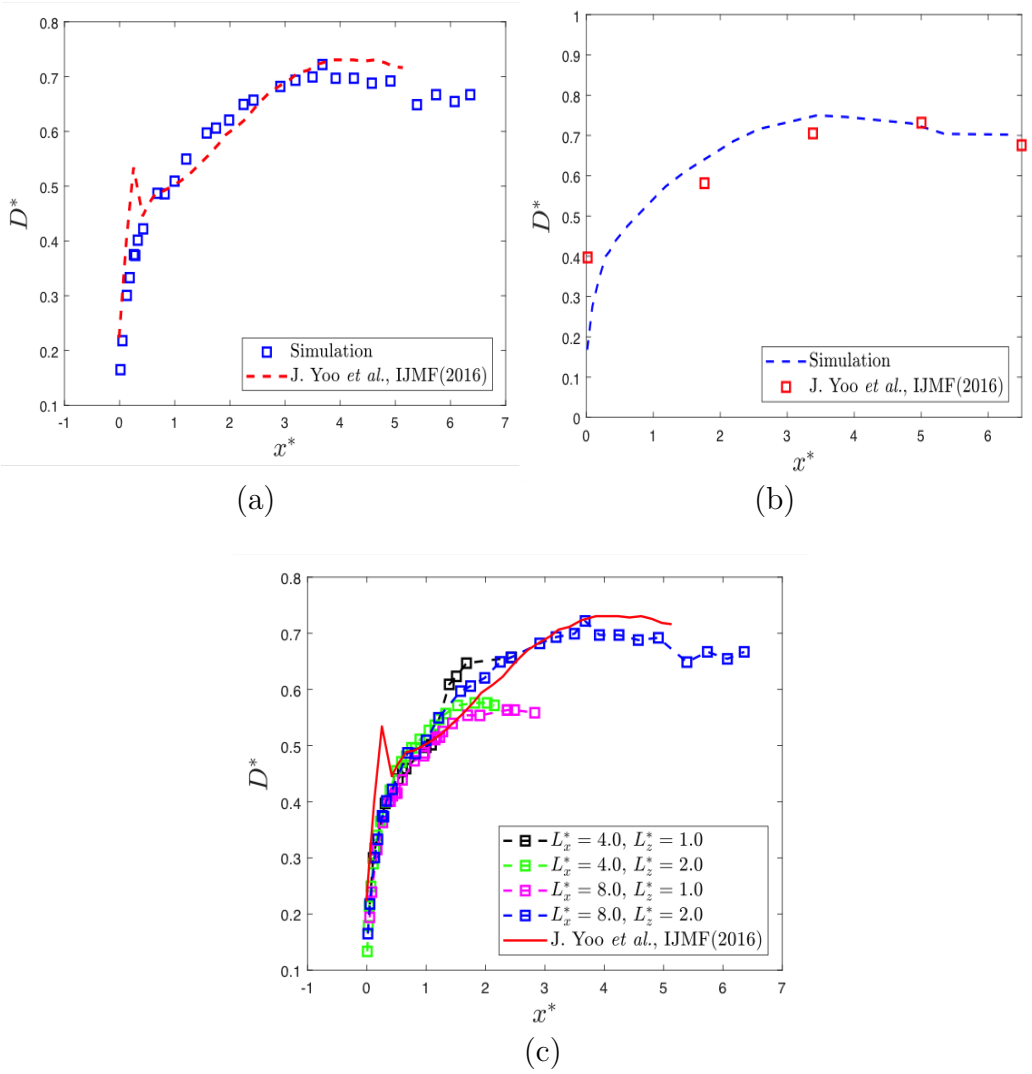

Figure 5.13. Comparison between the simulation and experimental data from the (a) Side view and (b) Top view. (c) The effect of changing the channel length and width of the computational domain on the simulation result.

rapid bubble growth marked by the initial steep region, and Secondly the flow boiling regime with the bubble experiencing boiling near the wall and condensation above.

Table 5.4.
List of parameters used in our flow boiling simulations

Case	Fluid	Re	D_h	G	ΔT_{sup}
1	Water	100	$0.2mm$	$146kgm^{-2}s^{-1}$	5 ^oC
2	Water	100	$0.2mm$	$146kgm^{-2}s^{-1}$	10 ^oC

5.4 Summary

In summary, we proposed a technique that is based on the front-tracking method and borrows from Sato *et al.* [77]. From a review of literature on the various mass transfer models we choose the flux-deficit model due to its simplicity and ease of implementation. We validated our model using benchmark problems such as Stefan's $1D$ problem and the bubble growth in superheated liquid problem, the analytical solutions to which are available in literature. The model was also validated by comparison with the experiments and simulations performed by Mukherjee *et al.* [73], for nucleation and growth of a water bubble in a micro-channel. We then validated our model with the experimental study by Yoo *et al.* [103], on vertical up-flow boiling from an artificial cavity in a channel of $10mm$ x $10mm$ cross-section. We used the approach of running single-phase simulations to obtain steady state solutions for temperature and velocity fields at the nucleation site that are then used a initial conditions for two-phase flow simulations. Our simulation shows good visual and quantitative comparison with the experimental results presented in Yoo *et al.*'s work [103]. We then used the validated numerical model to study the effect of wall superheat on the bubble growth and wall temperature.

6. FLOW BOILING IN MICRO-CHANNELS: IMPACT OF INLET FLOW RATE AND HOT-SPOT

In this chapter we use the numerical method described before to study the bubbly flow regime in the flow boiling in a micro-channel heat sink. The dimensions of the micro-channel heat sink are the same as those used by Mukherjee *et al.* [73] in their study. The working fluid is assumed to be water. We are interested in examining the effect of the inlet flow rate and the having a hot-spot on the bubble size distribution in the micro-channel.

6.1 Literature review

Abarajith *et al.* [69] used the level-set method to study the effect of contact angle on the departure time and diameter of a single bubble in nucleate pool boiling. Son *et al.* [70] used the same method to study the coalescence of a departed bubble with the subsequent bubble and its effect on heat transfer characteristics and departure diameter of the bubble. Li *et al.* [71] studied the effect of background flow on departure characteristics of bubbles in horizontal and vertical flows. They used a wall superheat of $5.3K$ and a flow velocity of $0.076\ m/s$ with a specified contact angle at the wall.

Mukherjee and Kandlikar [73] used the level-set method to simulate the growth of a bubble into a slug flow. They conducted an experiment of flow boiling in a microchannel of hydraulic diameter $0.2\ mm$ with a wall superheat of $2K$. Their numerical simulation shows a good comparison with the experiment in terms of the equivalent bubble diameter as a function of time. They also found that restrictions at the inlet of the channel reduces the bubble growth rate [75]. Mukherjee *et al.* [76] studied the wall heat transfer during bubble growth in flow boiling. They found that the surface

tension and flow rate have little influence on the wall heat transfer. But the bubble with the lowest contact angle resulted in the highest heat transfer rate in their study. Sato and Niceno [77] used VOF [51–53] to build a phase change model to study nucleate boiling. They imposed the saturation temperature at the interface by modifying the numerical schemes used to compute diffusion and convection. They also studied the transition of vapor bubble regime from discrete bubbles to the vapor mushroom regime [90].

Magnini, Pulvirenti and Thome [93] used VOF to run $2D$ axisymmetric simulations of elongated slug bubble flow in a micro-channel of circular cross-section. They found the film heat transfer to be the dominant phenomenon of heat transfer. Esmaeeli *et al.* [96,97] carried out computations of film boiling using the front-tracking method. Sun *et al.* [98] simulated bubble growth and departure in nucleate pool boiling using the Lattice-Boltzmann method. They found the dependence of bubble departure diameter and bubble departure frequency on the acceleration due to gravity. Jafari *et al.* [99] used the Cahn-Hillard phase field method to simulate bubble growth and departure from an artificial cavity in a micro-channel of cross-section $100\mu m$x$100\mu m$ and compared their results with Lee *et al.* [100].

While several successful attempts have been made to reproduce experimental results of nucleate pool boiling, there has been limited success in reproducing transient flow boiling data with multiple dispersed bubbles. Kharangate and Mudawar [110] give a comprehensive review on all the progress made in the field of boiling computational fluid dynamics over the past couple of decades. There is a scarcity of literature presenting numerical methods that can effectively handle regimes of flow boiling such as the bubbly flow regime. In the present work, we aim to address this gap by numerically examining the bubbly flow regime in a micro-channel, and its sensitivity to factors such as the inlet flow rate, and a hot-spot.

6.2 Numerical method and problem set up

We solve the momentum equation and the temperature equation using the finite-volume method using the front tracking method [28] for interface tracking. The momentum equations are solved using the explicit Euler time advancement scheme, and the energy equation is solved semi-implicitly. We use the numerical method developed in chapter 5 to simulate the flow boiling problems in the present chapter. We employ an inflow boundary condition and an outflow boundary condition along with four wall boundary conditions to model the channel flow. For all the simulations henceforth we consider a micro-channel with dimensions $X_L = 2.4mm$, $Y_L = 230\mu m$, and $Z_L = 230\mu m$, with the working fluid as water. We consider five different mean inlet velocities: $0.3m/s$, $0.5m/s$, $0.6m/s$, $0.7m/s$, and $0.9m/s$, corresponding to Mass-velocities: $288Kgm^{-2}/s$, $480Kgm^{-2}/s$, $576Kgm^{-2}/s$, $672Kgm^{-2}/s$, and $864Kgm^{-2}/s$ respectively. We perform two sets of simulations, the first one having a uniform heat-flux of $50W/cm^2$ at the bottom of the channel, and the second one with hot-spots at the bubble nucleation site in addition to a flux of $50W/cm^2$ everywhere else. In all the cases, the wall temperature at the nucleation site is chosen to be 110.5^oC. Therefore, as a precursor to each of the mentioned two-phase simulations, we run a single phase simulation with a much longer channel of length $100mm$, with the desired inlet flow rate and a flux of $50W/cm^2$ to determine the point along the channel where the temperature first attains 110.5^oC. At this instant in the simulation, we record the temperature profile at the said point and use it as the initial condition for the subsequent shorter channel two-phase simulation. The computational domain is surrounded by one layer of cells containing copper as shown in the Figure 6.1. We use stretched grids for all our simulations with the mesh refined near the site of bubble nucleation. In the present study the nucleation process is not modeled for each bubble and the bubbles are simply injected at the 'nucleation site'. The nucleation site is at a distance of 0.1mm from the beginning of the channel. At the inlet of the channel we use an inflow boundary condition with specified velocity and

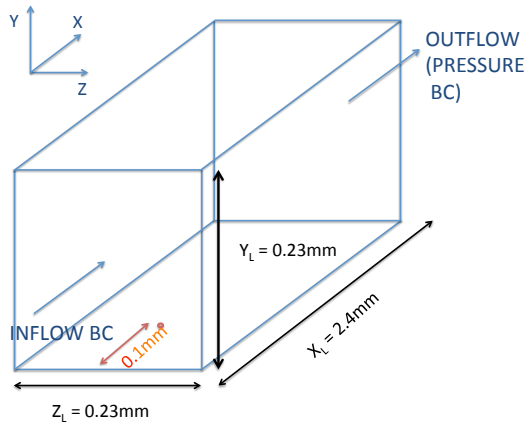

Figure 6.1. Schematic of the setup.

temperature profiles. At the outlet we use a zero-normal velocity gradient boundary condition along with specifying a constant pressure. All the remaining faces of the computational domain have no-slip boundary conditions. For the energy equation, we use a Neumann boundary condition with constant flux at the bottom face of the channel, and a zero-Neumann boundary condition at the top face. The left, right, and bottom faces of the computational domain have one layer of cells each with properties of copper. There are no convective heat transfer and momentum in these cells. At each time-step we monitor the temperature at the nucleation site and when the temperature reaches a value of 110^oC, a new bubble is introduced into the computational domain. The heat transfer coefficient is defined as:

$$h = \frac{q"}{(T_{wall} - T_f)}, \tag{6.1}$$

where

$$T_f = \frac{\int_0^{Y_L}\int_0^{Z_L} T u dy dz}{\int_0^{Y_L}\int_0^{Z_L} u dy dz}. \tag{6.2}$$

T_{wall} is the wall temperature averaged along the Z direction at a given X. We record the heat transfer coefficient averaged at each X location, and averaged throughout

the bottom wall. We define the non-dimensional heat transfer coefficient h^*, distance x^*, and time t^* as:

$$h^* = \frac{h}{1000 W m^{-2} K^{-1}},$$
$$x^* = \frac{x}{10^{-3} m},$$

and

$$t^* = \frac{t}{10^{-3} s},$$

respectively. For each case, we monitor the bubble injection frequency, the bubble diameter evolution, and the heat transfer coefficient. Since the present study is focused on the bubbly-flow regime, we do not study cases where the bubbles evolve into slug flow. All the bubbles observed in the present study are poly-dispersed with effective diameters smaller than the channel hydraulic diameter.

6.3 Results and discussion

6.3.1 Effect of inlet flow rate

The results presented in this section correspond to a heat flux of $q" = 50 W/cm^2$, and inflow velocities of $0.3 m/s$, $0.5 m/s$, $0.6 m/s$, $0.7 m/s$, and $0.9 m/s$. We observe that each of these inflow velocities result in different frequencies of bubble injection. Figure 6.3.1(a) shows the temperature at the nucleation site for an inlet velocity of $0.5 m/s$. When the temperature exceeds $110.5^o C$ a new bubble is introduced at the nucleation site causing the temperature to dip sharply and then rise again. The periodic nature of the temperature at the nucleation site indicates that the process of nucleation and departure of bubbles has reached a quasi-steady state. For each of the cases presented more than 20 bubbles were injected and Figure shows the history of the nucleation site for the first 15 bubbles. A similar plot of the temperature history of the nucleation site is observed for all the other inlet velocities. Figure 6.3.1(b) shows the evolution of the temperature at the exit of the channel, indicating that the simulation has reached statistical steady state with a mean temperature of $105^o C$. The time period of the

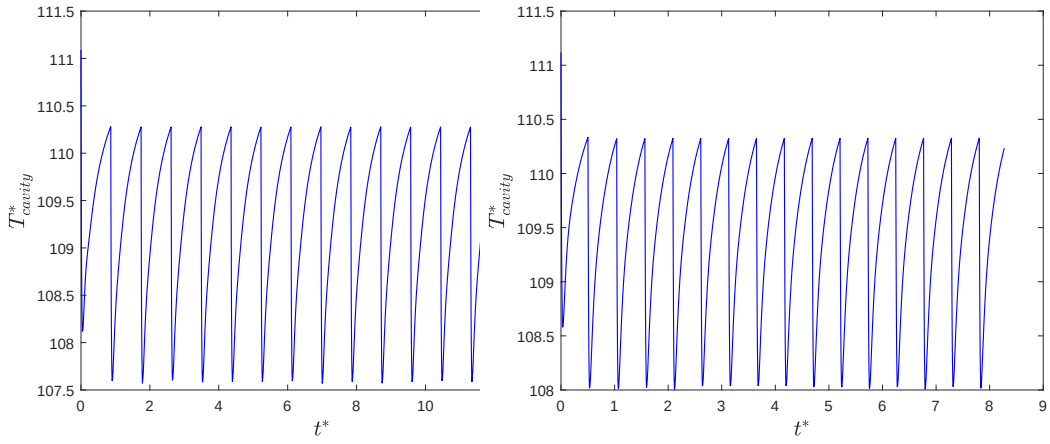

(a) (b)

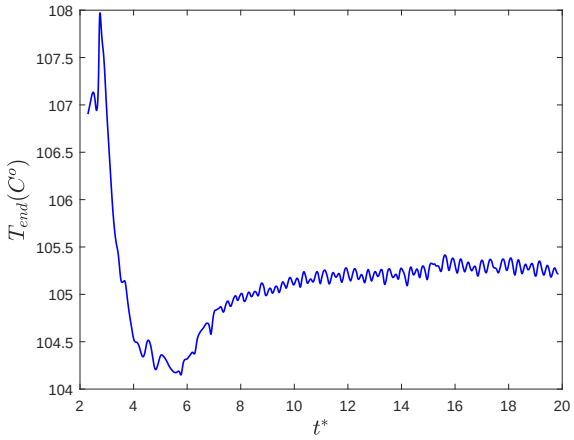

(c)

Figure 6.2. (a)Temperature at the nucleation site for $\overline{u} = 0.5m/s$. (b)Temperature at the nucleation site for $\overline{u} = 0.9m/s$. (c)Temperature at the end of the channel for $\overline{u} = 0.5m/s$.

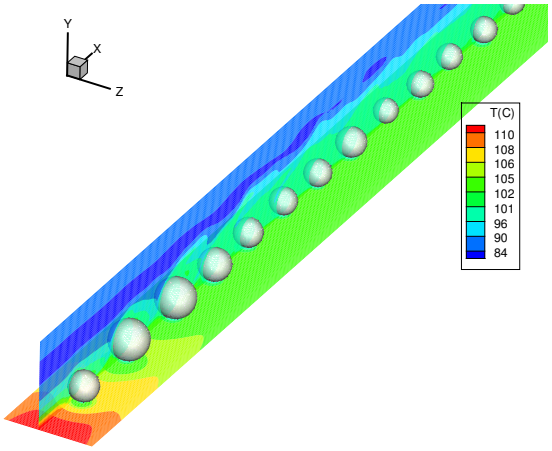

Figure 6.3. Snapshot of the simulation for the case $\overline{u} = 0.7m/s$ at statistical steady state.

temperature oscillations observed in Figure 6.3.1(a) are a function two parameters namely the residence time of the bubble before it detaches from the nucleation site, and the heat flux at the nucleation site. While the former suppresses the temperature at the nucleation site, the latter determines the time taken for the nucleation site to attain the activation temperature.

Shown in Figure 6.3.1 is a snapshot of the simulation for $\overline{u} = 0.7m/s$ when the statistical steady state is reached. The temperature of wall at the outlet is 105^oC. The frequency of injection of the bubbles is seen to increase as the inlet flow velocity increases. This can explained by the fact that a larger background velocity results in a quicker detachment of the bubbles. Larger flow velocities cause higher convective heat transfer, however in this case the effect of the residence and detachment of the bubbles eclipses the convective effect associated with the higher velocities. Figure 6.3.1(a) shows the variation of the bubble injection frequency with the inlet flow velocity. The variation is found to be monotonic and linear. Figure 6.3.1(b) shows the variation of

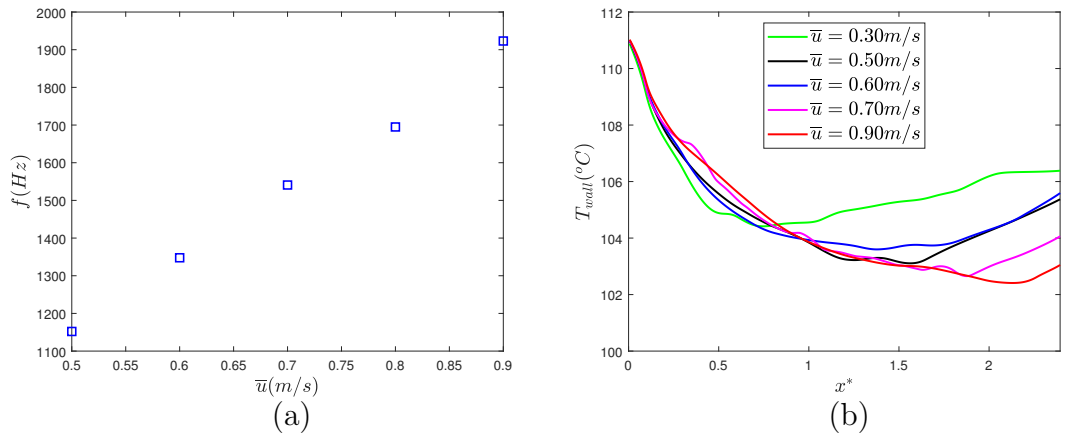

Figure 6.4. (a)Bubble injection frequency. (b)Time averaged wall temperature along the flow.

wall temperature along the flow direction for the different inlet flow velocities. We see that the temperature at the exit of the channel decreases as the flow velocity is

increased. The lower exit wall temperature for higher values of inflow velocity is in part due to the improved convection at higher velocities, and in part due to the larger number of bubbles in the computational domain at a given time. We also observe that the dip in temperature along the flow direction is steeper near the nucleation site for lower inlet flow velocities due to the larger time the bubble spends before detachment. Figure 6.3.1(a) shows the distribution of the bubble diameter along the flow direction

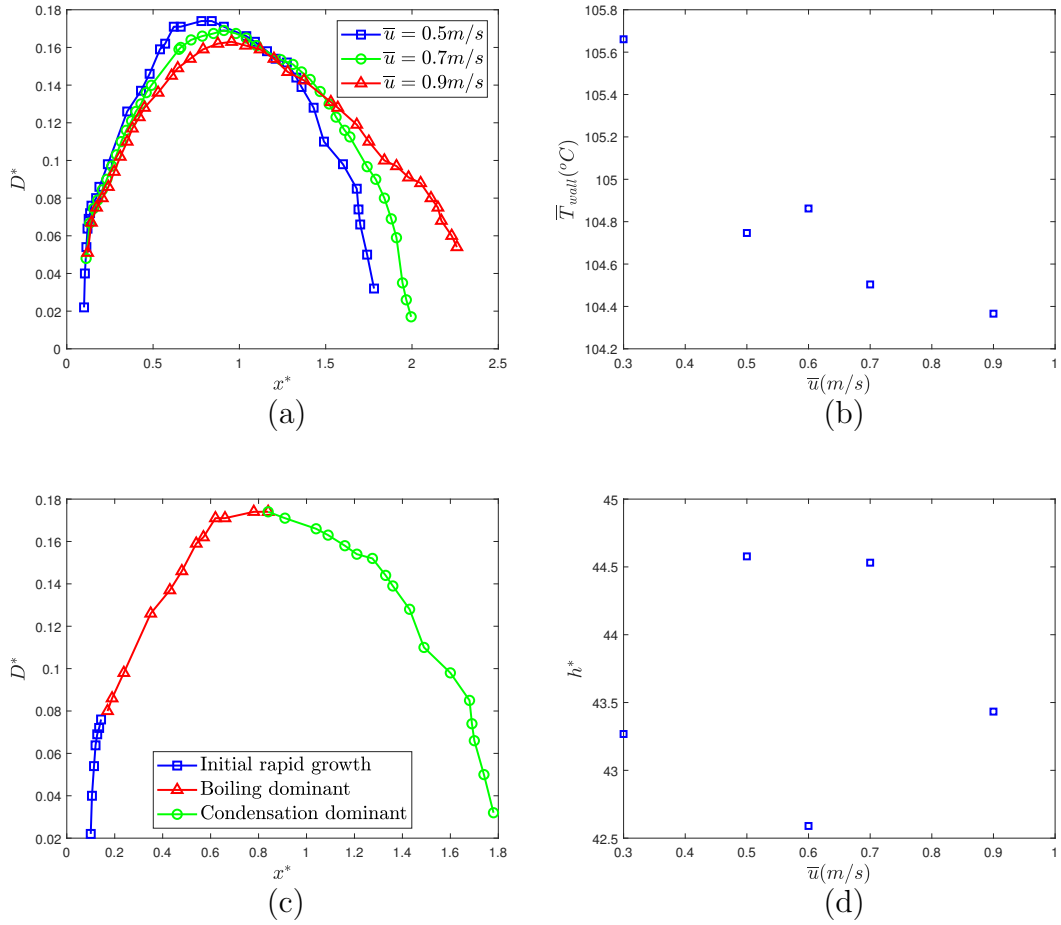

Figure 6.5. (a)Bubble diameter evolution along the flow direction. (b)Time averaged heat transfer coefficient. (c) Three different regimes of bubble evolution. (d) Heat transfer coefficient.

for $\overline{u} = 0.5m/s$,$0.7m/s$, and $0.9m/s$. The diameter distribution is found to become

flatter as the inflow velocity is increased. As the bubbles grows to a diameter larger than the thermal layer thickness, they comes in contact with sub-cooled liquid and undergoes condensation. For all the inflow velocities except $0.9m/s$, the bubbles are found to condense and collapse at point before the end of the computational domain. For all the cases, the diameter at which the bubble was deemed collapsed was the same as the starting diameter of $0.02mm$. Figure 6.3.1(b) shows the wall temperature averaged over time and wall area. We see that besides the case of $\overline{u} = 0.5m/s$, the average wall temperature decreases as the inlet flow rate is increased, and we get an advantage of around 1.2^oC as he inlet flow rate is increased from $0.3m/s$ to $0.9m/s$. We note that the bubble diameter evolution can be categorized into three distinct regimes as shown in figure 6.3.1(c). The first one being the nucleation phase where the bubble diameter increases steeply; the second being the phase where the bubble has detached from the nucleation site and predominantly experiences boiling, and the third being the phase where the bubble predominantly experiences condensation resulting in a decrease in its diameter. Figure 6.3.1(d) shows the average heat transfer coefficient in the computational domain for the various inflow velocities. We do not observe a significant variation in the overall heat transfer coefficient among the different inflow velocity cases, and the mean heat transfer coefficient is found to be nearly twice that of the single phase heat transfer.

6.3.2 Effect of hot-spots

Since hot-spots are commonly encountered in computer chip cooling, it is of interest to study how they affect the heat transfer characteristics in a micro-channel. For this purpose we consider an identical channel geometry as described previously and impose three different hot-spots: $Q_{hs} = 100W/cm^2$, $150W/cm^2$, and $200W/cm^2$. The hot-spots are imposed in a region spanning one bubble diameter along the X direction and Z_L along the Z direction as shown in Figure 6.3.1(a). Additionally, a flux of $50W/cm^2$ is imposed everywhere else. The hot-spot is kept relatively thin in-order

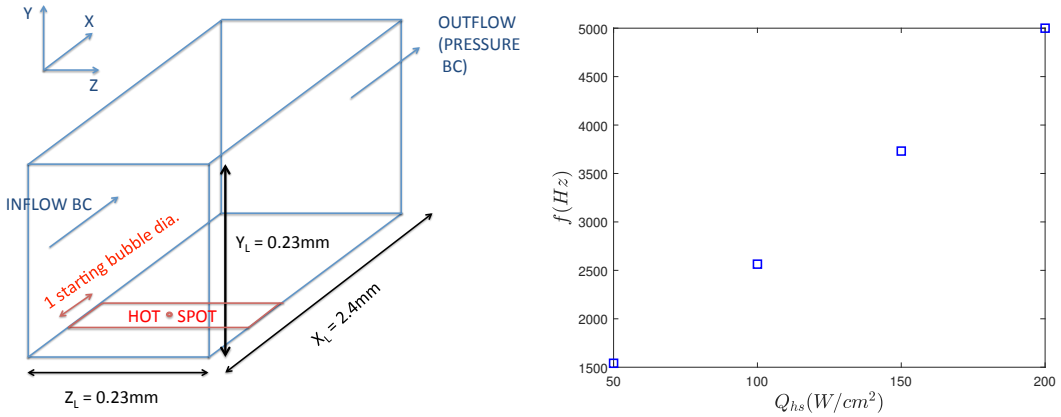

Figure 6.6. (a)Schematic showing the hot-spot imposition. (b)Bubble injection frequency for $\overline{u} = 0.7m/s$.

to not affect the overall heat added to the channel. We are mainly interested in the effect of the hot-spot on bubble nucleation frequency and the local heat-transfer near the hot-spot. The hot-spot is expected to heat up the nucleation site to the activation temperature quicker, thereby leading to a higher bubble injection frequency. This is can be seen in Figure 6.3.2(b). The bubble injection frequency increases from $1500Hz$ to $5000Hz$ for an inflow velocity of $0.7m/s$ as the intensity of the hot-spot is increased from the normative value of $50W/cm^2$ to $200W/cm^2$. Figure 6.3.2 (a) shows that for each inlet flow velocity with a hot-spot, the bubble injection frequency is comparably higher than the case without a hot-spot. We also note that the frequency increases monotonously with the inflow velocity for the cases with the hot-spot. The overall heat transfer coefficient for the cases with the hot-spot is seen to be lower than that with the normative heat-flux, as can be seen in figure 6.3.2(b). Figure 6.3.2(c) shows the temperature distribution along the flow direction in the micro-channel. We see that the temperature for the cases with the hot-spot decreases more steeply compared to the normative heat-flux case initially. In the hot-spot cases the wall temperature oscillates around $T_{wall} = 104^oC$ from $x^* = 1$ until $x^* = 2$, after which it increases. It

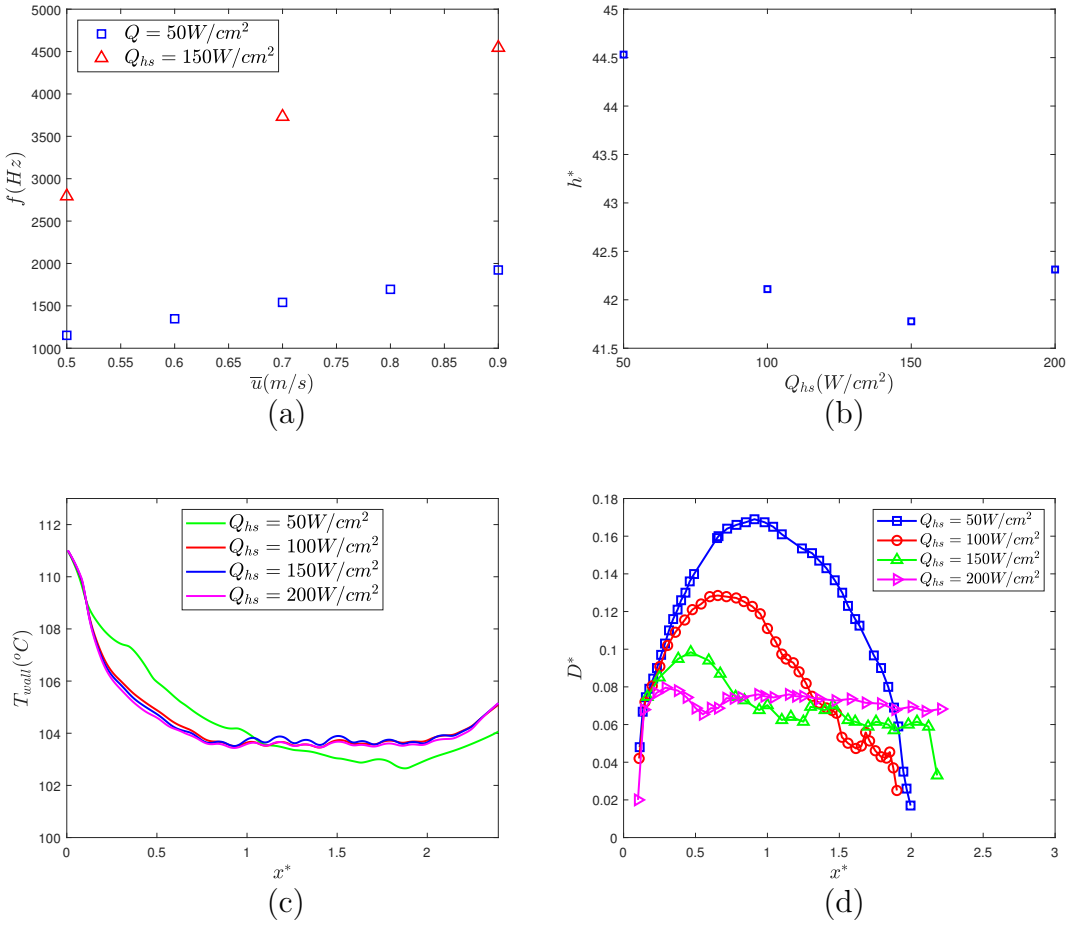

Figure 6.7. (a)Schematic showing the hot-spot imposition. (b)Heat transfer coefficient with $\overline{u} = 0.7m/s$ for the various hot-spots. (c) Wall temperature distribution for different hot-spots for the case of $\overline{u} = 0.7m/s$. (d) Diameter distribution for the case of $\overline{u} = 0.7m/s$.

is interesting to note that in the case of the normative heat-flux, this oscillation in temperature around a fixed value is not observed. Figure 6.3.2(d) shows the variation of the bubble diameter distribution along the micro-channel. A key observation to be made is that the diameter profile gets flatter as the hot-spot intensity is increased. The initial phase of rapid growth is relatively unchanged as the hot-spot intensity is increased, but the boiling-condensation phases are largely different based on the hot-spot intensity. The average bubble diameter in the channel gets smaller as the

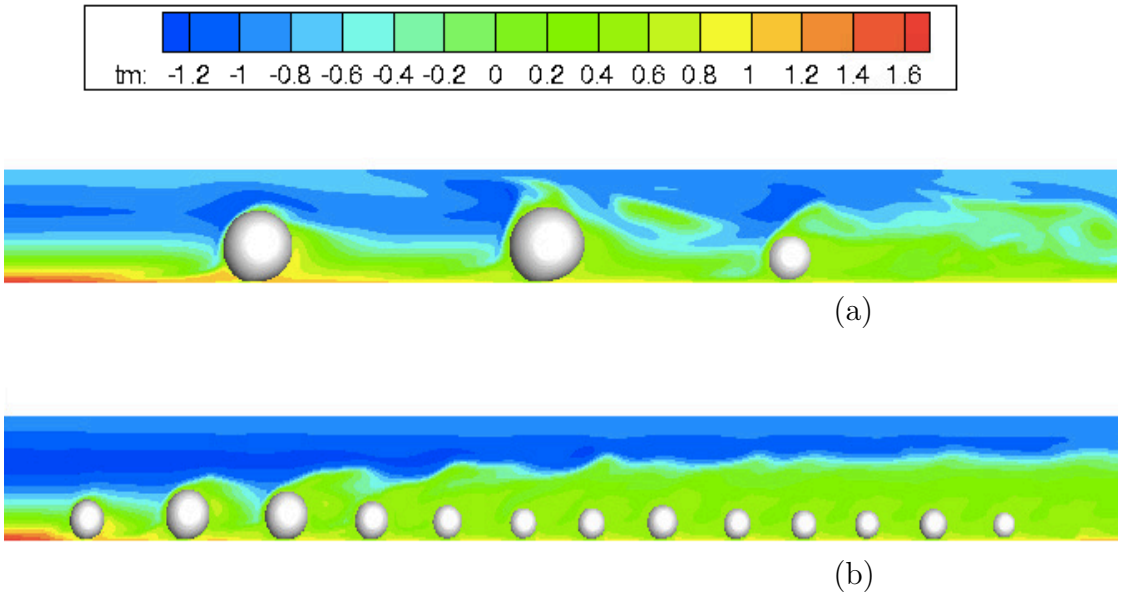

Figure 6.8. Snapshots of the simulations with (a) $\overline{u} = 0.7m/s$, $Q = 50W/cm^2$ and (b)$\overline{u} = 0.7m/s$, $Q_{hs} = 150W/cm^2$.

hot-spot intensity is increased. We observe some oscillations in the bubble diameter in the condensation dominated phase of the cases with $Q_{hs} = 100W/cm^2$ and $150W/cm^2$. Figures 6.3.2(a) and (b) show the bubble size distribution for the normative case and the case with $Q_{hs} = 150W/cm^2$, respectively. tm is the non-dimensional temperature defined as:

$$tm = 0.5 + \frac{T - 100^oC}{10^oC},$$

where T is the temperature in ^oC and $tm = 0.5$ corresponds to the saturation temperature. The difference in the bubble size distribution is a function of the bubble injection frequency. As we can see in figures 6.3.2(a) and (b), the case with $Q_{hs} = 150W/cm^2$ has a larger number of smaller bubbles than the normative case. Since the rate of expansion of the bubble is the largest in the rapid growth stage shown in blue in figure 6.3.1(c), a larger number of bubbles undergoing this stage per unit time would push

the previous bubbles ahead with a larger velocity. This can be expected to increase the entrainment of liquid water in between bubbles.

6.4 Summary

We presented a numerical method based in front-tracking to model phase change in two-phase flows. We validated the method using two benchmark problems and the flow boiling data from an existing study. We used the numerical method to simulate flow boiling in a micro-channel with a hydraulic diameter of $259\mu m$. Simulations of five different mean inflow velocities in the range of $0.3m/s$ to $0.9m/s$ with a constant heat-flux of $50W/cm^2$ showed that the heat transfer coefficient in the channel can be nearly twice that of the single phase flow. We observed that the bubble diameter distribution along the channel can be separated into three phases namely, the rapid growth phase, the boiling dominant phase, and the condensation dominant phase. We observed that the bubble size distribution along the channel got flatter and that the bubble injection frequency increased as the inflow velocity was increased. We simulated three different hot-spots at the nucleation site spanning one starting bubble diameter along the flow direction and we found that an increase in the intensity of the hot-spot causes an increase in the bubble injection frequency. We observed the bubble size distribution along the channel to become flatter as the hot-spot intensity is increased, and we did not observe a significant variation in the overall heat transfer coefficient over the range of hot-spots simulated. In conclusion, the inlet flow velocity and the hot-spot intensity play a significant role in determining the bubble injection frequency, and in turn the bubble size distribution in the micro-channel.

7. NUCLEATE BOILING: THE STUDY OF SLIDING MOTION OF BUBBLES IN FLOW BOILING

The simulations of flow boiling presented thus far have not taken into account the early stages of nucleate boiling that involves the bubble growing from a cavity on the super-heated surface. Nucleate boiling involves the growth of a micro-layer beneath the bubble that accounts for a significant portion of the heat absorbed by the bubble. In the present chapter we refine the numerical method presented in chapter 5 to include a stagnant micro-layer model that would enable us to account for the nucleate boiling phenomenon. We then proceed to use this model to simulate the heat transfer associated with a line of bubbles undergoing boiling under the effect of various shear flows.

7.1 Literature review:

An important phenomenon to consider in the modeling of boiling is the evolution of the micro-layer beneath a bubble during the initial stages of nucleate boiling as reported in the experimental findings of Cooper *et al.* [91] in 1969. Since the micro-layer can be as thin as a few angstroms, and contribute up to 80% of the heat transfer in the initial stages [91], it presents a multi-scale problem to CFD engineers. Son *et al.* [67] were the first to fully simulate nucleate pool boiling including the micro-layer evolution by solving the axisymmetric Navier Stokes equations in $2D$ with a special treatment given to the micro-layer. They solved a fourth-order ODE derived using the lubrication theory for the micro-layer and coupled its solution iteratively with the full axisymmetric Navier-Stokes solution in the rest of the domain. Their simulations compare well with experimental results by Siegel *et al.* [92]. Singh *et al.* [68] studied the effect of sub-cooling and gravity on nucleate pool boiling.

Sato and Niceno [77] used VOF [51–53] to build a phase change model to study nucleate boiling. They employed a separate model using boundary layer theory to solve for the micro-layer. In an effort to simplify the film model proposed earlier, Sato *et al.* [78] incorporated the findings of Utaka *et al.* [87] to assume that the micro-layer is largely stagnant, and that its initial thickness is linearly proportional to the radial distance from the center-line. The constant of proportionality of the micro-layer profile was found by Utaka *et al.* [87] to be 4.46x10^{-3} for water, and 10.2x10^{-3} for ethanol at atmospheric pressure. They also studied the transition from discrete bubbles to the vapor mushroom regime [90]. The stagnant micro-layer model reduces the computational cost of simulating nucleate pool boiling significantly, enabling researchers to run $3D$ simulations.

For a comprehensive review of the advances in numerical modeling of boiling, we refer the reader to Kharangate and Mudawar [110]. While a substantial amount of progress has been made in simulating Nucleate pool boiling, in light of the recent developments in micro-layer modeling [78, 87] the key challenge is to find correlations between the micro-layer thickness and the bubble diameter for a generic fluid. So far, from literature [87] we only know the behavior of the micro-layers of ethanol and water. While the constant of 4.46x10^{-3} worked in the case of $T_{wall} = 109.5^oC$, it was found to be ineffective for the case of $T_{wall} = 106.3^oC$ in the work of Sato *et al.* [78]. Hence, it can be speculated that the constant of proportionality depends on the wall super-heat along with the fluid properties.

The initial stages of flow boiling comprise of three regimes namely the nucleation, the sliding motion, and the lift-off. The sliding motion of bubbles have been shown to contribute up to 50% of the heat transfer [82]. Baltis *et al.* [83] found that during the sliding motion of bubbles in vertical flow boiling at a super-heat of 15^oC, the heat absorbed from the wall can be as high as 30% of the total heat absorbed by the bubble. Xu *et al.* [85] found that in vertical flow boiling, the bubbles begin to slide with lower velocities than the surrounding flow, and accelerate to velocities higher than the surrounding flow. Several studies have proposed correlations for the

bubble departure and lift-off diameters in flow boiling by relying on force-balance and experimental studies in literature [79–81]. While the studies in literature shed light on departure and lift-off characteristics there is a scarcity of literature investigating the mechanisms by which the sliding motion of a bubble affects heat transfer. There is also a lack of numerical simulations of sliding bubbles in literature that account for the micro-layer.

In the present study we develop a simple stagnant micro-layer model for a generic fluid along the lines of Utaka *et al.* [87], that uses the findings of Cooper *et al.* [91]. We use the model to then study the heat transfer of sliding bubbles in a shear flow.

7.2 Numerical method

We divide the computational domain into two sub-domains namely one comprising of the micro-layer region, and one comprising the rest of the domain. We refer to the latter as the macro-region, and the former to as the micro-region. We use the numerical method outlined in chapter 5 for the macro-region. For the micro-region we develop a special treatment that involves solving for the mass transfer and energy transfer equations in the micro-layer. Son *et al.* [67] used the Level-set method coupled with a $1-D$ axisymmetric micro-layer model. Sato *et al.* [78] proposed a simpler model for the micro-layer. They used the initial micro-layer from the empirical findings of Utaka *et al.* [87], and assumed the film to be stagnant. They justified the stagnant micro-layer assumption by computing the local Peclet number which was found to be less than 1, suggesting that the dominant mode of energy transport is diffusion and not convection. Utaka *et al.* [87] found the initial film thickness to depend linearly on the distance from the nucleation site. They determined the initial film thickness to be $\delta_0 = 4.45\text{x}10^{-3}r$ for water, and $\delta_0 = 10.2\text{x}10^{-3}r$ for ethanol, and found the initial film thickness to be independent of the heat flux. However, Utaka *et al.*do not discuss the dependence of the initial film thickness on the wall superheat, and most of their cases correspond to a wall superheat in the neighborhood of 20^oC for water.

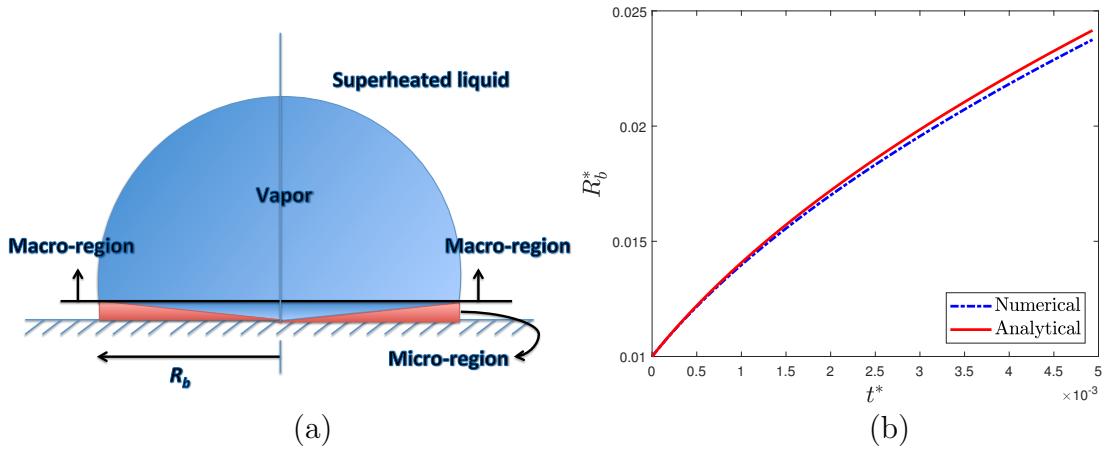

Figure 7.1. (a)Schematic of the $1-D$ nucleation model. (b) $1-D$ model without the micro-layer successfully simulates the growth of a water bubble in a superheated liquid at 104^oC.

Sato *et al.* [78] found that while the constant of proportionality $C = 4.45\text{x}10^{-3}$ works well for a superheat of 9.5^oC, it is not as effective for a superheat of 6.3^oC.

In the present section, we use a simplified $1-D$ model to predict the initial micro-layer thickness as function of the radial distance from the nucleation point. Cooper *et al.* [91] carried out an experimental study on the micro-layer thickness and developed a hydrodynamic model to arrive at equation 7.1 relating the initial micro-layer thickness at a given point and the time t_g taken by the micro-layer to reach the point. They also found the bubble to remain hemispherical in shape during the initial stages of bubble nucleation. We consider a bubble during the earlier stages of nucleation. In our analysis, we use the following assumptions:

a) The region of fluid surrounding the macro-region of the bubble is at an uniform temperature equal to that of the wall.

b) The bubble remains hemispherical in shape.

c) The wall temperature is constant.

d) The wall effect is not experienced by flow in the macro-region, i.e., the bubble

growth in the macro-region is governed by the simple $1-D$ energy transport equation in spherical coordinates.

e) The liquid in the micro-layer is assumed to be stagnant.

f) The temperature inside the bubble is equal to the saturation temperature.

$$\delta_0 = 0.8\sqrt{\nu t_g}. \tag{7.1}$$

$$\dot{V} = \dot{V}_{micro} + \dot{V}_{macro}. \tag{7.2}$$

$$\dot{V}_{micro} = \int_0^{R_b} 2\pi r u_g dr. \tag{7.3}$$

$$u_g = \frac{k_l \Delta T_{sup}}{\rho_v \delta(r) L}. \tag{7.4}$$

$$-\frac{d\delta}{dt} = \frac{k_l \Delta T_{sup}}{\rho_l L \delta}. \tag{7.5}$$

$$\dot{V}_{macro} = \frac{2\pi R_b^2 k_l}{\rho_v L}\left(\frac{\partial T}{\partial r}\right)_{R_b}. \tag{7.6}$$

$$\frac{dR_b}{dt} = \frac{\dot{V}}{2\pi R_b^2}. \tag{7.7}$$

From the above stated assumptions, it follows that the net rate of growth of the bubble is a sum of the rate of growth from the micro and macro-regions as shown in Equation 7.2. The rate of volumetric increase in the bubble due to the micro-layer is given by Equation 7.3. u_g is the velocity of the vapor above the micro-layer, and is derived by a simple energy balance as shown in Equation 7.4. The rate of volumetric change due to the macro-region is governed by the heat-flux on the liquid side as shown in Equation 7.6. The net rate of change in bubble radius is given by equation 7.7. Since the bubble is assumed to be hemispherical, the micro-layer ends at $r = R_b$. We solve equations 7.2-7.7 numerically, along with the $1-D$ energy transfer equation

in the macro-region given by Equation 7.8. From continuity in the macro-region, we have Equation 7.9, where u_r is the radial velocity in the liquid.

$$\frac{\partial T}{\partial t} + u_r \frac{\partial T}{\partial r} = \frac{\alpha}{r^2} \frac{\partial}{\partial r} \left(r^2 \frac{\partial T}{\partial r} \right). \tag{7.8}$$

$$u_r r^2 = R_b^2 \frac{dR_b}{dt}. \tag{7.9}$$

$$\delta(R_b, t) = 0.8\sqrt{\nu t}. \tag{7.10}$$

In solving the above mentioned equations numerically, we use the following approach at each time-step:

a) First, solve Equation 7.8 to obtain $T(r)$.

b) Find $\dot{V}_{macro}$ using Equation 7.6.

c) Compute $\dot{V}_{micro}$ using Equations 7.3 and 7.4.

d) Update $\delta(r)$ using Equation 7.5. Set the lower limit on δ to be $10^{-12}m$ to avoid numerical difficulties.

e) Update the value of R_b using Equation 7.7.

f) Update $\delta(R_b)$ using Equation 7.10.

We use a simple Explicit-Euler method to march in time, and all the spatial derivatives are computed to be second order accurate. The initial radius of the bubble was chosen to be $R_0 = 10^{-7}m$, which was sufficiently small as to not affect the steady state results discussed. The initial temperature field in the macro-region was chosen to be the analytical temperature distribution for the case of bubble growth in a superheated liquid at $R = R_0$.

If the contribution of the micro-layer is switched off in the above described model, the result should be the same as the growth of a vapor bubble in a superheated liquid described in Subsection **??**. We see in Figure 7.1(b) that for a superheat of $\Delta T_{sup} = 4K$, the model shows up to 97% agreement with the analytical solution for the chosen grid size. Shown in Figure 7.1(a) is a schematic of the macro and

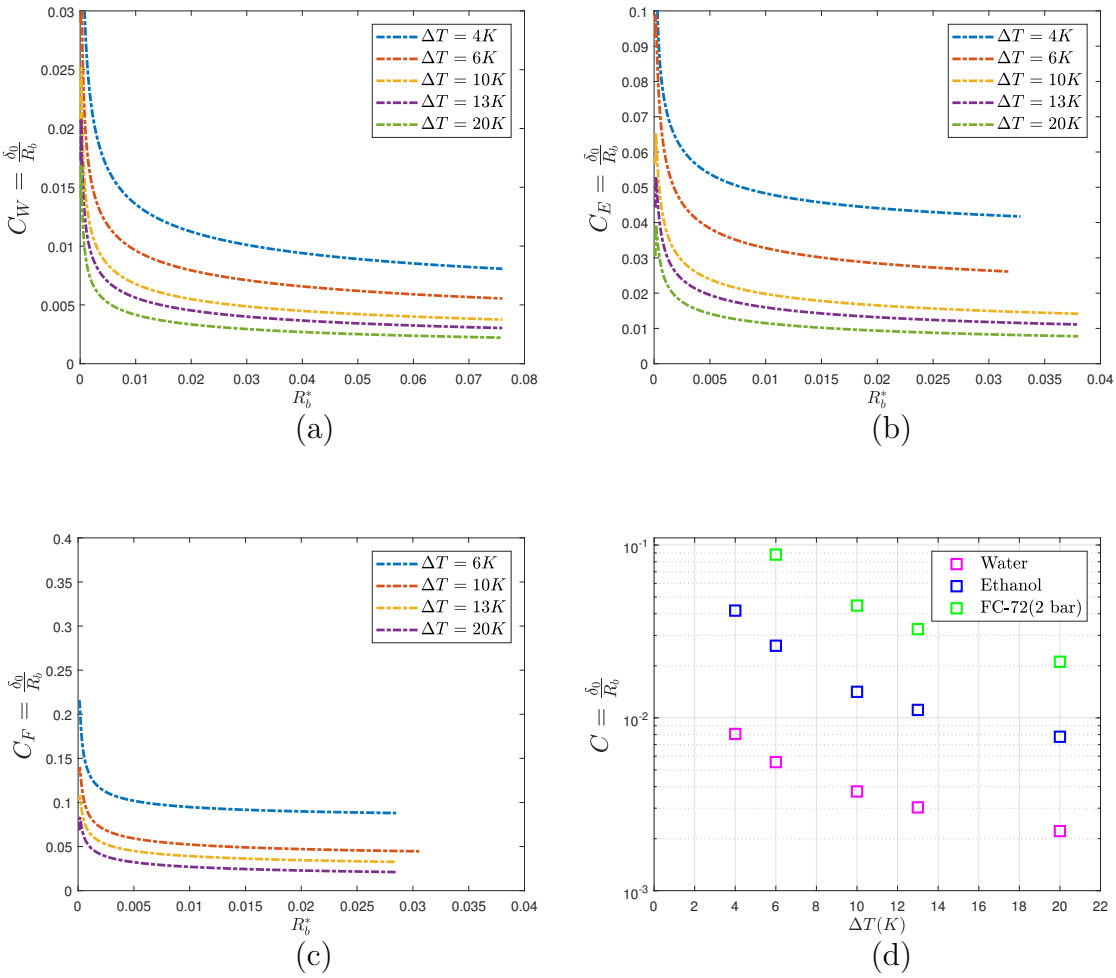

Figure 7.2. Asymptotic trend observed in C for various superheats for (a) Water, (b) Ethanol, and (c) FC-72 at 2 bar pressure. (d) Comparison between steady state C_W, C_E, and C_F at various superheats.

micro-regions in the model. We run five different cases each for water and ethanol corresponding to superheats $4K$, $6K$, $10K$, $13K$, and $20K$, and four cases for FC-72 corresponding to superheats $6K$, $10K$, $13K$, and $20K$.

From our simulation results, we see that $\frac{\delta_0}{R_b}$ shows an asymptotic trend at different superheats and working fluids as illustrated in Figures 7.2(a)-(c) for water, ethanol, and FC-72 at 2 bar. When the steady state value of $C = \frac{\delta_0}{R_b}$ is plotted for each case

against the superheat, we see a decreasing trend as illustrated in Figure 7.2(d). It is to be noted that the plot shows a plateau towards the higher superheats for all the three fluids. This is possibly why Utaka *et al.* [87] did not observe a significant variation of C with the wall superheat, given that most of their cases correspond to superheats close to $20K$ for water. The mean values of C that we obtained across the five superheats for water and ethanol are $\overline{C}_W = 4.5\text{x}10^{-3}$, and $\overline{C}_E = 20.1\text{x}10^{-3}$, respectively. While $\overline{C}_W$ is consistent with the findings of Utaka *et al.*, $\overline{C}_E$ deviates appreciably from their prediction of $10.2\text{x}10^{-3}$. Although they mention the heat flux for their experiment, it is unclear as to what superheat was used for the case of ethanol. We obtained $\overline{C}_F$ to be $46.6\text{x}10^{-3}$.

Since we wish to determine the dependence of C on the superheat temperature, we examine the two different length scales that affect C:

$$R \sim \beta_g \sqrt{\frac{k_l}{C_l \rho_l} t}. \tag{7.11}$$

$$\delta \sim \sqrt{\nu t}. \tag{7.12}$$

Equations 7.11 and 7.12 are derived using Equations 5.20 and 7.1 respectively. Hence the ratio of the mentioned length scales would scale as:

$$C = \frac{\delta}{R} \sim \frac{\sqrt{Pr}}{\beta_g}. \tag{7.13}$$

Pr being the Prandtl number and β_g implicitly carries information about the superheat according to Equation 5.21. Shown in Figure 7.3 is a plot of C against $\frac{\sqrt{Pr}}{\beta_g}$ based on 14 data points gathered for the three different fluids across five different superheats. The constant of proportionality by linear-fit was found to be 0.12 implying that:

$$C = 0.12 \frac{\sqrt{Pr}}{\beta_g} \tag{7.14}$$

It is to be noted that while the proposed correlation is built upon several important assumptions, it provides a useful starting point for a trial and error based determination of C for a generic fluid.

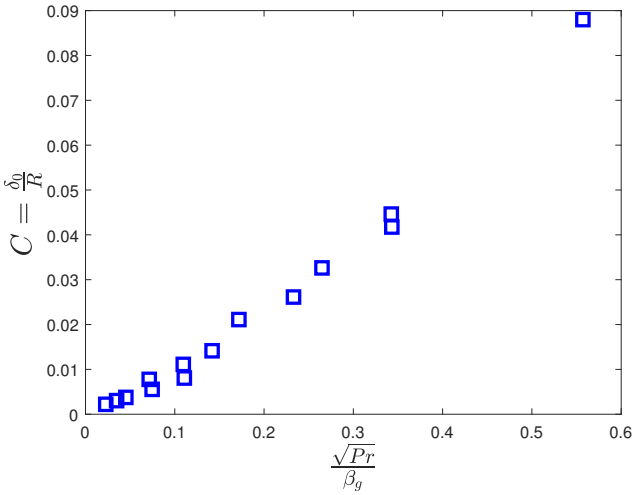

Figure 7.3. plot showing that $C \propto \frac{\sqrt{Pr}}{\beta_g}$.

7.2.1 Nucleate pool boiling: Comparison with Siegel *et al.* [92]

We use the above model to simulate the nucleation of a water bubble on a surface heated to 106.3^oC. We use the experimental data of Siegel *et al.* [92] to validate our simulations. We incorporate the stagnant micro-layer model into the front-tracking framework in the following way:

a) The initial shape of the bubble is assumed to be hemispherical, consistent with the experimental findings in literature [87, 91]. The bottom of the computational domain comprises of a layer of solid heating surface spanning 10 computational cells along the wall normal direction. These cells have zero velocity and zero convection. The last layer of solid cells have a Y-coordinate index jm.

b) We divide all front points and elements into two categories, namely the ones above the first node along the wall normal direction, and the ones that lie below it. The latter points are used to compute the micro-layer. We will refer to these front points

as 'micro-layer points' hereafter. Whenever a front point becomes a micro-layer point, we assign it its initial micro-layer thickness as:

$$\delta_{p,0} = C.r_0, \tag{7.15}$$

where C is determined from equation 7.14, and r_0 is the radial distance of the new micro-layer point from the axis of the bubble.

c) The micro-layer points will store the information about their local micro-layer thickness, and will dynamically update their micro-layer thickness according to equation 7.16, which is solved using an explicit-Euler scheme shown in equation 7.17. $T_{w,p}$ being the wall temperature corresponding to the micro-layer point which is computed from a first-order extrapolation using the first and second layers of solid cells beneath the bubble. We impose a minimum allowable $\delta_p = 10^{-8}m$, to avoid numerical difficulties. The ratio of the molecular size of water to $\delta_{p,min}$ is equal to 0.03, and is above the Knudsen number criterion for continuum mechanics to hold.

$$\frac{\partial \delta_p}{\partial t} = -\frac{k_f \left(T_w - T_{sat}\right)}{\delta_p \rho_f L_v}. \tag{7.16}$$

$$\frac{\delta_p^{n+1} - \delta_p^n}{\Delta t} = -\frac{k_f \left(T_{w,p}^n - T_{sat}\right)}{\delta_p^n \rho_f L_v}, \tag{7.17}$$

where, $T_{w,p}$ is interpolated from the fixed grid to the front.

$$\delta_p^{n+1} = max\{\delta_p^{n+1}, 10^{-8}m\}. \tag{7.18}$$

$$\dot{m} = \rho_f \frac{\left(\delta_p^n - \delta_p^{n+1}\right)}{\Delta t}. \tag{7.19}$$

$$\dot{Q}_{ml} = -\dot{M}_{ml} L_v \tag{7.20}$$

d) After computing $\dot{m}$ for the micro-layer points, we plug it into equations 5.12 and 5.13.This results in the mass transfer from the micro-layer to the gas phase inside

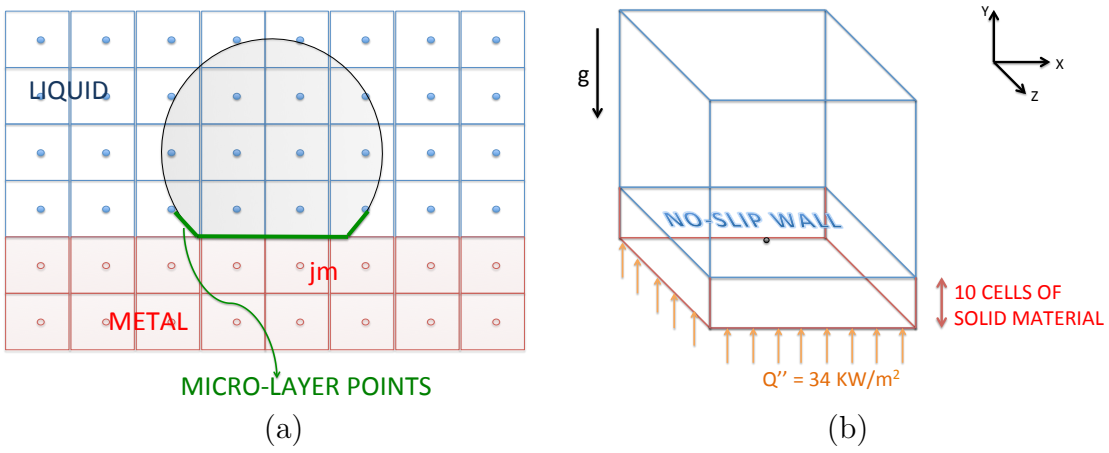

Figure 7.4. (a) Schematic showing the micro-layer points and the solid-liquid interface. (b) Schematic of the computational domain for nucleate pool boiling.

the bubble. We find $\dot{M}_{ml}$ using equation 5.12. With $\dot{M}_{ml}$, we compute $\dot{Q}_{ml}$ using equation 7.20. The smoothing of $\dot{Q}_{ml}$ is biased towards the heating surface side.

e) For a cell with indexes (i, jm, k), if the micro-layer is wet, i.e., $\delta > 10^{-8}m$, we impose T_{sat} as the boundary condition at the bottom face of the gas cell with indexes $(j, jm+1, k)$. The solid cells with indexes (j, jm, k) have a heat source $\dot{Q}_{ml}$.

f) On the other hand, if the micro-layer is dry, i.e., $\delta = 10^{-8}m$ for the mentioned cell, we treat cells (j, jm, k) and $(j, jm+1, k)$ as having the mean of their temperatures at their shared face. This signifies that the gas phase is in contact with the solid.

With the above described method in mind, we simulate a case of Nucleate boiling of a water bubble on a silicon substrate heated to a temperature of 106.3^oC. The values of properties used for the silicon heating substrate, water, and water-vapor are shown in table 7.1. The initial condition for the temperature profile was a thermal boundary layer of thickness δ_T dictated by Kays and Crawford [88] in equation 7.21.

$$\delta_T = 7.14 \left[\frac{\nu\alpha}{g\beta\Delta T} \right]^{1/3}. \tag{7.21}$$

Table 7.1.
List of material properties used in the present study

Material	ρ (Kg/m^3)	μ $(Pa.s)$	C_p (J/KgK)	k (W/mK)
Silicon	2330	–	766	148
Copper	8960	–	385	401
Water	959	$2.8\text{x}10^{-4}$	$4.2\text{x}10^{3}$	0.68
Vapor	0.59	$1\text{x}10^{-5}$	$3.3\text{x}10^{3}$	0.02

The initial temperature in the solid is set to 106.3^oC. Figure 7.2.1(b) shows a schematic of the computational domain used. The fluid region begins after ten layers of solid cells where a no-slip boundary condition is applied. All other faces of the computational domain have a zero normal velocity gradient along with a constant uniform pressure condition. We impose a heat-flux boundary condition at the bottom of the solid substrate $Q'' = 34\ kW/m^2$. The bubble nucleation site is located at the center of the XZ plane. For our numerical method to work, we need at least four computational cells across the bubble diameter, since a second order interpolation is used to compute thermal gradients across the interface. To be safe, we assume the initial bubble diameter to be six times the grid spacing. The Length of the computational domain is set to $L_x = L_y = L_z = 4mm$.

Plugging the properties of water and a superheat of 6.3^oC into equation 7.14 gives us $C = 8.5\text{x}10^{-3}$. We run the simulation for three different grid configurations: 128x128x128, 140x140x140, and 200x200x200. Figure 7.7(a), (b), and (c) show temperature contours at times $0.2ms$, $6.55ms$, and $13.4ms$ respectively. The bubble departure time in the simulation is $t_d \approx 20.5ms$. The bubble departure diameter is computed as the diameter of a sphere with the same volume.

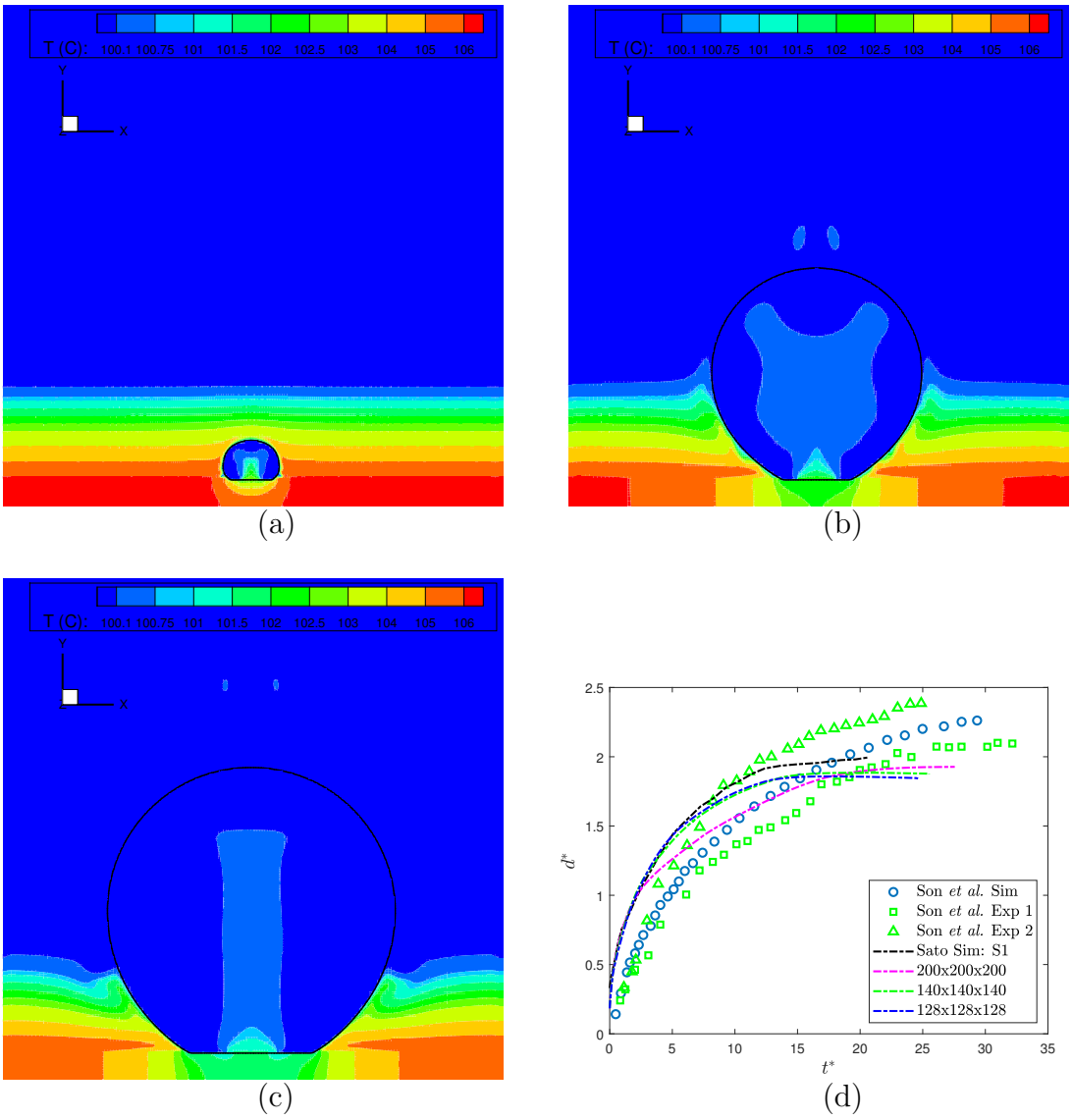

Figure 7.5. Snapshots of the simulation at times $t =$ (a)$0.2ms$, (b)$6.55ms$, (c)$13.4ms$. (d) Comparison of d^* the non-dimensional diameter of the bubble.

We use the experimental data of Siegel *et al.* [92] and the numerical data of Son *et al.* [67] for our validation. Figure 7.7(d) shows the plots of the non-dimensional diameter and of the bubble against non-dimensional time. Figures 7.7(d) indicates that the results of all the three grid configurations discussed compare well with the

experimental data of Siegel *et al.* [92] and the numerical data of Sato *et al.* [78]. For all future simulations we use a grid size corresponding to the 128x128x128 case.

7.3 Flow boiling: Problem setup and objectives

We consider six different shear rates: $\dot{\gamma} = 23.8\ s^{-1}$, $71.4\ s^{-1}$, $119\ s^{-1}$, $143\ s^{-1}$, and $167\ s^{-1}$. We are interested in the nucleation, sliding, and lift-off motion of a line of bubbles along the flow under the mentioned shear rates. The problem setup comprises of line of bubbles growing out of cavities with a fixed spacing between them on a wall at a temperature of 106.3^oC. We use two different values of spacing between the cavities in the present study: $s = 2.5\ mm$ and $s = 5.0\ mm$. The characteristic length scale for this problem L_C is defined as:

$$L_C = \sqrt{\frac{\sigma}{\rho g}}. \tag{7.22}$$

For our simulations with water as the working fluid $L_C = 2.5\ mm$. Using L_C we can normalize the shear rate $\dot{\gamma}$ as:

$$Re_b = \frac{\rho \dot{\gamma} L_C^2}{\mu} = \frac{\dot{\gamma}\sigma}{\mu g}. \tag{7.23}$$

The computational domain used to simulate the problem is identical to that described for pool boiling except that the top Y face is given a shear boundary condition corresponding to the applied shear rate. In order to simulate an infinite line of bubbles we use the periodic boundary condition along the flow direction. The length of the computational domain is equal to the spacing between the bubble cavities under the period boundary condition, and the cavities at the center of along the X direction. The Z faces have a constant uniform pressure along with a zero normal velocity gradient boundary condition. The wall material is silicon having thermal properties enlisted in table 7.1, and spanning the first ten cells along the wall normal direction. At the bottom of our computational domain we supply a constant heat flux of $Q'' = 40\ kW/m^2$. A schematic of the computational domain is provided in figure 7.3. We use a zero normal temperature gradient boundary condition at the Z

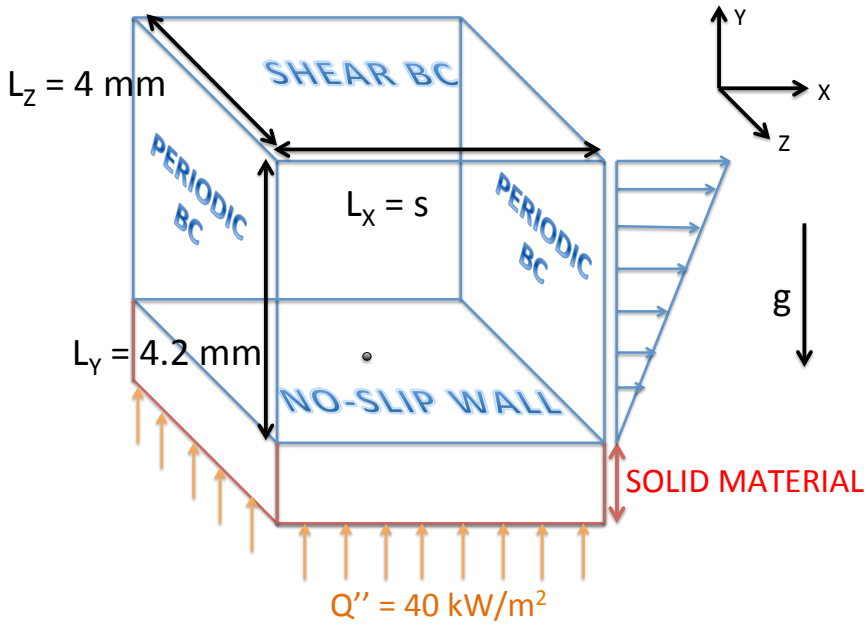

Figure 7.6. Schematic of the computational domain used for the flow boiling simulations. s is allowed to be 2.5 mm and 5 mm.

faces and the top Y face of the computational domain. The initial condition for the momentum equations is a linear u velocity profile with slope equal to the imposed shear rate. The temperature everywhere is initialized to 100^oC and the bubble is initialized at the cavity when the temperature of the cavity reaches $T_{wall} = 106.3^oC$. The X, Y, and Z lengths of the computational domain are s, 4.2 mm, and 4 mm, respectively. We run two sets of simulations corresponding to $s = 2.5$ mm and 5 mm. We use 256x128x192 grid points along X, Y, and Z directions for the case of $s = 5$ mm, and 128x128x192 grid points for $s = 2.5$ mm. This configuration results in a grid size

All the simulations are run in a frame of reference fixed to the bubble. This is achieved by subtracting from the overall velocity field the velocity of at each time-step. The boundary conditions have to be changed in the same manner. Since we have a layer

of solid cells in the computational domain, we have to additionally account for the convection of energy with the bottom wall velocity while solving the problem in a moving frame of reference. We refer the reader to our previous work [86] for a better understanding of the moving frame method. The grid size used in the mentioned configuration is smaller than the 128x128x128 case used in the pool boiling simulation for the same temperature. We use uniformly spaced grids in all the simulations.

We are interested in examining the total distance moved by the bubble as a function of time in the stationary frame of reference, the total heat transfer to the wall from the micro-layer, and the temperature of the wall as a function of time. Since we are interested in the transient heat transfer and bubble sliding characteristics the steady-state behavior of this system is out of the scope of the present study. We define the wall-averaged heat transfer coefficient using the applied heat flux, wall temperature recorded at the nucleation surface, and the saturation temperature as follows:

$$h = \int_0^{L_X} \int_0^{L_Z} \frac{Q''}{T_{wall}(x,z) - T_{sat}} dxdz. \tag{7.24}$$

To quantify the improvement in heat transfer coefficient compared to single phase flow we use the ratio of the two heat transfer coefficients:

$$h^* = \frac{h}{h_s}, \tag{7.25}$$

where h_s is the single phase heat transfer coefficient. We are also interested in the evolution of the rate of heat extracted from the wall by the micro-layer $\dot{Q}_{ml}$, and the ratio between the heat that the bubble extracts through micro-layer evaporation and the total heat absorbed by the bubble. The key difference between the two sets of spacing $s = 2.5\ mm$ and $5\ mm$ is that in the former case the interaction between adjacent bubbles can be expected to be more pronounced and influential in determining the lift-off characteristics. One of the cases that we present for the $s = 5$ mm is with an inclined wall at an angle of 15^o.

Table 7.2.
Cases simulated in the present study

Case	Spacing (mm)	Re_b	Inclination
1	2.5	507	–
2	2.5	2533	–
3	2.5	3039	–
4	2.5	3546	–
5	5.0	507	–
6	5.0	1520	–
7	5.0	2533	15^o
8	5.0	2533	–

7.4 Results and discussion

All the cases simulated are shown in table 7.2. We first present the transient characteristics of case 8. Figure 7.4(a) shows the motion of the bubble with time. We see that the bubble is initially stationary up to 2 ms and then accelerates. We define the point at which the bubble begins to accelerate as the departure point and the time from $t = 2$ ms to 30 ms as the sliding phase. The bubble detaches from the wall at $t = 30$ ms, and we define this point to be the lift-off. We note that the motion of the bubble in the sliding phase is smoother compared to the departure phase. Figure 7.4 (b) shows the evolution of the mean temperature at the wall, compared to the single phase flow. We note that the wall temperature decreases by 1^oC over the bubble's residence period. We define ΔT as the difference between the two-phase flow wall temperature at a certain time and the single phase flow temperature at the same time.

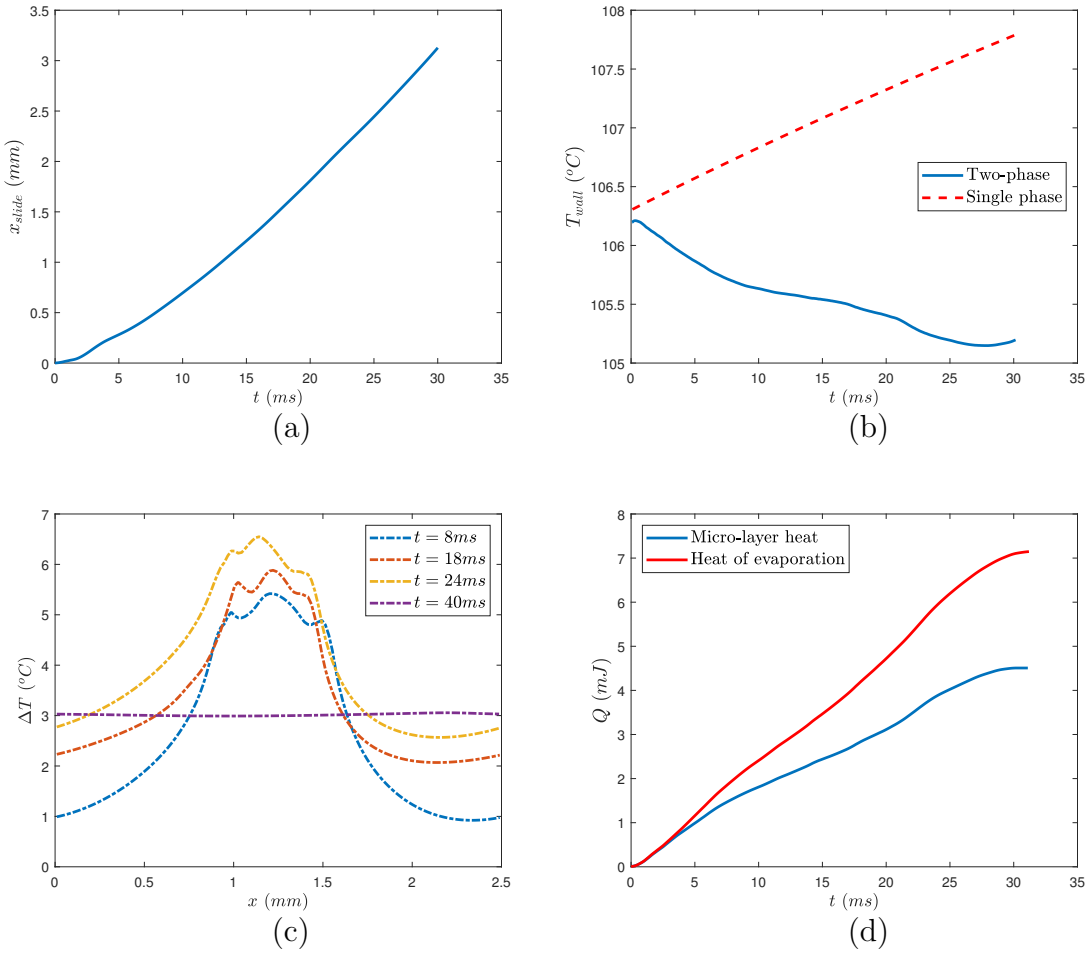

Figure 7.7. For $Re_b = 2533$, (a) Sliding distance as a function of time, (b) Average temperature at the wall compared to single phase flow, (c) Variation of the temperature along the center-line of the wall, and (d) Heat from the micro-layer compared to total heat.

Figure 7.4 (c) shows the difference between the temperature in the two-phase flow and single phase flow at different times. The temperature plot is along the center-line of the wall in the flow direction. Since the bubble lift-off occurs at 30 ms, we see that the temperature profile is nearly a straight line at 40 ms, and is 3^oC lower than the single phase flow temperature at that time. We also see that the improvement of the wall temperature with respect to single phase flow diffused along the center-line

with time. Figure 7.4 (d) shows the heat absorbed for the micro-layer evaporation as a function of time. The red plot shows the total heat absorbed by the bubble and is computed as

$$Q_{total} = (V_{bub,t} - V_{bub,0})\rho_g L_v. \tag{7.26}$$

We observe that in the micro-layer evaporation is the predominant mode of bubble growth in the initial stages until 4 ms. Beyond this point while the micro-layer still contributes significantly to the bubble growth, the convective heat transfer becomes increasingly important. We see that the micro-layer evaporation contributes 64% of the bubble growth over the total residence time of the bubble making it a critical phenomenon in predicting the heat transfer of a sliding bubble. Figures 7.4(a), (b), and (c) are snapshots of the simulation for case 8 at times $t = 4ms$, $t = 10ms$, and $t = 40ms$, respectively, showing the temperature contour in the flow and the solid region. Figure 7.4(d) is a $3D$ view of the simulation at $t = 18$ ms showing the temperature contour on the wall. Figure 7.4(e) shows the evolution of the bubble diameter as a function of time. We observe that there are two phases of the bubble growth. We see a distinct change in the slope of the diameter with time at around $t = 15$ ms. Beyond this point the diameter variation can be attributed to the sliding motion.

Figure 7.4 (a) and (b) show the variation of heat transfer coefficient improvement with respect to the single phase flow for $s = 5$ mm, and $s = 2.5$ mm, respectively. We observe an improvement of up to 20% for the case of $s = 5$ mm , and up to 60% for the case of $s = 2.5$ mm. The plots are show up to the lift-off time for each case of Re_b. A common observation in both cases is that the heat transfer coefficient ratio with single phase flow is similar for all Re_b up to a certain point in the simulation after which they all diverge. For both cases of s this point in the simulation is around $t = 6$ ms. For the case of $s = 2.5$ mm we see that the variation in time of the heat transfer coefficient is less smooth compared to $s = 5$ mm. The lift-off times for $s = 2.5$ mm are larger than for the case of $s = 5$ mm. For the same Re_b of 507 and 2533 we see that the lift-off time for the case of $s = 2.5$ mm is larger than $s = 5$ mm.

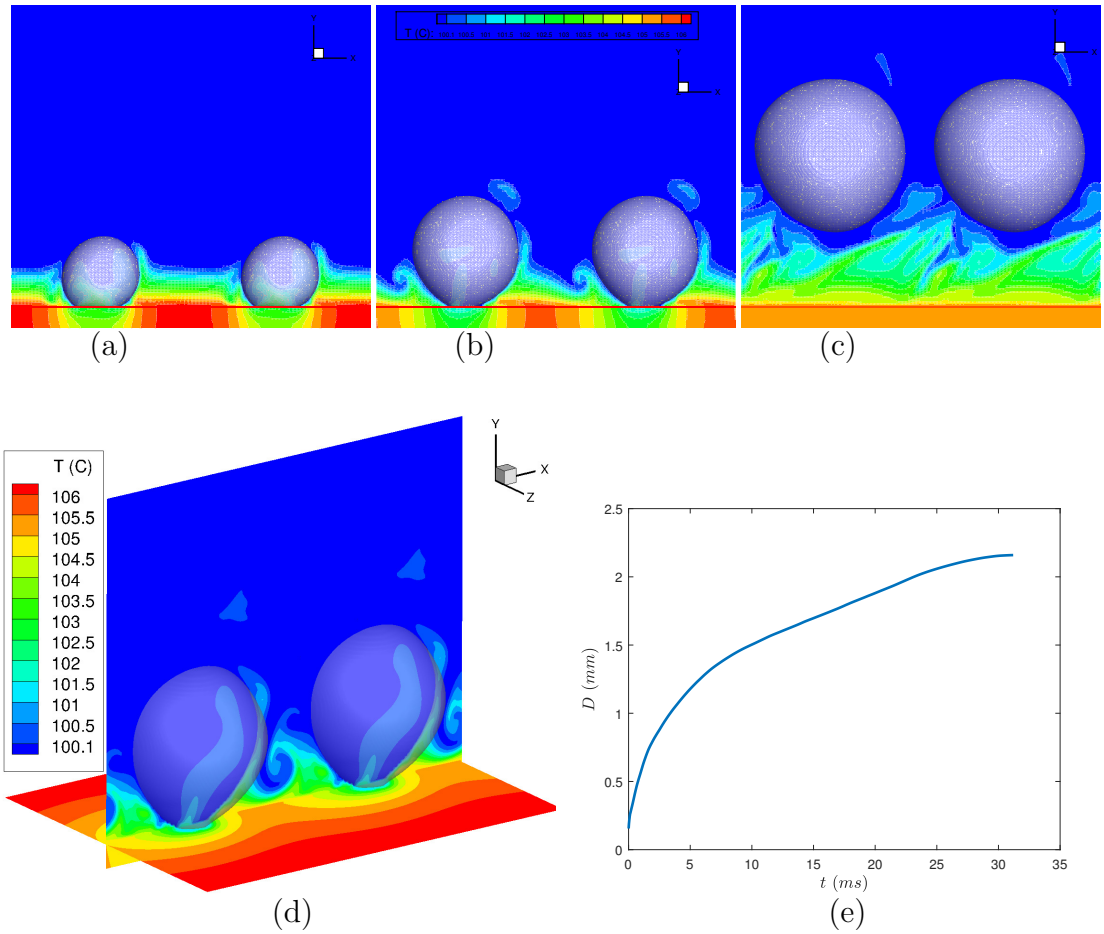

Figure 7.8. Snapshot of the simulation for $Re_b = 2533$ at (a) $t = 4ms$, (b) $t = 10ms$, (c)$t = 40ms$, (d)A $3D$ view of the simulation at $t = 18ms$, and (e)The evolution of the bubble diameter.

We note from cases 7 and 8 that an inclination of 15^o causes the bubble to lift-off sooner than in the horizontal case. Figure 7.4 (c) and (d) show the heat transfer from the solid surface to the bubble via micro-layer evaporation. Again we observe that the plots for all the Re_bs for a fixed s are similar until around $t = 5\ ms$ and then diverge. When Q_{mic} becomes flat, it signifies the bubble lift-off. We also observe that the trends of h/h_s and Q_{mic} are similar to one another showing the dominance of micro-layer evaporation in the overall heat transfer from the bubble. We can expect

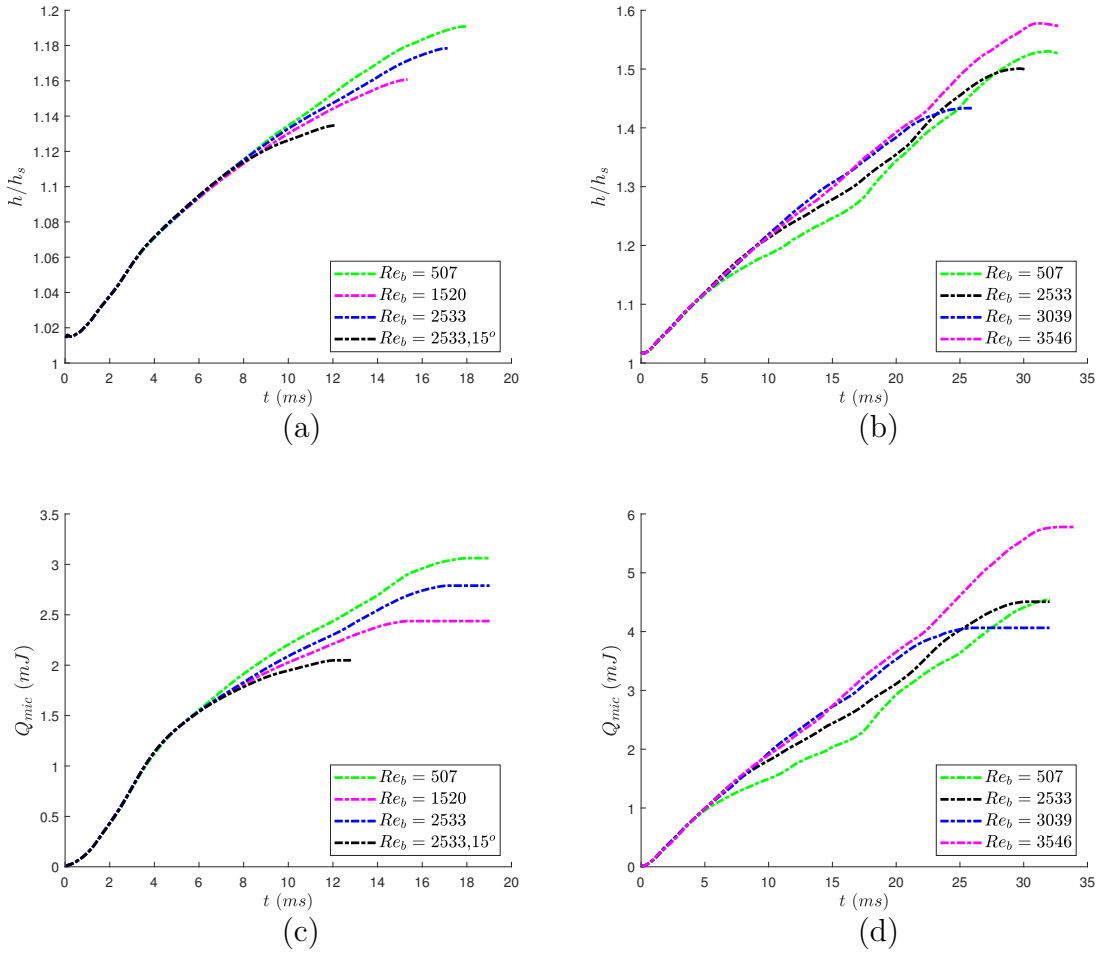

Figure 7.9. Heat transfer coefficient for (a) $s = 5\ mm$, (b) $s = 2.5\ mm$, heat transfer from the micro-layer evaporation for (c) $s = 5\ mm$, (d) $s = 2.5\ mm$ for different cases of Re_b, (e) Sliding distance as a function of time for $s = 5\ mm$, and (f) Sliding velocity for $s = 5\ mm$.

the interaction effect between adjacent bubbles to be stronger in the case of $s = 2.5$ mm than $s = 5\ mm$. From our simulations it is evident that for the same value of shear rate, a smaller inter-bubble spacing leads to a larger lift-off time.

Figure 7.4 (a) and (b) show the sliding distance and sliding velocity as a function of time, respectively. From figures 7.4 (a) and (b) we can split the bubble trajectory into two phase, the first one where the bubble moves with a low velocity, and the second

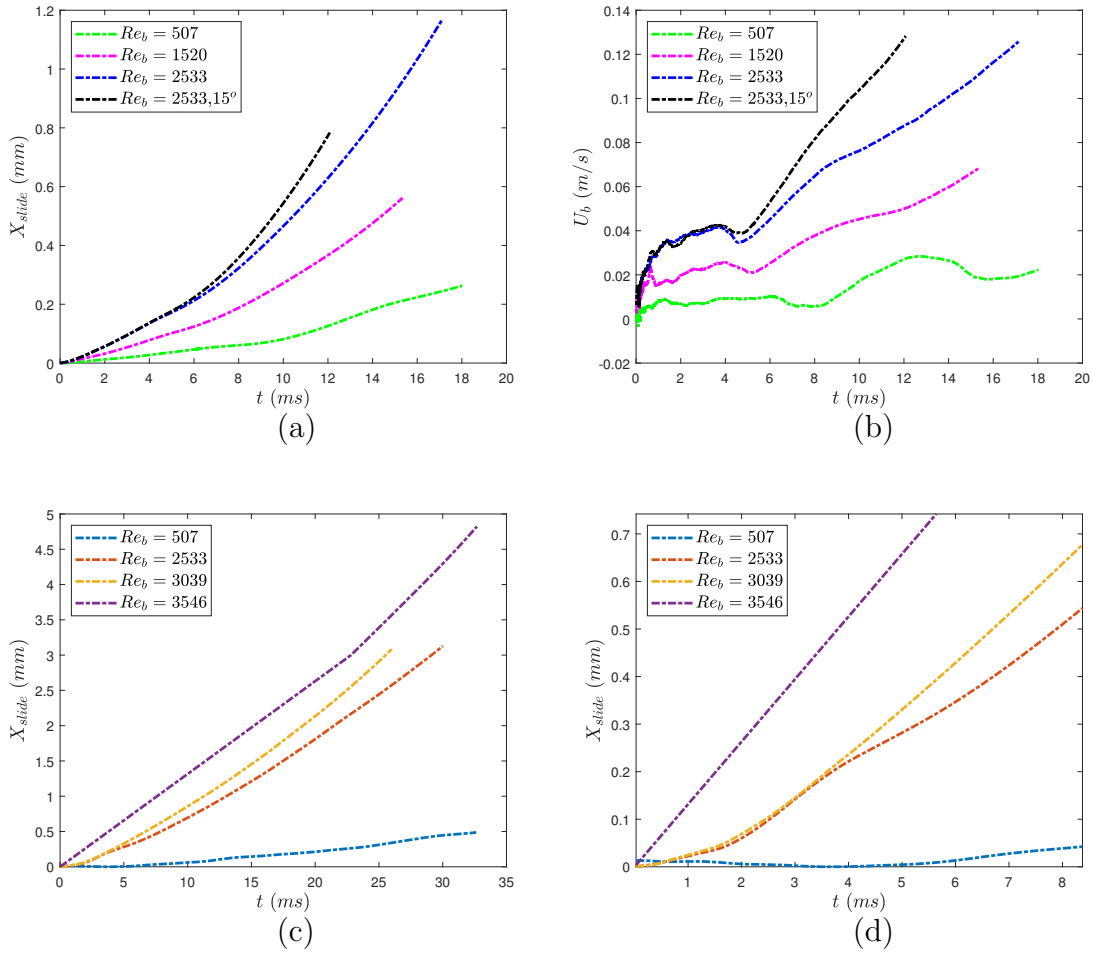

Figure 7.10. (a) Sliding distance as a function of time for $s = 5\ mm$, and (b) Sliding velocity for $s = 5\ mm$. (c) Sliding distance as a function of time for $s = 2.5\ mm$, and (d) Sliding distance for $s = 2.5\ mm$ zoomed in, showing the transition from the initial phase to the acceleration phase.

in which the bubble accelerates. We also observe that as the shear rate is increased the velocity of the bubble in each phase increases. The blue and black lines in figure 7.4 (a) corresponding to cases 7 and 8 indicate that the velocity of the bubble in the first phase is a function of the shear rate. We see from figure 7.4 (b) that the first phase has almost a constant velocity profile with time and the second phase involves bubble acceleration. A comparison between the velocities of cases 7 and 8 from figure

7.4 (b) shows that for the inclined case 7 the bubble experiences a higher acceleration along the X direction and also experiences lift-off earlier. The point at which the sliding trajectories of cases 7 and 8 deviate from one another is around $t = 6\ ms$. While the time at which the sliding motion transitions from the slow phase to the acceleration phase is seen to decrease with an increase in flow rate, the lift-off time has no clear correlation with the shear rate. Figure 7.4 (c) shows the sliding distance of the bubble for $s = 2.5\ mm$. We observe a much shorter initial phase compared to the cases of $s = 5\ mm$. Figure 7.4 (d) shows a zoomed-in view of figure 7.4 (c) showing the initial phase for the bubble. We see that the time at which the bubble transitions from the initial phase to the acceleration phase is at around $t = 3\ ms$. We see for case 4 corresponding to $Re_b = 3546$, the initial slow phase is non-existent and the bubble begins to accelerate as soon as the simulation begins. This case also has the longest sliding distance and the largest sliding time. Figure 7.4 (a) shows the percentage improvement in the heat transfer with respect to the single phase flow, as a function of the lift-off time Δt_l. We see that for both cases of s the percentage improvement in the heat transfer coefficient increases as a function of the lift-off time. In the range of shear rates simulated the linear fit for $s = 2.5mm$ and $s = 5mm$ are:

$$\frac{\Delta h}{h_s}(\%) = 0.52\Delta t_l + 2.4,$$

and

$$\frac{\Delta h}{h_s}(\%) = 0.7\Delta t_l + 7.5,$$

respectively. Basu *et al.* [84] used the data of sliding distances and diameters from literature and created a correlation between $D_L/[L_C Ja_{sup}^{0.45} e^{-0.0065 Ja_{sub}}]$ and the Sliding Reynolds number defined as:

$$Re_l = \frac{\rho u l}{\mu},$$

where u is the fluid flow velocity around the bubble and l is the sliding distance of the bubble. In the former parameter,

$$Ja_{sup} = \frac{\rho_l C_l (T_{wall} - T_{sat})}{\rho_v L_v},$$

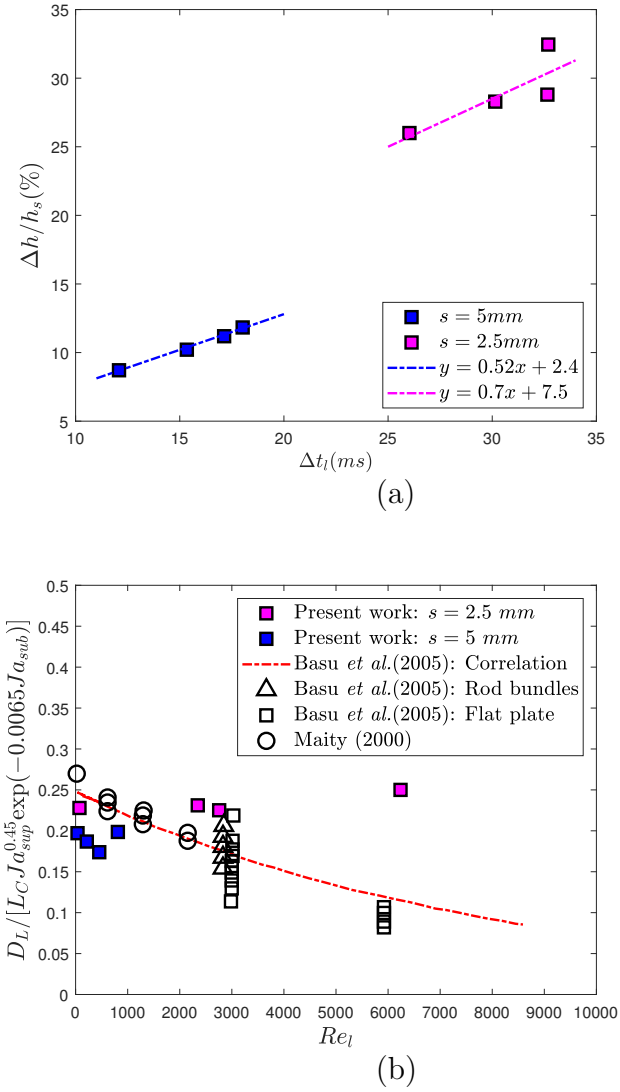

Figure 7.11. (a) Sliding distance as a function of time for $s = 5\ mm$, and (b) Sliding velocity for $s = 5\ mm$.

and L_C is defined by equation 7.22. Since all our simulations are under the saturated flow condition, $J_{sup} = 0$. For each case of Re_b we compute the mean time averaged fluid velocity experienced by the bubble as:

$$u = \frac{\int_0^{\Delta t_l} \int_0^{D_b(t)} \dot{\gamma} y dy dt}{\int_0^{\Delta t_l} D_b(t) dt}.$$

We can compute the Re_l by using u computed above and the sliding distance. With Re_l and the lift-off diameter D_L, we create a data point corresponding to each case in table 7.2. D_L is the bubble equivalent diameter measured at lift-off. The Ja_{sup} for all our simulations is 18.73. Figure 7.4 (b) is a plot of $D_L/[L_C Ja_{sup}^{0.45} e^{-0.0065 Ja_{sub}}]$ against Re_l showing the correlation of Basu *et al.* [84], their experimental findings, Maity's experimental findings, and the results from our simulations. Our values for the lift-off diameters are in agreement with the correlation shown in red except for case 4. It must be noted that the correlation proposed by Basu *et al.* [84] and the experiments performed by Maity were for the case of a single bubble. Hence, cases 5-8 in 7.2 can be expected to be in better agreement with their correlation compared to cases 1-4, since the bubbles are farther apart in the former than the latter.

7.5 Summary

In conclusion the front-tracking based numerical method was successfully validated using the bubble growth in super-heated liquid problem and the Stefan's problem. A stagnant micro-layer model was created for nucleate boiling simulations, and was validated by using data from an experimental study on pool boiling at 106.3^oC. The developed model was then used to study nucleate flow boiling of a line of bubbles under a shear flow. Two different values of bubble spacing and four different shear rates were simulated. Our simulations show that the micro-layer evaporation is an important mechanism by which the bubble enhances heat transfer at the wall forming up to 64% of the total heat absorbed by the bubble. The motion of the bubbles was seen to comprise of two-phase namely the initial low-velocity phase, and the acceleration phase with higher velocities. The initial low-velocity phase was seen to be dependent on the shear rate. The velocity of the bubble was seen to increase as the shear rate was increased. The improvement in the heat transfer coefficient with respect to single phase flow was seen to be as high as 32%. The improvement in the heat-transfer coefficient was seen to increase as the lift-off time increases. Finally

our results for the bubble lift-off diameter were seen to agree with the experimental findings and a correlation in literature.

8. CONCLUSION

Two-phase flow heat transfer is a fascinating field of research that presents challenging multi-physics problems for computational fluid dynamicists. Its abundance in industrial applications further necessitates research in the field of multiphase computational fluid dynamics. The goal of the present work was to develop an effective numerical tool that can then be used to further the understanding of the physics of two-phase heat transfer.

The applications and importance of two-phase flow heat transfer were introduced in chapter 1. The importance of two-phase flows in heat removal from high heat flux devices is explained along with other traditional applications of bubbly flows. The strategy adopted to understand bubbly flow heat transfer was to first gain an understanding of the fluid dynamics of a layer of bubbles rising near a vertical wall; then to look at the heat transfer associated with non-condensable bubbles, and finally to examine the heat transfer associated with phase change in bubbly flows. Chapter 3 presented results of the direct numerical simulations of a layer of bubbles rising near a vertical wall, a situation commonly encountered in the industry. Scaling laws relating the bubble rise velocity, the viscous dissipation and the steady-state film thickness to the archimedes number were derived. Chapter 4 examined the flow patterns around a rising bubble near a vertical wall, and linked it to the wall-to-liquid heat transfer. The heat transfer improvement with respect to a single phase flow was found to depend directly on the reversal streamlines around the bubble. An optimal shear was found to exist for a given archimedes number that maximizes the heat transfer at the wall. Chapter 5 presented a numerical method to simulate boiling and condensation that was validated with experimental data and benchmark problems. This method was in chapter 6 used to study the heat transfer characteristics, bubble size distribution, and the bubble injection frequency in a micro-channel undergoing sub-cooled flow boiling.

The bubble size distribution was to become flatter and the frequency was found to increase as the inlet flow rate was increased. Having a hot-spot at the nucleation site was found to increase the bubble injection frequency and the flatten the bubble size distribution along the micro-channel. Chapter 7 improved the numerical method to include a stagnant micro-layer model which was validated using an experimental study. The micro-layer model was then used to study the boiling of a line of bubbles in various shear flows. Two distinct phases of the bubble evolution, namely, the rapid growth phase and the bubble sliding phase, were found to exist. The heat transfer improvement was found to be strongly dependent on the bubble lift-off time. The results of the simulation were then compared with existing correlations and experimental studies to find a good match between the two.

In conclusion, the present work sheds light on the fluid flow characteristics around bubbles, the mechanism by which non-condensible bubbles affect heat transfer, and presents a robust numerical tool to simulate boiling and condensation problems in bubbly flows. It demonstrates the power of computational fluid dynamics as a tool to carry out future studies that will enable the optimal design of thermal systems involving two-phase flows. It presents flow boiling as a potent means to remove high heat fluxes, and provides a useful micro-layer model in nucleate boiling. The proposed model is a good starting point to run future simulations of flow boiling where the micro-layer effects need to be modeled.

9. FUTURE WORK

We can broadly divide the future work into two categories namely development of the numerical method, and investigation of new physics or flow situations.

9.1 The numerical framework

9.1.1 Micro-layer modeling

Although the micro-layer model described in section 7.2 of chapter 7 is generic enough to account for differences properties of the working fluid, it can be improved in the following ways:

a) The stagnant micro-layer model does not account for the effect of varying the heat flux on the heating surface, or take into account the lateral conduction that occurs in the heating surface as the bubble expansion takes place. The model in section 7.2 is built upon the assumption that the heating surface is at a constant super-heated temperature. In the future one would like to expand the analysis in section 7.2 to include the lateral conduction and the wall heat effects.

b) The micro-layer is assumed to be stagnant. Sato *et al.* [78] justified this assumption by using the Peclet number in the micro-layer. As we move closer to the edge of the micro-layer, we know that this assumption is more likely to be violated. Hence, While one doesn't need the level of complexity that Son *et al.* [67] used in their analysis, one could solve the simplified navier-stokes equations in the micro-layer.

9.1.2 Contact angle

Whenever there are three phases coming into contact, such as in the case of nucleate boiling, there is a contact angle made by the gas-liquid interface with respect to the

solid surface. This contact angle is a function of the adhesive and cohesive forces between the three phases. The Implementation of the contact angle is achieved in the Level-set method by using a Neumann boundary condition for the distance function [74]. In the front-tracking method, implementation of the contact angle is more challenging. In the present work, since we don't have a model to solve for the contact line, we simply use a no-slip boundary condition wherever the front is found to touch the wall. This results in a contact angle that is largely dependent on the dynamic effects of the flow field around the bubble. But when the bubble is stationary, we wish to implement a static contact angle that is a function of the chemical properties of the gas, liquid and the solid wall. In the front-tracking framework, the contact angle will have to be implemented by applying a force along the desired angle at front elements that are in contact with the wall. Since the effect of surface wettability on flow boiling is an active field of research, the implementation of static contact angle boundary condition as an important future task.

9.1.3 Topology change: Coalescence and break-up

The transition from bubbly flow to slug flow is often caused by coalescence of small bubbles. Similarly, when dealing with annular flows or churn flows, we see the phenomenon of break up. A major disadvantage of the front-tracking method employed in the present study is its difficulty in accommodating topological change. Front information is stored in the form of data structures, with information connecting each node to other neighboring nodes and each elements to its neighboring elements, and a break-up or coalescence between two bubbles would involve coming up with efficient and effective algorithms to make changes to these data structures. Having said that, topological change has been implemented in front-tracking by a studies such as Shin *et al.* [95].

Level-set on the other hand has the advantage that any two interfaces that approach each other within 1 cell size would result in coalescence automatically. Level-set is

also attractive in terms of its ease of implementation. So, as a future work, we aim to integrate front-tracking and level-set. We aim to implement a numerical method where nucleation and growth of the bubble is simulated using front-tracking, and after departure, we switch to level-set, so that many such individual bubbles can coalesce at that stage. The switch from front-tracking to level-set is can be achieved by using the color function field generated at each time-step in the front tracking method. A level-set reinitialization applied to the color function would convert it into the distance function.

9.2 Challenges: Hot-spots, Flow reversal, Pressure fluctuations

Hot-spots are likely to be an area of focus in the field of micro-channel heat sinks in the future. The hot spots could contain heat fluxes as high as six times the average heat flux and could often cause thermal failure. Recently there has been a focus in the heat transfer community to address this problem [112]. While chapter 6 presented an analysis on the impact of a hot-spot on the micro-channel heat transfer characteristics, more work could be done in the future on hot-spot mitigation strategies. Flow reversal is a commonly faced problem when micro-channels are stacked in parallel [111]. The problem is aggravated by non-uniform heating in the micro-channel heat sink. Pressure fluctuations could arise in the micro-channel due to abrupt evaporation. Hence, it would be of interest to study the dynamics between parallel micro-channels under the effect of non-uniform heating.

REFERENCES

REFERENCES

[1] D. J. Chamund, L. Coulbeck, D. R. Newcombe and P. R. Waind. High power density ICBT module for high reliability applications. *IEEE 6th Int. Power Electronics and motion control conference, 17-20 May 2009, China*, 2009.

[2] C. Bachmann and A. Bar-Cohen. Hotspot remediation with anisotropic thermal interface materials. *11th IEEE conference on thermal and thermomechanical phenomena in Electronic systems, 28-31 May 2008, Orlando, FL, USA* 2008.

[3] E. A. Silk, E. L. Golliher and R. P. Selvam. Spray cooling heat transfer: technology overview and assessment of future challenges for micro-gravity application. *Energy Convers. Manage.*, 49 (3)(2008) 453-468.

[4] T. G. Karayiannis and M. M. Mahmoud. Flow boiling in microchannels: Fundamentals and applications. *Applied Thermal Engineering*, 115 (2017) 1372–1397.

[5] A. T. Tokuhiro and P. S. Lykoudis. Natural convection heat transfer from a vertical plate-I. Enhancement with gas injection flows. *Int. J. Heat Mass Transfer*, 37:997–1003, 1994.

[6] M. Tamari and K. Nishikawa. The stirring effect of bubbles upon heat transfer to liquids. *Heat Transfer - Japanese Research*, 5(2):31–44, 1976.

[7] A. Kitigawa, K. Uchida, and Y. Hagiwara Effects of bubble size on heat transfer enhancement by sub-millimeter bubbles for laminar natural convection along a vertical plate. *Int. J. Heat and Fluid Flow*, 30:778–788, 2009.

[8] A. Kitagawa, K. Kosuge, K. Uchida, and Y. Hagiwara Heat transfer enhancement for laminar natural convection along a vertical plate due to sub-millimeter-bubble injection. *Exp. Fluids*, 45:473–484, 2008.

[9] A. Kitagawa, K. Kitada, and Y. Hagiwara Experimental study on turbulent natural convection heat transfer in water with sub-millimeter-bubble injection. *Exp. Fluids*, 49:613–622, 2010.

[10] S. Dabiri and G. Tryggvason Heat transfer in turbulent bubbly flow in vertical channels *Chemical Eng. Science*, 122:106–113, 2015.

[11] V. Babin, L. Shermer, and D. Barnea Local instantaneous heat transfer around a rising Taylor bubble. *Int. J. Heat and Mass Transfer*, 89:884–893, 2015.

[12] N. G. Deen and J. A. M. Kuipers Direct numerical simulation of wall-to liquid heat transfer in dispersed gas-liquid two-phase flow using volume of fluid approach *Chemical Eng. Science*, 102:268–282, 2013.

[13] T. J. Liu and S. G. Bankoff. Structure of air-water bubbly flow in a vertical pipe–I. liquid mean velocity and turbulence measurements. *Int. J. Heat and Mass Transfer*, 36:1049–1060, 1993.

[14] S. Guet, G. Ooms, R.V.A. Oliemans, and R. F. Mudde. Bubble size effect on low liquid input drift-flux parameters. *Chem. Eng. Sci.*, 59:3315–3329, 2004.

[15] A. Matos, E.S. de Rosa, and F.A. Franca. The phase distribution of upward co-current bubbly flows in a vertical square channel. *J. Braz. Soc. Mech. Sci. Eng.*, 26:308–316, 2004.

[16] S. Mendez-Diaz, R. Zenit, S. Chiva, J.L. Muñoz-Cobo, and S. Martinez-Martinez. A criterion for the transition from wall to core peak gas volume fraction distributions in bubbly flows. *Int. J. Multiphase Flow*, 43:56–61, 2012.

[17] M. N. Descamps, R. V. A. Oliemans, G. Ooms, and R. F. Mudde. Air-water flow in a vertical pipe: experimental study of air bubbles in the vicinity of the wall. *Exp Fluids*, 45:357–370, 2008.

[18] D. W. Moore. The rise of a gas bubble in a viscous liquid. *Journal of Fluid Mechanics*, 6(1):113–130, 1959.

[19] D. W. Moore. Velocity of rise of distorted gas bubbles in a liquid of small viscosity. *Journal of Fluid Mechanics*, 23(part 4):749–&, 1965.

[20] S. Dabiri, J. Lu, and G. Tryggvason. Transition between regimes of a vertical channel bubbly upflow due to bubble deformability. *Physics of Fluids*. under review.

[21] J. Lu, S. Biswas, and G. Tryggvason. A DNS study of laminar bubbly flows in a vertical channel. *Int. J. Multiphase Flow*, 32:643–660, 2006.

[22] J. Masliyah, R. Jauhari, and M. Gray. Drag coefficients for air bubbles rising along an inclined surface. *Chemical Engineering Science*, 49(12):1905–1911, Jun 1994.

[23] C. E. Norman and M. J. Miksis. Dynamics of a gas bubble rising in an inclined channel at finite Reynolds number. *Physics of Fluids*, 17(2), FEB 2005.

[24] T. Maxworthy. Bubble rise under an inclined plate. *Journal of Fluid Mechanics*, 229:659–673, Aug 1991.

[25] H.K. Tsao and D.L. Koch. Observations of high Reynolds number bubbles interacting with a rigid wall. *Physics of Fluids*, 9(1):44–56, Jan 1997.

[26] R. Krishna, M.I. Urseanu, J.M. van Baten, and J. Ellenberger. Wall effects on the rise of single gas bubbles in liquids. *International Communications in Heat and Mass Transfer*, 26(6):781–790, 1999.

[27] S. Biswas. *Direct numerical simulation and two-fluid modeling of multi-phase bubbly flows*. PhD thesis, Worcester Polytechnic Institute, 2007.

[28] S. O. Unverdi and G. Tryggvason. A front tracking method for viscous incompressible flows. *J Comput Phys*, 100:25–37, 1992.

[29] G. Tryggvason, B. Bunner, A. Esmaeeli, D. Juric, N. Al-Rawahi, W. Tauber, J. Han, S. Nas, and Y. J. Jan. A front tracking method for the computations of multiphase flow. *J Comput Phys*, 169:708–759, 2001.

[30] L. A. Del Castillo, S. Ohnishi, L. R. White, S. L. Carnie, and R. G. Horn. Effect of disjoining pressure on terminal velocity of a bubble sliding along an inclined wall. *Journal of Colloid and Interface Science*, 364(2):505–511, Dec 15 2011.

[31] P. Spicka, M.M. Dias, and J.C.B. Lopes. Gas-liquid flow in a 2D column: Comparison between experimental data and CFD modelling. *Chemical Engineering Science*, 56(21-22):6367–6383, Nov 2001. 5th International Conference on Gas-Liquid and Gas-Liquid-Solid Reactor Engineering, MELBOURNE, AUSTRALIA, SEP 23-27, 2001.

[32] E. Bouche, V. Roig, F. Risso, and A. M. Billet. Homogeneous swarm of high-Reynolds-number bubbles rising within a thin gap. Part 1. Bubble dynamics. *Journal of Fluid Mechanics*, 704:211–231, Aug 10 2012.

[33] B. Bunner and G. Tryggvason. Dynamics of homogeneous bubbly flows. part 1. rise velocity and microstructure of the bubbles. *J Fluid Mech*, 466:17–52, 2002.

[34] B. Bunner and G. Tryggvason. Effect of bubble deformation on the properties of bubbly flows. *J Fluid Mech*, 495:77–118, 2003.

[35] G. Riboux, F. Risso, and D. Legendre. Experimental characterization of the agitation generated by bubbles rising at high Reynolds number. *Journal of Fluid Mechanics*, 643:509–539, Jan 25 2010.

[36] J. Lu and G. Tryggvason. Dynamics of nearly spherical bubbles in upflow in a vertical channel. *Journal of Fluid Mechanics*. under review.

[37] A. W. G de Vries, A. Biesheuvel and L. Van Wijngaarden. Notes on the path and wake of a gas bubble rising in pure water. *Int J Multiphase Flow*, 28:1823–1835 (2002).

[38] H.K. Tsao and D.L. Koch. Observations of high Reynolds number bubbles interacting with a rigid wall. *Physics of Fluids*, 9(1):44–56, Jan 1997.

[39] M. F. Moctezuma, R. Lima-Ochoterena and R. Zenit. Velocity fluctuations resulting from the interaction of a bubble with a vertical wall. *Physics of Fluids*, 17, 098106 (2005).

[40] D.R. Mikulencak and J.F. Morris. Stationary shear flow around fixed and free bodies at finite Reynolds number. *Journal of Fluid Mechanics*, vol. 000:1–28, (2004).

[41] C.A. Kossack and A. Acrivos. Steady simple shear flow past a circular cylinder at moderate Reynolds numbers: a numerical solution. *Journal of Fluid Mechanics*, vol. 66, part 2:353–376, (1974).

[42] S. Dabiri and P. Bhuvankar. Scaling law for bubbles rising near vertical walls. *Physics of Fluids*, 28(6),062101, (2016).

[43] L.M. Milne-Thomson. Theoretical Hydrodynamics, 5th edn. *Macmillan*, 1968, p. 185.

[44] Emmanuel Dériat. Écoulement cisaillé non visqueux autour d'un cylindre proche d'une paroi. *C.R.Mecanique* 300,(2002), 35–38.

[45] S. Dabiri, J. Lu and G. Tryggvason. Transition between regimes of a vertical channel bubbly upflow due to bubble deformability. *Physics of Fluids*, 25,102110, (2013).

[46] H. Hikita, S. Asal, H. Kikukawa, T. Zalke and M. Ohue. Heat transfer coefficient in bubble column. *Ind Eng Chem Process Des Dev*,1981;20:540-545.

[47] A. Mersmann, H. North and R. Wunder. Maximum heat transfer in equipment with dispersed two-phase systems. *Int J Chem Eng*,1982;22:16-29.

[48] W. D. Deckwer On the mechanism of heat transfer in bubble column reactors. *Chemical Engineering Science*,1980;35:1341-1346.

[49] N. Kantarci, F. Borak and K. O. Ulgen Bubble column reactors. *Process Biochemistry*,2005;40:2263-2283.

[50] A. Mehdizadeh, S. A. Sherif and W. E. Lear. Numerical simulations of thermofluid characteristics of two-phase slug flow in microchannels. *Int Journal of Heat and Mass Transfer*,2011;54:3457-3465.

[51] R. Scardovelli and S. Zaleski. Direct numerical simulation of free-surface and interfacial flow. *Annual Review of Fluid Mechanics*,1999;31:567-603.

[52] W. F. Noh and P. Woodward. SLIC (Simple line interface calculation). *Proceedings of the fifth international conference on numerical methods in fluid dynamics, Twente Univ., Enschede*, 1976; 330-340.

[53] D. L. Youngs. Time-dependent multi-material flow with large fluid distortion. *Numerical methods for fluid dynamics, Academic Press, New York*, 1982; 273-285.

[54] Z. Wang, D. Shi and A. Zhang. Three-dimensional lattice Boltzmann simulation of bubble behavior in a flap-induced shear flow. *Computers and Fluids*,123,(2015), 44-53.

[55] A. Serizawa, I. Kataoka, I. Michiyoshi Turbulence structure of air-water bubbly flow. *Int J Multiphase Flow*, 2:235–246, 1975.

[56] T. Hibiki, M. Ishii, Z. Xiao Axial interfacial area transport of vertical bubbly flows *Int J Heat and Mass Transfer*, 44:1869–1888, 2001.

[57] R.V. Mukin. Modeling of bubble coalescence and break up in turbulent bubbly flow. *Int. J Multiphase Flow*, 62:52–66, 2014.

[58] S.P. Antal, R.T. Lahey Jr and J.E. Flaherty. Analysis of phase distribution in fully developed laminar bubbly two-phase flow. *Int. J Multiphase Flow*, 17:635–652, 1991.

[59] J. F. Harper The Motion of Bubbles and Drops Through Liquids. *Advances in Applied Mechanics*, 12:59–129, 1972.

[60] S. K. Wang, S. J. Lee, O. C. Jones Jr., and R. T. Lahey Jr. 3-D turbulence structure and phase distribution in bubbly two-phase flows. *Int. J. Multiphase Flow*, 13:327–343, 1987.

[61] T. J. Liu and S. G. Bankoff. Structure of air-water bubbly flow in a vertical pipe–I. liquid mean velocity and turbulence measurements. *Int. J. Heat and Mass Transfer*, 36:1049–1060, 1993.

[62] V.E. Nakoryakov, O.N. Kashinsky, V.V. Randin, and L.S. Timkin. Gas-liquid bubbly flow in vertical pipes. *J. Fluids Eng.*, 118:377–382, 1996.

[63] T. J. Liu. Investigation of the wall shear stress in vertical bubbly flow under different bubble size conditions. *Int. J. Multiphase Flow*, 23:1085–1109, 1997.

[64] O. N. Kashinsky and V. V. Randin. Downward bubbly gas–liquid flow in a vertical pipe. *Int. J. Multiphase Flow*, 25:109–138, 1999.

[65] S. So, Morikita, S. Takagi, and Y. Matsumoto. Laser doppler velocimetry measurement of turbulent bubbly channel flow. *Exp. Fluids*, 33:135–142, 2002.

[66] M. Sussman, P. Smereka and S. Osher. A level set approach for computing solutions to incompressible two-phase flows. *Journal of Computational Physics*, 114, (1994), 146-159.

[67] G. Son, V. K. Dhir and N. Ramanujapu. Dynamics and heat transfer associated with a single bubble during nucleate boiling on a horizontal surface. *Journal of Heat Transfer- Trans. ASME*, 121, (1999), 623-632.

[68] S. Singh and V. K. Dhir. Effect of gravity, wall superheat and liquid subcooling on bubble dynamics during nucleate boiling, in: V. K. Dhir. *Microgravity Fluid Physics and Heat Transfer, Begell House, New York*, (2000), 106-113.

[69] H. S. Abarajith and V. K. Dhir. Effect of contact angle on the dynamics of a single bubble during pool boiling using numerical simulations. *ASME International Mechanical Eng. Congress & Exposition, New Orleans, LA*, (2002).

[70] G. Son, N. Ramanujapu and V. K. Dhir. Numerical simulation of bubble merger process on a single nucleation site during pool nucleate boiling. *Journal of Heat Transfer- Trans. ASME*, 124, (2002), 51-62.

[71] D. Li and V. K. Dhir. Numerical study of single bubble dynamics during flow boiling. *Journal of Heat Transfer- Trans. ASME*, 129, (2007), 864-876.

[72] E. Aktinol and V. K. Dhir. Numerical simulation of nucleate boiling phenomenon coupled with thermal response of the solid. *Microg. Sci. Technology*, 24, (2012), 255-265.

[73] A. Mukherjee and S. G. Kandlikar. Numerical simulation of growth of a vapor bubble during flow boiling of water in a microchannel. *J. Microfluid. Nanofluid.*, 1, (2005), 137-145.

[74] A. Mukherjee and S. G. Kandlikar. Numerical study of single bubbles with dynamic contact angle during nucleate pool boiling. *Int. J. Heat Mass Transfer*, 50, (2007), 127-138.

[75] A. Mukherjee and S. G. Kandlikar. The effect of inlet constriction on bubble growth during flow boiling inside microchannels. *Int. J. Heat Mass Transfer*, 52, (2009), 5204-5212.

[76] A. Mukherjee, S. G. Kandlikar and Z. J. Edel. Numerical study of bubble growth and wall heat transfer during flow boiling in a microchannel *Int. J. Heat Mass Transfer*, 54, (2011), 3702-3718.

[77] Y. Sato and B. Niceno. A sharp-interface phase change model for a mass conservative interface tracking method. *Journal of Computational Physics*, 249,(2013), 127-161.

[78] Y. Sato and B. Niceno. A depletable micro-layer model for nucleate boiling. *Journal of Computational Physics*, 300, (2015), 20-52.

[79] Y. J. Cho, S. B. Yum, J. H. Lee and G. C. Park. Development of bubble departure and lift-off diameter models in low heat flux and low flow velocity conditions. *Int. J. Heat Mass Transfer*, 54, (2011), 3234–3244.

[80] L. Z. Zeng, J. F. Klausner, D. M. Bernhard and R. Mei. A unified model for the prediction of bubble detachment diameters in boiling system-II. Flow boiling. *Int. J. Heat Mass Transfer*, 36 (9), (1993), 2271-2279.

[81] J. F. Klausner, D. M. Bernhard and L. Z. Zeng. Vapor bubble departure in forced convection boiling. *Int. J. Heat Mass Transfer*, 36 (3), (1993), 651-662.

[82] G. Sateesh, S. K. Das, A. R. Balakrishnan. Analysis of pool boiling heat transfer: effect of bubbles sliding on the heating surface. *Int. J. Heat Mass Transfer*, 48, (2005), 1543-1553.

[83] C. H. M. Baltis and C. W. M. van der Geld. Heat transfer mechanisms of a vapour bubble growing at a wall in saturated upward flow. *Journal of Fluid Mechanics*, 771, (2015), 264-302.

[84] N. Base, G. R. Warrier and V. K. Dhir. Wall Heat Flux Partitioning During Subcooled Flow Boiling: Part 1Model Development. *Journal of Heat Transfer*, Vol (127), (2005), 131-140.

[85] J. Xu, B. Chena, Y. Huanga, X. Yana and D. Yuana. Experimental visualization of sliding bubble dynamics in a vertical narrow rectangular channel. *Nuclear Engineering and Design*, Vol (261), (2013), 156-164.

[86] P. Bhuvankar and S. Dabiri. Impact of a single bubble rising near a wall on the wall-to-liquid heat flux. *Int. J. Heat Mass Transfer*, 116, (2018), 445–457.

[87] Y. Utaka, Y. Kashiwabara and M. Ozaki. Microlayer structure in nucleate boiling of water and ethanol at atmospheric pressure. *Int. J. Heat Mass Transfer*, 57, (2013), 222-230.

[88] W. M. Kays and M. E. Crawford. Convective Heat and Mass Transfer. *Mc-Graw Hill, New York*, (1980), p. 328.

[89] S. Moghaddam and K. Kiger. Physical mechanisms of heat transfer during single bubble nucleate boiling of FC-72 under saturation conditions-I. Experimental investigation. *Int. J. Heat Mass Transfer*, 52, (2009), 1284-1294.

[90] Y. Sato and B. Niceno. Nucleate pool boiling simulations using interface tracking method: Boiling regime from discrete bubble to vapor mushroom region. *Int. J. Heat Mass Transfer*, 105, (2017), 505-524.

[91] M. G. Cooper and A. P. J. Lloyd. The micro-layer in nucleate boiling. *Int. J. Heat Mass Transfer*, 12,(1969), 895-913.

[92] R. Siegel and E. G. Keshock. Effects of reduced gravity on nucleate boiling bubble dynamics in saturated water. *AICHE*, 10, (1964), 509-517.

[93] M. Magnini, B. Pulvirenti and J. R. Thome. Numerical investigation of hydrodynamics and heat transfer of elongated bubbles during flow boiling in microchannel. *Int. J. Heat Mass Transfer*, 59, (2013), 451-471.

[94] D. Juric and G. Tryggvason. Computations of boiling flows. *Int. J. Multiphase Flow*, 24, (1998), 387-410.

[95] S. Shin and D. Juric. Modeling Three-Dimensional Multiphase Flow Using a Level Contour Reconstruction Method for Front Tracking without Connectivity. *Journal of Computational Physics*, 180,(2002), 427-470.

[96] A. Esmaeeli and G. Tryggvason. Computations of film boiling. Part I: numerical method. *Int. J. Heat Mass Transfer*, 47,(2004), 5451-5461.

[97] A. Esmaeeli and G. Tryggvason. Computations of film boiling. Part II: multimode film boiling. *Int. J. Heat Mass Transfer*, 47,(2004), 5463-5476.

[98] T. Sun, W. Li and S. Yang. Numerical simulation of bubble growth and departure during flow boiling period by Lattice Boltzmann method. *Int. J. Heat Fluid Flow*, 44,(2013), 120-129.

[99] R. Jafari and T. Okutucu-Ozyurt. Numerical simulation of flow boiling from an artificial cavity in a microchannel. *Int. J. Heat Fluid Flow*, 97,(2016), 270-278.

[100] J. Y. Lee, M. H. Kim, M. Kaviany and S. Y. Son. Bubble nucleation in microchannel flow boiling using single artificial cavity. *Int. J. Heat Mass Transfer*, 54,(2011), 5139-5148.

[101] B. P. Leonard. A stable and accurate convective modelling procedure based on quadratic upstream interpolation. *Computer Methods in Applied Mechanics and Engineering*, 19(1): 59-98.

[102] A. J. Chorin. The numerical solution of the Navier-Stokes equations for an incompressible fluid. *Bull. Am. Math. Soc.*, 73: 928-931.

[103] J. Yoo, C. E. Estrada-Perez and Y. A. Hassan. Experimental study on bubble dynamics and wall heat transfer arising from a single nucleation site at subcooled flow boiling conditions Part 2: Data analysis on sliding bubble characteristics and associated wall heat transfer. *Int. J. Multiphase Flow*, 84,(2016), 292-314.

[104] J. U. Brackbill, D. B. Kothe and C. Zemach. A continuum method for modeling surface tension. *J. Computation Physics*, 100,(1992), 335-354.

[105] C. S. Peskin. Numerical analysis of blood flow in the heart. *J. Computation Physics*, 25,(1977), 220-252.

[106] R. W. Schrage. A theoretical study of interphase mass transfer. *Columbia University Press, New York*, 1953.

[107] W. H. Lee. A pressure iteration scheme for two-phase flow modeling. *Multiphase Transport Fundamentals, Reactor safety, Applications, vol. 1, Hemisphere Publishing, Washington DC*, 1980.

[108] M. Knudsen. The kinetic theory of gases: Some modern aspects. *Methuen's Monographs Physical Subjects, Methuen and Co., London*, 1934.

[109] I. Orlanski. A simple boundary condition for unbounded hyperbolic flows. *Journal of Computational Physics*, 21, (1976), 251-269.

[110] C. R. Kharangate and I. Mudawar. Review of computational studies on boiling and condensation. *Int. J. Heat Mass Transfer*, 108,(2017), 1164-1196.

[111] D. Bogojevic, K. Sefiane, G. Duursma and A. J. Walton. Bubble dynamics and flow boiling instabilities in microchannels. *Int. J. Heat Mass Transfer*, 58,(2013), 663-675.

[112] K. P. Drummond, D. Back, M. D. Sinanis, D. B. Janes, D. Peroulis, J. A. Weibel and S. V. Garimella. A hierarchical manifold microchannel heat sink array for high-heat-flux two-phase cooling of electronics. *Int. J. Heat Mass Transfer*, 117,(2018), 319-330.

VITA

VITA

Education

- **PhD** in Mechanical Engineering - Purdue University, August 2019.
- **M.Tech** in Mechanical Engineering - Indian Institute of Technology, Madras, July 2014.
- **B.Tech** in Mechanical Engineering - Indian Institute of Technology, Madras, July 2014.

Awards and scholastics achievements

- Sigma Xi Purdue Chapter Poster Presentation Competition (2019): Presentation entitled *A numerical method to simulate flow and nucleate boiling*, won the **First prize** for poster presentations in the **Engineering category**.
- IITJEE Examination (2009): Ranked **1184** out of **300,000** competitors nationwide in India.

Publications

- P. Bhuvankar and S. Dabiri, "Direct numerical simulation of flow boiling in a micro-channel: Effect of the inlet flow rate, hot-spot.", under revision
- P. Bhuvankar and S. Dabiri, "Direct numerical simulation of sliding bubbles in flow boiling under a shear rate.", under preparation
- P. Bhuvankar and S. Dabiri, "Impact of a single bubble rising near a wall on the wall-to-liquid heat flux", *Int. J. Heat Mass Transfer*, 116, (2018), 445-457.

- S. Dabiri and P. Bhuvankar, "Scaling law for bubbles rising near vertical walls", *Physics of Fluids*, 28(6), 062101 (2016).

Conference and poster presentations

- P. Bhuvankar and S. Dabiri, "A numerical method to simulate flow and nucleate boiling", *Poster Presentation Competition : Sigma Xi, Purdue Chapter (2019)* : **First prize in the Engineering section.**
- P. Bhuvankar and S. Dabiri, "A front-tracking based method to simulate phase change in two-phase flows", *ParCFD* (2018).
- P. Bhuvankar and S. Dabiri, "Numerical study of the bubbly flow regime in micro-channel flow boiling", *Bulletin of the American Physical Society* (2017).
- P. Bhuvankar and S. Dabiri, "The effect of flow pattern around a bubble rising near a vertical wall, on the wall to liquid heat transfer", *APS Meeting Abstracts* (2016).
- S. Dabiri and P. Bhuvankar, "Rising motion of a bubble layer near a vertical wall", *APS Meeting Abstracts* (2015).

Teaching experience

- *Transport Phenomena (ABE307)*: Fall 2017.
- *Thermodynamics (ABE210)*: Spring 2017, Spring 2018.
- *Introduction to Design & Entrepreneurship (ME263)*: Spring 2016.

Research Experience

- Fully resolved high-fidelity simulation of nucleate & flow boiling: Developed a numerical method using the front-tracking framework to run 3D simulations of

boiling and condensation in multiphase flows. Developed a stagnant micro-layer model for nucleate pool boiling.

- CFD simulations of bubbles near a wall: Conducted simulations using the **PARIS** multiphase simulation code in FORTRAN to find a scaling law for the flow rate and the wall viscous dissipation of a bubble layer rising near a vertical wall.
- Heat transfer around a bubble rising near a wall: Conducted CFD simulations to find the effect of flow patterns around a bubble rising near a vertical wall on the wall-to-liquid heat transfer.
- Turbulent two-phase heat transfer in channels: Currently mentoring a student in running Direct Numerical Simulations of turbulent bubbly flow heat transfer in horizontal channnels.